Nanosecond Laser Ablation of Thin Film Material Libraries

Simina Aurelia Rebegea

Department of Mechanical Engineering

School of Engineering

University of Birmingham

This dissertation is submitted for the degree of Doctor of Philosophy

February 2018

UNIVERSITY OF BIRMINGHAM

University of Birmingham Research Archive

e-theses repository

ABSTRACT

A novel approach in the field of pulsed laser ablation of thin films is discussed, namely thin films having controlled variations in chemical composition irradiated with a beam of constant parameters. The method proposed in this thesis could be incorporated in the development of new materials where the machining capabilities would be assessed as a function of composition, thus potentially replacing a difficult-to-machine material. Moreover, a different perspective of the same process could lead to new insights or a deeper understanding of any beam-workpiece interaction in general and material removal by pulsed laser ablation in particular.

Nowadays lasers are used in a variety of industries, where materials' processing holds the highest market share (35%), overcoming even the communication industry (33%). Laser processing of materials (e.g. cutting or drilling in semiconductor manufacturing) is regarded as a non-conventional machining method which eliminates the problem of tool wear, minimises the damage to the workpiece and requires no special atmosphere or chemicals to be efficient. Extensive theoretical and empirical work has been carried out to understand laser-material interaction. The most common approach to study the laser ablation is to vary processing parameters (such as wavelength, pulse duration or pulse energy) and investigate the material response, which can be, for example, geometry of the ablated region (i.e. crater) temperature measurement or characterisation of laser-produced plasma.

This study focuses instead on ternary thin film material libraries (copper, aluminium, nickel, and zirconium) irradiated with a beam of constant parameters (30-55 ns pulse length, 1064 nm wavelength). As reference, experiments on pure films and their

corresponding binary alloys were carried out. Thin films with a thickness in the range of 1 µm were deposited on Si wafers using magnetron sputtering technique and characterised prior to laser ablation in terms of chemical composition, reflectivity and surface/ sub-surface morphology.

First, the study of pure Cu and Al thin films revealed similarities in terms of laser-ablated morphology compared to Ni. The different crater morphologies were attributed to the combined effects of laser scattering at the surface, thermal diffusivity of the metals and the presence of a thermal barrier between the thin film and the substrate. A preferential lateral heat transfer for the Ni films compared to the more common vertical one in Cu and Al was identified.

Second, binary films (Cu-Ni, Ni-Al and Cu-Al) were used to investigate the contributions of chemical composition variations in crater geometry and morphology, for both smooth and structured films. The results showed that the microstructure of the target material had a major influence on the crater shape and morphology, while the material properties had minimal contribution, noticeable only in the absence of variation in film morphology. When the film had a relatively homogenous structure and surface morphology, the change in thermal properties caused solely by the chemical composition were less significant.

Finally, the study of the ternary compositional gradients irradiated with constant laser parameters extends upon the findings of the pure and binary films, and represents, to the author's knowledge, the first work of this type. A second film with compositional gradient (copper, aluminium and zirconium) was analysed to confirm that the variations in crater geometry and morphology were not typical to only Cu, Al, Ni and their corresponding alloys. Similarities between the two samples both prior to and after laser

ablation were discussed. Moreover, due to the higher reflectivity of the zirconium ternary alloy, crater morphology was representative of how boiling occurs revealing that microstructures on the surface acted like ignition centres which eventually could be responsible for the variations in crater geometry observed throughout this work.

DEDICATION AND ACKNOWLEDGEMENTS

I dedicate this thesis to my parents, Angela and Teodor, and to my sister, Irina. I would not have made it this far without your constant encouragement and support.

I would like to show my deepest gratitude to my main supervisor, Dr. Ming Chu (Carol) Kong, for guiding me throughout these years in both professional and personal life, with patience, dedication and care.

My thanks go to Prof. Dragos Axinte (coordinator of the STEEP project) and Prof. Stefan Dimov (my co-supervisor), for their valued support during my research.

I would like to acknowledge the collaboration with my colleagues in the STEEP project and useful discussions on material synthesis and analysis with my colleague at EMPA (Swiss Federal Laboratories for Materials Testing and Research).

I acknowledge my colleague at University of Liverpool who carried out the initial laser ablation test before the start of my PhD.

I acknowledge the funding support of EUFP7-ITN (Grant no. 316560) for the work presented as a part of the STEEP project.

Special thanks go to my friend and colleague, Jean-Michel who helped proofreading this manuscript.

My appreciation goes to my friends, old and new, whom I shall not name, but I am sure you will find yourselves in here, for being by my side to lift me up when I was down.

Finally, my thoughts go to my "best colleague ever", Stefano, for being on my right-hand side for three years, in both laser-related discussions, philosophical lunch talks and the occasional drinks.

Although the acronym "loser" (Light Oscillation by Stimulated Emission of Radiation) more accurately describes the process of light generation in a laser, the acronym "laser" (Light Amplification by Stimulated Emission of Radiation) was historically adopted for obvious reasons! (-Alphan Sennaroğlu)

The world is only as meaningful to us as the beings that inhabit it. (-Xe'ra)

TABLE OF CONTENTS

LIST OF FIGURES

LIST OF TABLES

LIST OF ABBREVIATIONS AND ACRONYMS

PLA   pulsed laser ablation

IR   infrared

EM   electromagnetic

UV   ultraviolet

Vis   Visible

LPP   Laser produced plasma

HAZ   Heat affected zone

XRF   X-ray fluorescence spectroscopy

SEM   Scanning electron microscopy

FIB   Focused ion beam

ns   nanosecond

ICCD Intensified charge-coupled device

Sccm standard cubic centimetre per minute

NOMENCLATURE

Symbol	Units (S.I.)	Description
F_0	J/m^2	absorbed fluence (after reflection from sample surface)
F_L	J/m^2	laser fluence (laser output)
F_{th}	J/m^2	threshold fluence (estimated based on material properties)
L_m	J/kg	latent heat of melting
L_v	J/kg	latent heat of evaporation
T_m	K	melting temperature
$f, \quad s$	-	Subscripts indicating thin film or substrate
l_f	m	thermally active depth
v_s	m/s	velocity of the substrate relative to the heat source
ΔL_m	J/kg	melting enthalpy
ΔT_v	K	variation between the evaporation and room temperature
Δz_v	m	ablation depth per pulse
α_{surf}	-	surface scattering coefficient
δ_{th}	m	thermal diffusion length
σ_{RMS}	m	root mean square roughness
$h - h$	m	height-height correlation length
A	-	absorptivity
I	W/m^2	intensity of the electromagnetic field
K	J/ (kg K)	thermal conductivity
L	$W\Omega/K^2$	Lorenz number
N	-	complex refractive index
P	W	average power
Q	J	heating rate
R	-	reflectivity
S	m^2	laser beam area in the focus plane
T	K	temperature

c	J/ (kg K)	specific heat
d	m	thin film thickness
e	-	Euler's number
f	Hz	repetition rate
i	-	imaginary unit
k	m^2/s	thermal diffusivity
m	-	weight percentage
n	-	refractive index
z	m	depth (distance from the surface)
α	m^{-1}	absorption coefficient
δ	m	optical absorption depth
η	-	energy efficiency
κ	-	extinction coefficient
λ	m	wavelength
ρ	kg/m^3	mass density
σ	S/m	electrical conductivity
τ	s	pulse duration
ϕ	m	beam diameter in focus

PUBLICATIONS

(Published) **S. A. Rebegea**, K. Thomas, V. Chawla, J. Michler, and M. C. Kong, "Laser ablation of a Cu–Al–Ni combinatorial thin film library: analysis of crater morphology and geometry," *Appl. Phys. A*, vol. 122, no. 12, p. 1074, 2016.

(Under submission) **S. A. Rebegea**, S. Buratin, L. Petho, J. Michler, M. C.Kong, *Crater shapes and geometries obtained by irradiation of metal films with nanosecond infrared laser*

(In preparation) **S. A. Rebegea**, K. Thomas, L. Petho, J. Michler, M. C. Kong, *Laser ablation of binary combinatorial thin film libraries of Cu, Al and Ni: the effect of film composition and microstructure on crater characteristics.*

1 INTRODUCTION

1.1 MOTIVATION

Thin film material libraries are samples with gradients in chemical composition, usually investigated using time-efficient characterisation techniques. This field of research is called high-throughput screening (or characterisation) and it has been used by material scientists to discover or optimise materials for a specific application [1]. The technique has been successfully applied for alloy discovery and optimization, alloy design, the study of local stress in thin films, phase diagrams and composition-structure-property relationships and determining experimental enthalpies of formation of [2–7]. It would be of interest to extend the application of high-throughput characterisation into the discovery of new materials from the machining perspective in order to replace difficult-to-machine materials. It would be beneficial, for example, if three alloys with desired properties were found but one of them prove easier-to-machine compared to the others; this material would be further used for the particular application, decreasing the final production costs.

Laser based technologies are gaining ground in the manufacturing industry as non-conventional machining processes, as they allow precise machining of micron and submicron features in otherwise difficult to machine materials (e.g. ceramics, semiconductors). Ever since the first demonstration of a functioning laser in 1960 [8,9], extensive research has been carried out to understand laser beam interaction with a material [10] and thus to develop new applications [11]. The realisation that a high

amount of energy could be spatially and temporally confined in such a way to create changes in the material (e.g. surface modification by melting or removal of material by vaporisation) led to a wide variety of fields where laser technology is used as a complementary tool or, often, preferred with respect to previously used techniques. Nowadays lasers are used in a various range of devices and with various purposes: in medicine (e.g. laser eye surgery), bar scanners, storage devices, measuring distances etc. The laser market for the year 2017 given in Figure 1.1 shows the areas in which lasers are used nowadays. Material processing (e.g. cutting, drilling, patterning and machining in general) is the dominant field, overcoming even the communications industry.
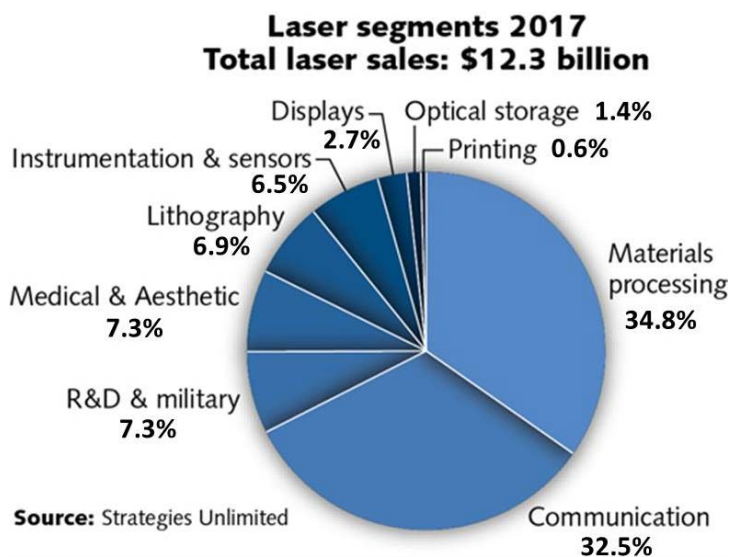
Figure 1.1 Laser market segments in 2017 (adapted from [12]).

Lasers are preferable to conventional machining methods because of several advantages: no tool wear, minimal damage to the workpiece and no special atmosphere requirements (such as higher temperatures or vacuum). The present work focuses on the laser as a micro-processing tool, which finds applications such as micro-electronics packaging, semiconductor manufacturing, data storage devices, medical devices,

communication and computer peripherals as the need to fabricate high accuracy features on a very small scale increases.

Despite the advantages of laser micromachining over other conventional or non-conventional methods [13,14], the complex phenomena occurring when a material is irradiated with a pulsed laser makes the exact outcome difficult to predict [15,16]. Considering the broad area of materials processing, with the sub-categories shown in Figure 1.2, numerous studies (detailed below) focused on gaining a better understanding of laser removal by pulsed laser ablation (PLA), because there are many laser parameters and material properties which affect the material response when irradiated with a laser beam.

Industrial laser applications 2017

Additive manufacturing **4%** Other **2%**
Non-metal processing **6%**
Fine metal processing **8%**
Cutting **35%**
Semiconductors/ displays **14%**
Marking **15%**
Weld/braze **16%**

Source: Strategies Unlimited
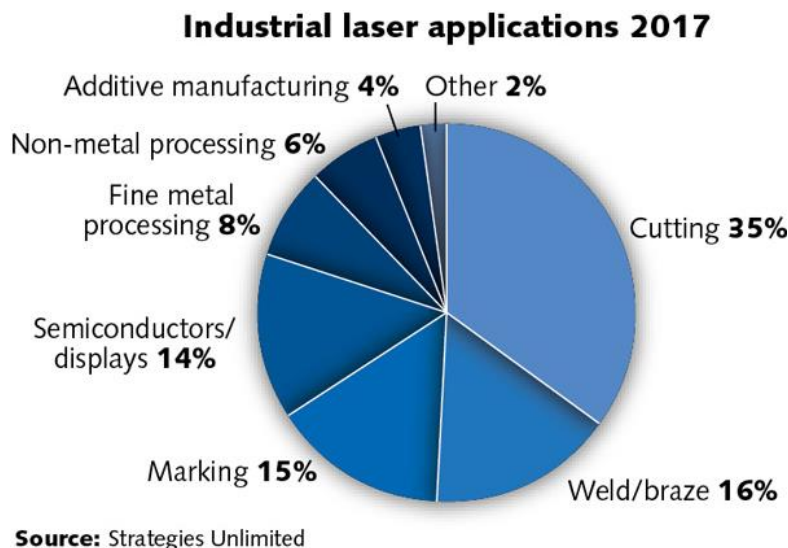
Figure 1.2 Industrial laser applications for 2017 [12].

Extensive theoretical and empirical studies alike have been dedicated to investigating phenomena occurring during PLA, each considering various physical parameters of the laser beam and target material [17–23]. Some of these models are

accompanied by experimental investigations of the dynamics involved, studied by either time resolved techniques [24–26], imaging of the process with fast ICCD (intensified charge-coupled device) cameras [18,27], time-of-flight measurements [17,27] or analysis of the plume expansion [28,29]. Only a few studies have focused on the geometry of the ablated craters and the changes of the subsurface [30,31].

Although previous studies cover a wide range of materials (e.g. pure metals [32,33], alloys [34,35], semiconductors [36,37] and optically transparent materials [38]), the approach used is generally the same, i.e. to study the laser-material interaction for targets of constant chemical composition with well-known optical and thermal properties, by adjusting the beam parameters, such as fluence, pulse duration and wavelength. Several examples which used the typical approach to study the nanosecond laser ablation of metals are given in Table 1.1. To the author's knowledge, the material response to PLA when the composition of the target is incrementally varied has so far not been investigated. Small variations in the chemical composition of a material can be obtained by using thin film material libraries. As the compositional spread can be continuous (composition gradient) or discrete (by using masks in the deposition process), smaller increments could be obtained if necessary by varying material parameters instead of the usual laser parameters, allowing for a more detailed analysis of laser-material interaction.

Table 1.1 Examples of studies which investigate laser ablation by varying laser parameters and irradiating a target of known chemical composition.

Laser parameter	Description
Pulse duration	- Four pulse regimes were investigated (ms, ns, ps and fs) and nanosecond ablation showed the highest efficiency for micro-drilling of stainless steel. Ablated mass was shown to increase with the number of pulses for various pulse regimes [39]. - Residual thermal effects in an Al target were systematically studied following single-pulse irradiation with various pulse lengths (45 ns, 55 ns and 60 fs), wavelengths (690 nm, 1064 nm and 800 nm respectively) and in different atmospheres (air, oxygen and helium) or ambient pressures (atmospheric pressure, 1 torr, 0.04 torr and vacuum) [40].
Wavelength	- While absorption of metals is generally higher in UV (266 nm) compared to the green (532 nm) or near-infrared (1064 nm), plasma formation threshold for several metals has been shown to be much lower for 1064 nm (at 5 ns pulse duration) [30]. - The etch rate of copper as a function of wavelength has been investigated. Highest etch rate was achieved when using a 532 nm wavelength (~13 µm/pulse), compared to ~7 µm/pulse at 355 nm and ~2 µm/pulse at 1064 nm [41].
Atmosphere/ Ambient pressure	- The ablation process (22 ns, 1064 nm) has been shown to depend on the ionisation threshold and density of the ambient gas (i.e. air, argon and helium), through the effects of laser-produced plasma on the material removal [42]. - Crater geometry and particle distribution have been analysed on Al and brass targets irradiated with an 8 ns pulse at 1064 nm. It is shown that ablation efficiency and laser ablation synthesis of nanoparticles is more suitable for mass production of nanoparticles [43].

Power/ fluence	- For a Ni target irradiated with a 30 ns pulse (248 nm wavelength) a sudden increase in plasma velocity and transmissivity was observed at a fluence of 5.2 J/cm^2, which was attributed to the evaporation being an explosive type phase change [28].
Spot size	- The plasma plume expansion and shielding effects have been investigated as a function of beam diameter in focus (between 0.1 mm and 0.6 mm) for a Cu target irradiated in air with a 15 ns pulse at 1064 nm [44].
Pulse number	- Crater depth and diameter increased with the number of pulses, up to a threshold (~20 pulses) dependent on plasma shielding of the target from the workpiece. The target was Al irradiated with ~6 ns pulse, 532 nm wavelength [45].

The present work has been carried out within the context of STEEP EUFP7-ITN project (*A Synergetic Training Network on Energy Beam Processing: from Modelling to Industrial Applications*), whose aim is to establish a unifying research platform on energy beam processing methods. The three energy beams (waterjet, laser and focused ion beam) are part of the non-conventional machining processes group and are regarded as efficient material removal technologies for demanding applications, at different spatial scales (micro, meso and nano). Despite the different material removal mechanisms of these beams, a common aspect is used to unify them under a machining platform, namely their nature as dwell time dependent processes. The final aim of the STEEP project is to develop a beam path simulator to be implemented on real workstations, based on a general model for material removal. To achieve this goal, several fields of research are to be approached simultaneously (i.e. *(i)* generic mathematical modelling of footprints and experimental validation of results, *(ii)* investigation of the physical process and material parameters relevant to each of the beams and *(iii)* development and optimisation of

algorithms for effective processing tool paths. Within the context of STEEP, the present work falls within the second field (*ii)*, the research area of experimental investigations of laser-material interactions, namely the material properties relevant to nanosecond PLA ("thermal regime") and their contribution to the geometry and morphology of the ablated workpiece. This could enable easier machining in terms of resulting footprint when the relevant material characteristics are known.

1.2 AIM AND OBJECTIVES

The aim of this work is to offer a novel approach to the investigation of material response (in terms of crater geometry, volume removal, and sub/surface morphology) in pulsed laser ablation (PLA), by using a material library (having small variations in the chemical composition) and irradiating it with a beam of constant parameters. The present work uses a step-by-step approach for investigation of thin film material, by starting from the pure copper (Cu), aluminium (Al) and nickel (Ni) thin films, followed by the binary alloys (Cu-Ni, Ni-Al and Cu-Al) and ending with the investigation of the ternary copper-aluminium-nickel/zirconium (Cu-Ni-Al/Zr) alloys.

The objectives of this study, specific to each set of samples, are shown below.

- *Pure films*: (a) to optimise the PLA processing of thin films by varying the laser fluence; (b) to empirically study the resulting crater morphologies and geometries following irradiation with constant fluence; (c) to correlate crater characteristics (geometry, volume and morphology) with the material properties to understand which of the latter have the higher contribution to the final crater shape.

- *Binary films*: to evaluate the evolution of crater shape and morphology when accompanied by a notable change (a) in chemical composition; (b) only in the thin film morphology prior to irradiation; (c) in both chemical composition and thin film morphology.

- *Ternary films*: (a) to investigate the material response of the Cu-Al-Ni ternary alloy to ablation with constant laser fluence and correlate the results with the pure and binary samples; (b) to identify whether the material response is limited to Cu-Al-Ni alloys, by comparing with identical experiments on a ternary Cu-Al-Zr thin film; (c) to study the various stages of material vaporisation by investigating the morphology of craters obtained with fluence below complete crater formation.

In addition, in order to achieve the above objectives, an important part of this work focused on the design of efficient experimental methods for both thin film and crater characterisation.

1.3 THESIS OUTLOOK

This work is divided in seven chapters (as shown in Figure 1.3), as follows:

Chapter 1 (*Introduction*) discusses the motivation behind the work in terms of extending the use of material libraries to discover easy-to-process materials as well as the importance of PLA as a non-conventional processing method. A general description of aims and objectives is given to guide the reader through the approach used, and a brief overview of each chapter is given to guide the reader through the contents of this work.

Chapter 2 (*Literature review*) places the current work in a broader context. Basic knowledge of laser is given to understand the generation of the laser beam. Also, the

interaction between short pulsed laser and metallic films is analysed. Thin film properties which affect heat diffusion and ablation threshold for nanosecond pulses are discussed together with previous works which focused on nanosecond PLA of thin films.
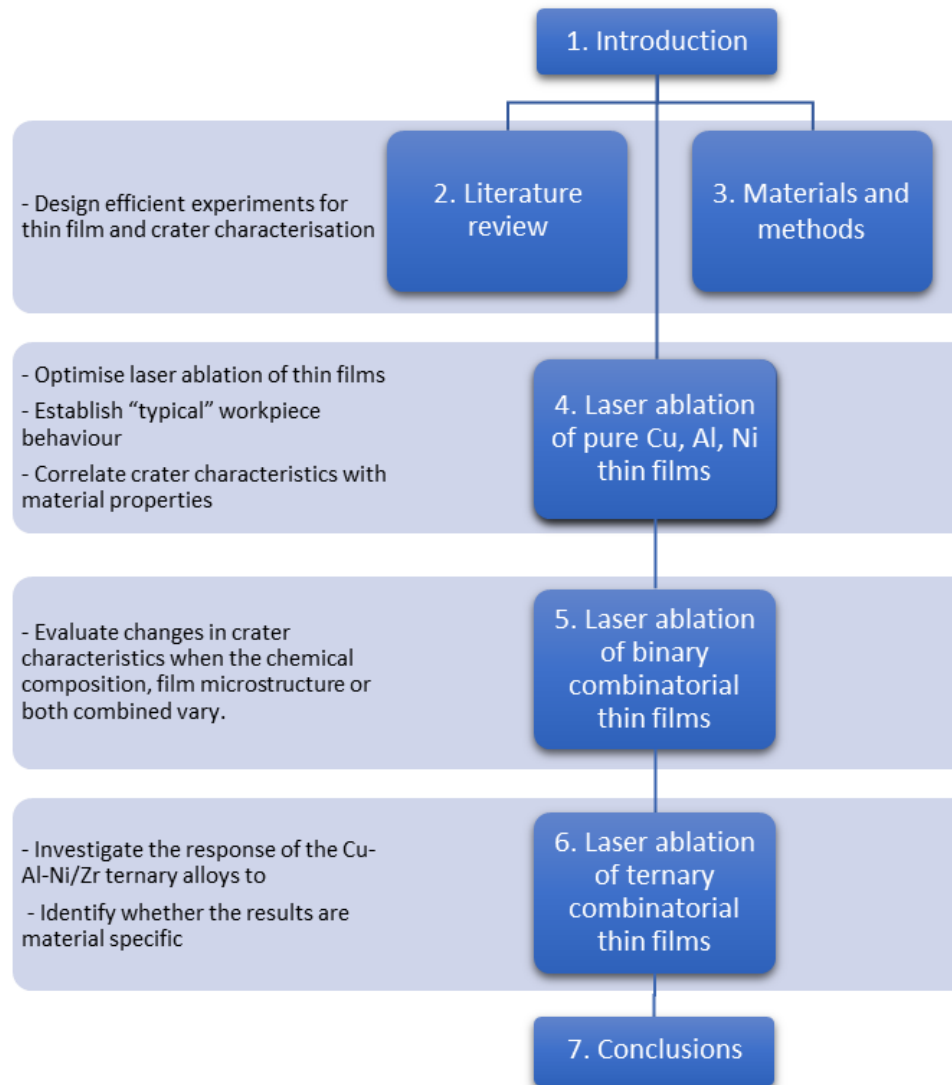
Figure 1.3 Thesis outline and objectives overview.

Chapter 3 (*Materials and methods*) gives general information on the synthesis of the pure (Cu, Al and Ni), binary (Cu-Ni, Ni-Al and Cu-Al) and ternary samples (Cu-Ni-Al, Cu-Al-Zr) by magnetron sputtering technique and characterisation of the as-deposited thin films in terms of thickness, chemical composition and optical properties. A

description of the experimental setup and methodology is given for the laser processing and further geometrical and morphological characterisation of the craters for the pure and binary samples. Particularities of the experiments (i.e. process parameters) are given at the beginning of each chapter. The experimental setup details and parameters for the ternary alloys are given in Chapter 6.

Based on material properties (e.g. reflectivity and thermal conductivity), **Chapter 4** (*Laser ablation of pure copper, aluminium and nickel thin films*) deals first with estimation of the ablation threshold and resulting ablated geometries and morphologies for each of the pure Cu, Al and Ni thin films. The material properties which have a considerable influence on the ablation result are discussed.

In **Chapter 5** (*Laser ablation of binary alloys*) the influence of chemical composition and film surface- and sub-surface morphology on the crater characteristics is studied. The binary Cu-Ni solution is used to illustrate how significant variations in chemical composition affect the crater shape in the absence of well-defined film morphology. In addition, as the nickel-aluminium shows a strong morphological gradient (from small surface structures to a more pronounced columnar structure of the film), the influence of surface morphology is discussed when the change in chemical composition is minimal. Finally, variations in crater characteristics in the presence of both chemical and morphological gradients are studied.

In **Chapter 6** (*Laser ablation of ternary combinatorial thin film libraries*) the material response of the Cu-Ni-Al ternary alloys, a shape memory alloy in certain compositions, is discussed with respect to the previous findings in chapters 4 and 5. To illustrate that the results are not sample-specific, the ternary Cu-Al-Zr compositional

gradient was also investigated because of the different thermal properties of Zr and Ni as well as the industrial application of Cu-Al-Zr as a bulk metallic glass.

Chapter 7 (*Conclusions*) discussed the main findings. The original contributions and limitations of this study are also highlighted, and recommendations for further work are presented at the end of the chapter.

2 LITERATURE REVIEW

Compared to other sources of emission, laser light has three main characteristics: *(i)* it is highly monochromatic – the radiation has a very narrow spectrum; *(ii)* it is directional – light is emitted mainly in one direction (little divergence), as opposed to other sources of light (e.g. the sun); *(iii)* it has spatial and temporal coherence – the photons are in the same phase and have the same wavelength [46]. The unique nature of the laser beam enables the precise delivery of a high amount of energy to the material in a very short time and in a spatially confined region near the surface. Irradiating a material with a laser may induce permanent changes in the material, such as surface morphology or crystalline structure, which makes the laser a useful non-conventional tool for micromachining.

The present work covers two main topics – material libraries/high throughput characterisation and laser ablation. For a comprehensive review on the state-of-the-art in high-throughput screening the reader is referred to the work of Potyrailo et al. [1]. The book by P. Schaaf (ed.) [16] offers a compact view on lasers, from the generation of the laser light to the time-dependent laser-material interaction and to a wide range of applications.

Throughout this chapter the reader is guided through the basics of laser-light generation (Section 2.1), followed by the phenomena occurring as the beam reaches the surface and the events which occur as more and more energy is transferred from the laser to the workpiece (Section 2.2). The latter are discussed with respect to the material properties which affect the absorption of laser light and transmission of heat in the sample. The particularities of thin film laser ablation are then discussed in Section 2.3, focusing on the variations in material properties and heat transfer to the substrate, both influenced

by the film thickness. The chapter ends with a review focused on nanosecond pulsed laser ablation (PLA) of thin films (Section 2.4).

2.1 BASIC PRINCIPLES OF LASERS

LASER stands for **L**ight **A**mplification by **S**timulated **E**mission of **R**adiation, a theory first formulated in the late 1950s by C. H. Townes, N. G. Basov and A. M. Prokhorov, who were awarded the Nobel Prize in Physics in 1964 [47–49], "for fundamental work in the field of quantum electronics, which has led to the construction of oscillators and amplifiers based on the maser-laser principle" [50]. Stimulated emission, the fundamental principle behind laser, is a quantum process which describes the interaction between light carriers (i.e. photons) and atoms and molecules, more specific, their electrons). The first stage of stimulated emission is absorption of photons, which leads to the formation of excited species, i.e. electrons move from the fundamental state with minimum energy to a higher energetic level. Subsequently this energy of excitation is released as the electrons move back to the fundamental level, in the form of photons (stimulated emission). These photons are in phase and travel in the same direction, which gives the laser its coherence and directionality. Usually they are spectrally pure but may have a range of wavelengths if the change is from an energy well to a lower state. When more atoms and molecules are in an excited state than in the lower energy state, population inversion is achieved, which is a fundamental condition for generating laser radiation.

The properties which distinguish the laser from other sources of light and make it such a versatile tool which finds uses in numerous applications, are a result of how the beam is generated. A typical laser setup has three main components and is shown in Figure 2.1.
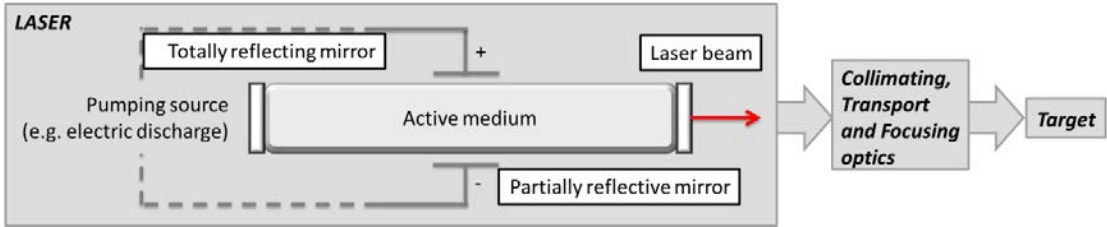
Figure 2.1 Schematic representation of a typical laser source (adapted from [16,51]).

- Active medium (or lasing material). Any material, whether it is solid (semiconductor [52], crystal [53]), liquid (dye laser [54]) or gas (He-Ne [55], CO_2 [56]), will lase provided that enough evergy is delivered to excite its atoms or molecules and obtain the population inversion. For example, a most unusual type of active medium was gelatin, which made the laser edible [57]. The active medium is used to amplify the energy from the pumping source and influeces the output wavelength. An important subcategory of lasers is the solid-state lasers, where the active medium is glass or a crystalline material usually doped with rare-earths, most commonly doped with neodymium or ytterbium. Solid-state lasers have evolved into fibre lasers, where the optical fibre is doped with similar dopants. The advantages of using fibre lasers consist of high average powers and high beam quality [58].

- Pumping source (or energy source). Common energy sources used to excite the active medium are flash lamps, other lasers and electric discharges. The output power of the laser depends on the pumping source and the amount of active medium [58]. An energy efficient, high power pumping source is the laser diode, which resuts in overall lower energy consumption and cooling requirements.

- Optical cavity (or resonator). This usually consists of a cavity with two mirrors at

each end, one 100% reflective and the other one partially reflective. Its purpose is to increase the length of the active medium (by making the beam pass through it multiple times), and determines the boundary conditions for the electromagnetic fields inside the cavity (similar to standing waves on a string). Commonly the optical fibres in fibre lasers act as both an optical cavity and active medium. In addition, the fibre geometry allows easy delivery and focusing of the beam which simplifies laser operation [59].

The initial step in the process of lasing is the excitation of the atoms and molecules in the active medium (e.g. optical fibre doped with ytterbium atoms) by a photon from the electromagnetic field of the pumping source (e.g. laser diode). First, spontaneous emission naturally occurs, meaning that atoms in a higher energy state decay spontaneously to the lower state. The photons emitted this way come out in random directions and, without any other process occurring in the active medium, the excited population will steadily shift to the fundamental state. However, when atoms become excited by interacting with an electromagnetic field, when emitting, the resultant photon gives its energy to the field. This photon has the same frequency, same phase and sense of polarisation and propagates in the same direction as the wave that induced the excitation [51]. Population inversion is essential to achieve amplification of light by stimulated emission, which means that more atoms need to be in the excited state than in the fundamental one. Einstein first showed that there is an interrelation between spontaneous emission, absorption and stimulated emission; for the full discussion the reader is referred to his work on the subject [60]. A part of these generated photons exits the optical resonator, as an energetic beam. An optical setup is then used to focus and

deliver the laser to the workpiece, where complex processes regarding the laser-material interaction occur.

2.2 CONSIDERATIONS OF LASER-MATERIAL INTERACTION

In the previous section the fundamental principles of laser light generation were discussed. Further, as the laser beam reaches the surface of the workpiece, several optical phenomena may occur: reflection, absorption and transmission. These are influenced by the interaction between the incident electromagnetic field and the electrons in the sample governed by the Maxwell equations. Thus, the first parameters which indicate how the material responds to irradiation are generally given by its electronic structure (dielectric, semiconductor or metal) and the laser wavelength.

2.2.1 Absorption of laser light

For the laser to produce any effect, it needs to be absorbed by the sample. This is determined by the optical properties of the material, namely the complex refractive index $N = n - i\kappa$, where n is the real part of the refractive index, κ the extinction coefficient and i the imaginary unit. The intensity of the absorbed radiation below the surface is described by Beer-Lambert law, which states that the intensity of the electromagnetic (EM) field $I(z)$ inside a given material at depth z drops exponentially from the surface, shown in Equation (2.1), and depends on the wavelength through the absorption coefficient α. The depth at which the intensity of this field decreases to $1/e$ is called the penetration depth (electromagnetic or optical) and is given by $\delta = 1/\alpha$.

$$I(z) = I_0 e^{-\alpha z} \tag{2.1}$$

The reflectivity R, the absorption coefficient and optical penetration depth at normal incidence are related to the complex refractive index through Equation (2.2) and Equation (2.3), where λ is the radiation wavelength.

$$R = \frac{(n-1)^2 + \kappa^2}{(n+1)^2 + \kappa^2} \tag{2.2}$$

$$\alpha = \frac{4\pi\kappa}{\lambda} \tag{2.3}$$

Aluminium, as a common metal, can be considered as an example: for a wavelength of $\lambda = 1033.2\ nm$ the real part of the refractive index is $n = 1.3998$ and the imaginary part is $k = 9.8914$ which give an absorption coefficient of $\alpha = 1.2030 * 10^6\ cm^{-1}$, resulting in an optical penetration depth of $\delta = 8.3126\ nm$. In an analogous manner one can compute the values for copper and nickel which are 12.095 nm and 14.349 nm respectively. The values for Cu, Al and Ni used for these calculations were taken from references [61], [62], and [63] respectively.

The absorption of metals is higher for ultraviolet light compared to the infrared spectrum, so laser ablation efficiency of metals is increased when UV-Vis wavelengths are used. For example, simulation of the early ablation stage (<100 ns) of lead targets using 30 ns laser pulses showed that higher surface temperature, vapour mass and ionisation fraction were achieved when using 248 nm KrF excimer laser instead of a 1064 nm Nd:YAG laser (Figure 2.2) [64]. The higher yield in UV laser ablation of metals is caused not only by the increased absorption of metals in UV-Vis (e.g. the reflectance of a polished copper surface at 1064 nm is 97% compared to 65% at 532 nm), but also by the attenuation of the incoming laser beam being stronger for longer wavelength, as pointed out in by Stafe et al. [33].

17
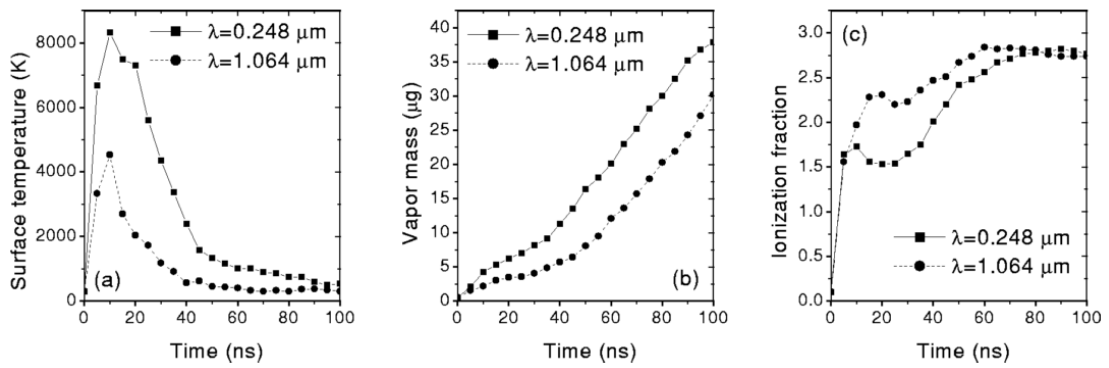
Figure 2.2 Temporal evolution of (a) surface temperature, (b) vapour mass and (c) ionisation fraction of lead using 248 nm and 1064 nm lasers with fluence 10 J/cm² [64].

2.2.1.1 *Influence of material properties on absorption of laser light*

Despite metals being highly reflective in the near-infrared (NIR) and infrared (IR) domains, lasers operating in IR (such as Nd:glass, fibre and CO_2 lasers) are widely used in materials processing, due to, among others, less wear of the optical components and cost effectiveness [58]. Machining of metals with IR lasers is still possible due to their high peak power, but also to an increase in absorption which can occur on account of various material and laser-related factors, and the most important of them are listed in Table 2.1.

Table 2.1 Laser and material properties of importance to absorption (adapted from [65]).

Laser properties	Metal properties
Wavelength	(I) Chemical composition
Polarisation	(II) Roughness/topography
Angle of incidence	(III) Temperature
Intensity, non-linear effects	(IV) Oxide layers
	(V) Plasma coupling

Due to the nature of the present work which focuses on material as a "variable" in the laser ablation process, and the extensive literature on how laser parameters affect

laser-material interaction (including the changes in absorption), only the metal properties which play a role in modifying absorption of laser light are discussed below.

(I) <u>Chemical composition</u>. The optical properties of a material are the result of interaction between the external electromagnetic field and electronic structure of the sample. By changing the chemical composition, the electronic structure is modified, and thus the reflectance, absorbance and transmittance change accordingly, as demonstrated in several studies [66–68]. For example, a study aimed at the optical, chemical and structural characterisation of germanium oxide thin films [67], i.e. understanding the effect of the oxygen addition on the optical constants of 100 nm thick, DC-sputtered GeO_x showed a decrease of the refractive index with the oxygen gas fraction (Figure 2.3).
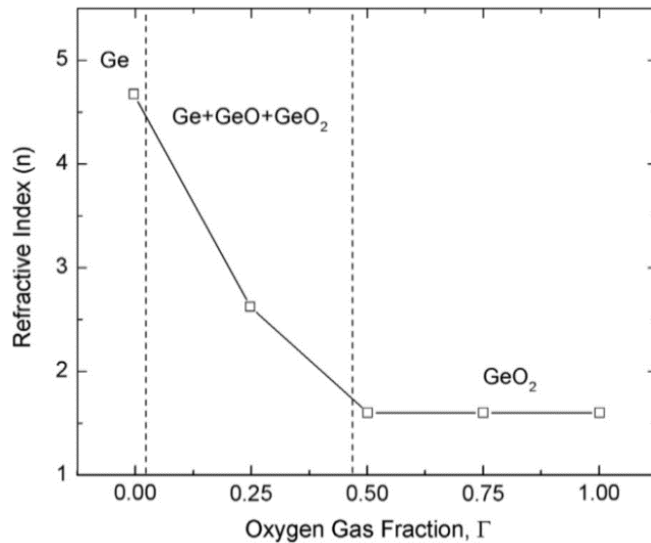
Figure 2.3 The dependence of refractive index (n) on oxygen gas fraction (Γ) at a wavelength of 550 nm. The approximate regions for different film compositions are shown by the dashed lines [67].

In the case of metals it has been shown that the reflectivity of an alloy could be estimated based on the optical constants of pure metals [69], the study in question

focusing on monophasic Au_xM_{1-x} binary gold alloys, where M is silver, platinum and palladium. The authors argue this method is a good starting point when no other data is available; however, more material characteristics contribute to the reflectivity of an alloy, some of them discussed below.

(II) <u>Surface roughness and topography</u>. Depending on the roughness and particle size with respect to the wavelength, the absorption increases either through multiple reflections (when structure size is greater than the wavelength [65]), or by exhibiting an apparent gradual refractive index ("moth-eye"). Surfaces with a structure which mimics the moth eye have a refractive index which varies gradually from unity (i.e. air) to that of the bulk material. The travel of light from one medium to the other can be regarded as the resultant of an infinite series of reflections, each with its own refraction index. For a detailed description, the reader is referred to the work of Wilson and Hutley [70]. When the surface structures are much greater than the incident wavelength, the light is partially absorbed and then further reflected (Figure 2.4a). When the structure size and the wavelength are comparable in size, the rays tend to bend around the structure, also called Rayleigh effect (Figure 2.4b). If there are variations in the lateral spacing and depth of the structure the light will undergo multiple internal reflections (Figure 2.4c) [71].

The presence of well-defined surface structures may lead to the scattering of light, causing energy loss from the laser beam. An increased surface roughness σ_{RMS} leads to an increased scattering coefficient α_{surf}, as shown in Equation (2.4),

$$\alpha_{surf}(\lambda) = \left(\frac{2\pi(n_1 - n_2)\sigma_{RMS}}{\lambda}\right)^2 \tag{2.4}$$

where n_1, n_2 and λ are the refractive index of the film and air and wavelength of the incoming radiation [72].
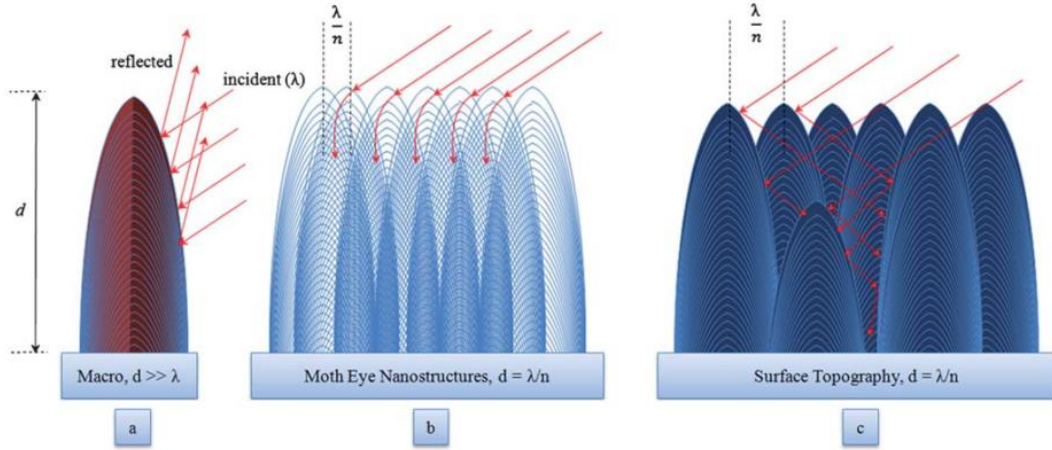
Figure 2.4 (a) Light being reflected away from a microstructure, (b) light interacting with the whole surface due to comparable dimensions, (c) light undergoing multiple internal reflections through a nanostructure pattern [71]. Here d is the structure dimension, λ the wavelength of light and n the refractive index.

(III) <u>Temperature</u>. One study shows an overall decrease in absorptivity at 780 nm with an increase in temperature for three common materials used in the aerospace industry [73]. It is highlighted the importance of correcting for heat losses when measuring absorptivity as a function of temperature. However, the study is limited to temperatures up to 400-500 °C, well below typical ablation temperatures which usually reaches beyond melting temperatures for common metals. Another study showed that a temperature increase in metal samples (Cu and Al) led to an increase in the absorptivity of the material at a given wavelength [74]. In this case, the temperature ranged from room temperature up to the melting point of each metal, and the absorption was measured for IR radiation using a CO_2 laser operating at 10.6 µm. These studies show that variation in temperature

leads to variation in absorptivity; the discrepancies in these two studies could be attributed to a variety of reasons, such as the different wavelength and techniques used.

(IV) Oxide layers. When measuring the absorptivity as a function of temperature for metals there is usually a variation in overall value attributed to the formation of oxide layers on the surface. Both studies discussed in the temperature section highlight the importance of oxide layers when heating metal samples (an example by Rubenchik [73] is shown in Figure 2.5). Yilbas et al. [74] attribute the deviations of reflectivity from the computed values on the growth of an oxide layer on the metallic surface, which can lead to a sudden drop of reflectivity. The influence of oxide layers on the absorption of light is based on the thin-film interference phenomenon; however, for the effect to take place, the thin film must have a thickness of $[(2n + 1)/4]\lambda$, where n is any integer.
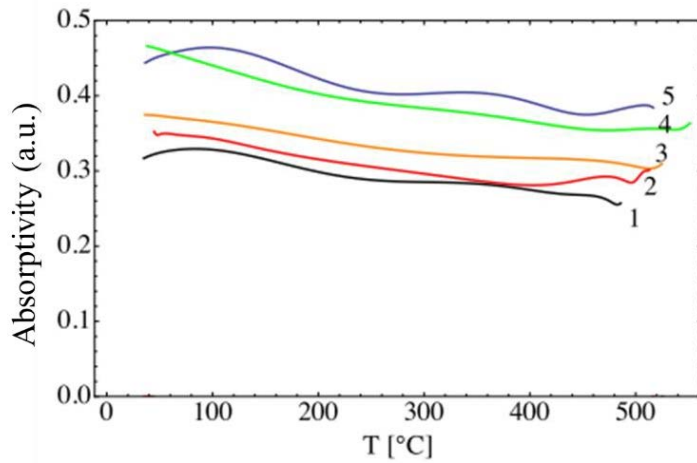
Figure 2.5 Absorptivity of Al sample in several heating and cooling cycles up to ~550 °C. The increase in absorptivity is evidence for the modification of the oxide layer in Al (adapted from [73]).

(V) Laser produced plasma (LPP). It has been reported that for metal films irradiated with IR, a decrease in reflectivity with the laser fluence occurs above the plasma formation threshold [75,76]. Figure 2.6 highlights that Cu has a higher threshold for

plasma formation than Al and Ni, attributed to the breakdown of air in front of the irradiated sample. It is important to note that thermal coupling between the resulting plasma (which usually emits in UV) and the metal surface may occur at lower plasma densities, [77] where LPP converts the IR radiation to UV which is easily absorbed by metals. At higher plasma densities, however, LPP instead completely shields the target by decoupling the beam from the workpiece.

2.2.2 Timescale of energy transfer with respect to the pulse duration

In the previous sub-section, the absorption of energy by the sample has been discussed. Further, the effects occurring after the absorption of radiation, when an energy shift in the lattice occurs and the system returns to an equilibrium state by a variety of mechanisms which dissipate the energy are discussed. These are usually referred to as "material response".
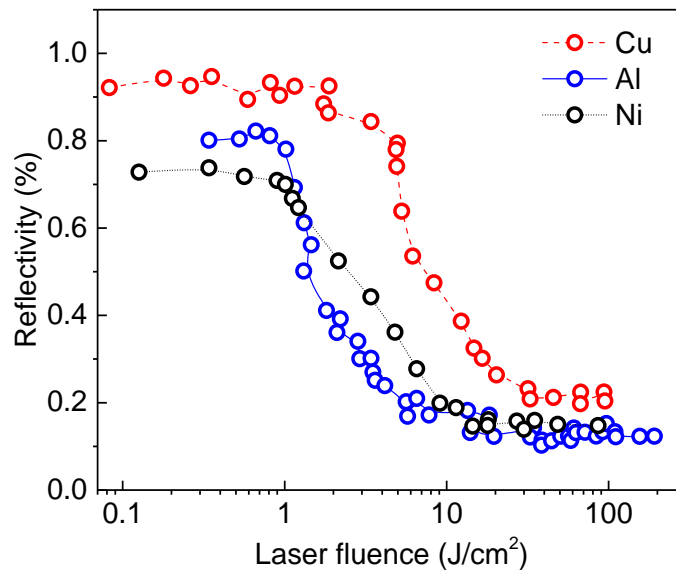
Figure 2.6 Reflectivity of Cu, Al and Ni as a function of laser fluence (50 ns, 1064 nm) for ablation in 1-atm air (adapted from [75,76]).

The material response is given by the pulse duration with respect to the time scale of electron and lattice dynamics [78]. The energy is absorbed by the electrons, and then transferred to the lattice by electron-electron and electron-phonon interactions. For a metal target the lifetime of the excited electrons is in the order of a few femtoseconds [79], and the energy transfer from the electron cloud to the lattice occurs within picoseconds [16]. When the laser pulse is longer than electronic relaxation and electron-phonon interaction times (e.g. tens of nanoseconds), the processes occurring fall under the laws of classical heat transfer, and the material is removed from the target by thermal ablation. A schematic representation of thermal ablation is given in Figure 2.7.
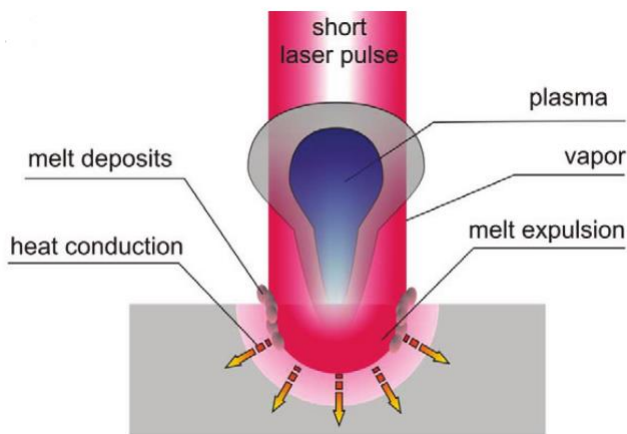
Figure 2.7 Classical beam-matter interaction [39].

The material response in this case is a result of elevated temperatures, and the equilibrium is reached through heat dissipation in the adjacent region. In the coordinate system of the laser beam, the one-dimensional heat equation which describes the temporal and spatial evolution of the temperature inside the material can be written as:

$$\rho(z,t)c(z,t)\frac{\partial T(z,t)}{\partial t} - \nabla[K(z,t)\nabla T(z,t)]$$

$$+ \rho(z,t)c(z,t)v_s\nabla T(z,t) = Q(z,t) \tag{2.5}$$

where ρ is the mass density, c is the specific heat at constant pressure, K is the thermal conductivity and v_s the velocity of the substrate relative to the heat source and Q the heating rate, in which the contributions of heat sources and heat sinks are included [80].

From Equation (2.5), it is seen that in addition to the reflectivity of the sample at the given wavelength discussed in earlier paragraphs (which indicates the amount of energy absorbed by the sample), the thermal properties are also important when evaluating the maximum temperature reached during pulsed laser ablation. These material properties together with the laser pulse temporal and spatial intensity profiles will result in various material responses, such as heating without phase change, melting, material removal through vaporisation and plasma formation [81,82].

2.2.3   Density and thermal properties

Several authors have established a connection between melting temperature and material response to PLA. For nanosecond PLA of various metals in air at atmospheric pressure, one study shows that the plasma formation threshold values (which are only ~0.2 J/cm^2 higher than ablation thresholds for metals irradiated with ns) generally increase with the melting and boiling points of the target material [30],. The same study attributes a decrease in the threshold fluence with a decrease in target density.

A trend was also noticed in PLA of metals with UV radiation, regarding the crater geometry as a function of the melting temperature: the lower the melting point, the larger

the crater diameter and crater depth [31], for both single- and multi-pulse ablation (Figure 2.8).
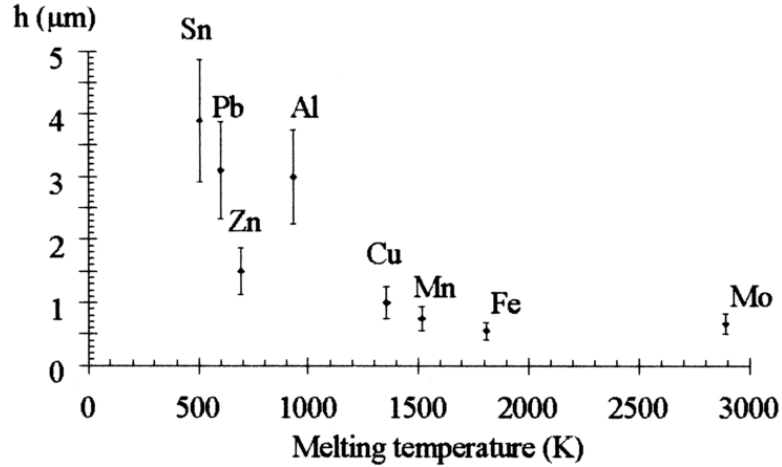
Figure 2.8 Crater depth versus melting temperature, after ten KrF laser pulses [31].

The thermal properties of the sample play a key role in nanosecond PLA: the absorbed energy is stored in a layer of a thickness given by the thermal (or heat) diffusion length $\delta_{th} \approx (2k\tau)^{1/2}$, where τ is the pulse duration and $k = K/\rho c$ the thermal diffusivity. Evaporation occurs when the absorbed energy is larger compared to the latent heat of evaporation, L_v [83], and the ablation depth per pulse Δz_v can be estimated as shown in Equation (2.6). The threshold fluence F_{th} represents the onset of significant evaporation and can be approximated using Equation (2.7), where F_0 represents the absorbed fluence, $A = 1 - R$ is the absorbance and T_m the melting temperature.

$$\Delta z_v \approx \frac{A(F_0 - F_{th})}{\rho L_v} \tag{2.6}$$

$$F_{th} \approx \frac{\rho c \Delta T_m \delta_{th}}{A} \tag{2.7}$$

2.2.4 The vapour cloud and laser produced plasma (LPP)

As the intensity of the laser pulse increases, evaporation and plasma effects become important and have a significant contribution to material removal. The vapour cloud forming at the surface (which, ionised, becomes plasma), creates elevated pressure at the target surface (recoil pressure), which assists in material removal by impinging on the molten surface and thus creating a drag movement of the material towards the edges of the irradiated area. Thus, the material removal (at average intensities) represents a superposition of melt ejection and evaporation. Both the evaporation rate and the recoil pressure are dependent on the temperature of the molten surface and the material density and thermal properties [84].

In machining, the presence of LPP can lead to the shielding of the target from the incoming laser radiation by absorbing its energy [85,86]. The vapour cloud is transparent at low power densities, but as the latter increases so does the amount of energy absorbed by the plume, until it eventually becomes optically thick (e.g. a Cu plasma completely shields the laser from the target around 0.2 GW/cm^2 [85]). This phenomenon becomes even more important for metals, since it has been experimentally shown that the plasma formation threshold is only slightly higher than ablation threshold for metal targets irradiated in air (e.g. 0.8 J/cm^2 and 1.0 J/cm^2 are the ablation and plasma thresholds for titanium ablated in air with ns pulses [87]). Sometimes plasma enhances material removal by transferring this energy to the target (known as plasma coupling). Material removal has been attributed to "assisted plasma etching" by a set of studies, where pure metal targets (Cu, Al, Ni and W) were ablated in air using a Nd:YAG operating at 1064 nm, and a 50 ns temporal pulse width [75,76]. The phenomenon occurred in air (or another background gas), where the plume is confined closer to the target surface, instead of

expanding freely as it is the case in vacuum. Another study done using similar parameters confirms the existence of energy coupling following the ablation of Al with nanosecond pulses, in the single-pulse regime. By measuring the temperature of the target, it was shown that the residual energy is higher in a range of fluences, after which it drops irrespective of the increase in the laser fluence. Again, this effect was enhanced when ablating in air or a background gas (oxygen, helium) at atmospheric pressure [40].

One study dedicated to the investigation of LPP showed that enhanced LPP – workpiece coupling could occur by using subwavelength gratings, which, while highly dependent on the geometry of the surface, contribute to the formation of intense electrostatic fields which then interact with the laser radiation or the LPP [88]. Another study shows that not only nanostructured materials lowered the ablation threshold by limiting the heat dissipation into the bulk, but also its surface morphology led to different plasma characteristics in the same experimental conditions, i.e. the LPP formed by irradiating a nanostructured surface had a shorter emission duration and less intense basic atomic lines compared to a plasma generated from a polished target, as well as higher temperature and density, as shown in Figure 2.9 [89]. As the presence of plasma can improve the absorption and thus the energy transfer from the laser to the target, it is important to keep in mind that there is only a range of power where LPP can facilitate metal machining. This range is likely to vary from a structured to a smooth surface because nanostructured surfaces may facilitate plasma formation and limit the amount of heat dissipation into the bulk.
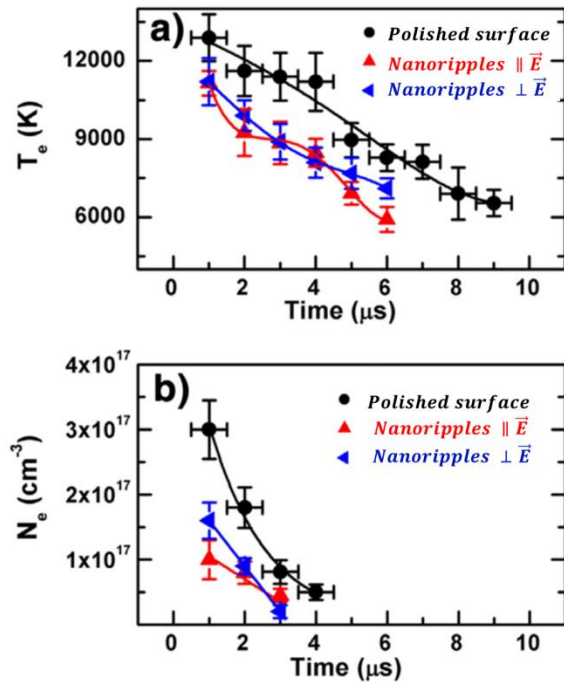
Figure 2.9 Temperature (a) and electron density (b) evolution for plasmas produced on the polished sample (black) and the nanostructured sample depending on the orientation of nanoripples with respect to polarisation (red and blue), adapted from [89].

Up to this point, only the processes characteristic to thermal ablation (in the microsecond-nanosecond range of pulse durations) have been discussed. However, while the phenomena occurring in nanosecond ablation are generally described as thermal, it has been shown that, at shorter pulse durations within the nanosecond regime ($\tau <$ 10 ns), phenomena associated with the non-thermal ablation (specific to sub-nanosecond pulses) may occur. These effects do not make the subjects of the present work, as longer pulse durations are used (i.e. 30 ns and 55 ns). Extensive studies have also been dedicated to ultra-short laser pulses and some example of these processes are the formation of self-organised structures [90], commonly known as laser induced periodic surface structures (LIPSS), characteristic to ultra-fast laser processing, and also material removal by phase

explosion [91–93], which occurs when the material is heated beyond its critical temperature.

Due to minor damage to the area adjacent to the laser beam, as well as minimal heat losses into the bulk, ultra-short laser pulses have been the preferred laser-machining technique for processing of thin films. Despite the higher processing quality, the price and usage cost of an ultra-fast laser are higher compared to a nanosecond laser [94,95], and thus it would be worth investigating the nanosecond PLA of thin films and whether the efficiency can be improved in terms of minimalizing the heat affected area (or heat affected zone – HAZ) and thermal damage to the substrate. Several studies dedicated to this topic are presented in Section 2.4; first, however, the differences between thin film and bulk laser ablation are discussed.

2.3 PARTICULARITIES OF THIN FILM LASER ABLATION

Thin films are widely used nowadays, with new applications emerging, mainly to improve the performance of a material, for a broad range of applications. Common uses of thin films include optical coatings with self-cleaning, anti-fogging or anti-reflective properties [71,96,97], solar cells [98], wear resistant coatings [99] and biological implants [100]. Moreover, as the microelectronic industry becomes more and more demanding, thin films found their way in micro-electro-mechanical systems (MEMS) [101,102]. These devices require accurate micro-manufacturing techniques, and laser processing is a viable choice in terms of speed and reproducibility.

As discussed in Section 2.2, during nanosecond PLA material is mainly removed by thermal processes (heating, melting, evaporation and melt ejection), while non-thermal processed may appear at shorter pulse duration (<10 ns). Thermal processing is associated

with the presence of a heat affected zone (HAZ) around the irradiated spot, where the material properties may change and the presence of re-solidified material, resulting in a poor surface finish [39,103–105]. Hence a large amount of thin films laser processing is carried out using ultra-fast lasers (in the pico- and femtosecond regimes), where the thermal effect is minimal and a higher precision can be achieved [106,107]. Holes drilled in a 100 μm thick steel foil with ns and fs laser pulses are shown in Figure 2.10. However, several studies show that by using an optimised set of laser parameters (among which beam spatial and temporal profile, pulse duration and wavelength) it is possible to obtain high precision features and minimal HAZ when machining thin films using nanosecond laser ablation, thus taking advantage of the lower cost, higher efficiency and well-established technology of nanosecond pulsed lasers [108–110]. As discussed in the previous section, a structured thin film could minimise heat transfer to the substrate – and the size and nature of the structures can be controlled by adjusting the deposition parameters.
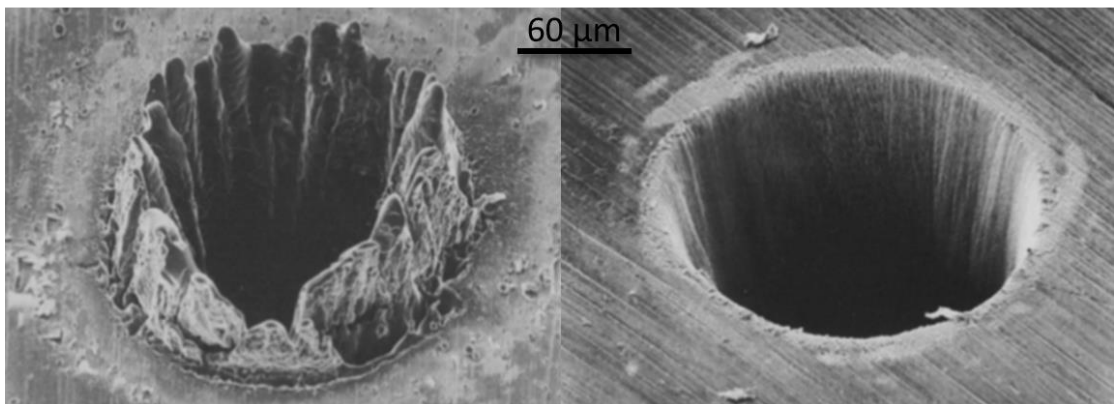
Figure 2.10 Holes drilled in 100 μm steel used to illustrate typical nanosecond (left) and femtosecond (right) ablation features (adapted from [111]).

2.3.1 Film thickness and estimation of the ablation threshold

Numerous studies on nanosecond PLA of thin films report the importance of the film thickness. It is shown that the ablation threshold has a linear increase with the thin film thickness d, up to the point where the latter is equal to the thermal diffusion length [112], when it reaches the ablation threshold of the bulk material. Moreover, when the film thickness decreases below the heat diffusion length δ_{th}, the threshold fluence also depends on the substrate material [113], as its thermal diffusivity will result in a higher or lower amount of heat losses to the substrate, which acts as a heat sink. The amount of energy lost to the substrate depends on the pulse duration τ and it is shown that for a thin film of certain thickness and composition, optimal pulse duration for efficient ablation can be defined [114]. The energy efficiency yield η can be written as shown in Equation (2.8),

$$\frac{1}{\eta} = 1 + \frac{2}{\psi\sqrt{\pi}} \tag{2.8}$$

where $\psi = \rho_f c_f d / \rho_s c_s (k_s \tau)^{1/2}$. Thus, for an efficiency yield $\eta > 1/2$, the value of the pulse duration can be written as shown in Equation (2.9). The subscripts f and s refer to the film and substrate respectively.

$$\tau \leq \frac{\pi}{4}\left(\frac{\rho_f c_f}{\rho_s c_s}\right)^2 \frac{d^2}{k_s} \tag{2.9}$$

Despite the extensive amount of theoretical research and modelling done on laser ablation, few consider nanosecond PLA of thin films. A simple model to estimate the ablation threshold of metal thin films by taking into account physical material properties

as well as film thickness d and losses to the substrate has been shown by Matthias et al. [115]. The authors emphasise the influence of thermal diffusion in thin films and its contribution to the ablation threshold. The assumptions of the model are as follows: *(i)* the damage and ablation thresholds are of thermal origin; *(ii)* lateral heat diffusion is neglected (as is usually the case when the spot size is much larger than the ablation depth); *(iii)* heat losses to the gas layer near the surface are ignored; *(iv)* the temperature rise is uniform within the thin film thickness; *(v)* heat losses to the substrate are taken into account additively; *(iv)* any thermal resistance at the thin film-substrate interface is neglected. The ablation threshold fluence (experimentally determined as the onset of evaporation), can be written using material properties as below (2.10),

$$F_{th} = \frac{\Delta T_v + L_m/\rho_f c_f}{(1 - e^{-\alpha d})(1 - R)} \times \left\{ \left[\rho_f c_f - \left(\frac{\delta_{th,s}}{\delta_{th,f}} \right) \rho_s c_s \right] l_f + \delta_{th,s} \rho_s c_s \right\} \quad (2.10)$$

where ΔT_v is the evaporation temperature, L_m the melting enthalpy; a "thermally active depth" l_f is introduced and is defined in Equation (2.11). The superscripts indicate properties of the thin film and substrate respectively, thus allowing for the approximation to stand for bulk materials as well.

$$l_f = d \quad \text{for} \quad d < \delta_{th,f}$$
$$l_f = \delta_{th,f} \quad \text{for} \quad d \geq \delta_{th,f}$$
$$(2.11)$$

The authors argue that the thermal diffusion length of the thin film $\delta_{th,f}$ and the reflectivity R are the most important material properties when evaluating the threshold fluence. The variation of the ablation threshold with film thickness (for Ni films on fused silica) is shown in Figure 2.11.
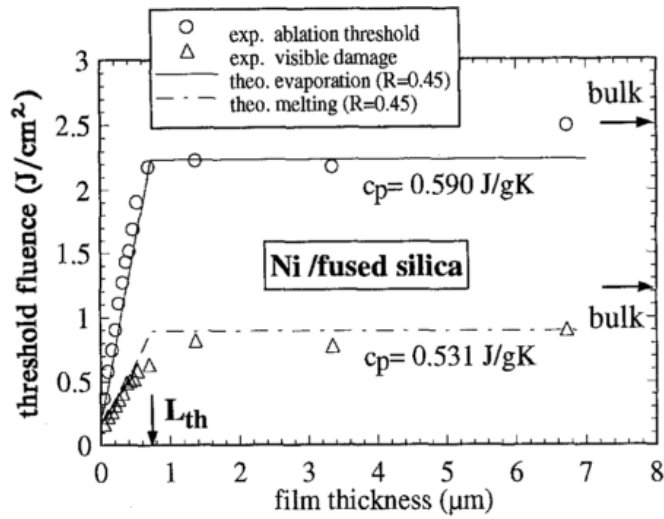
Figure 2.11 Thickness dependence of single shot threshold fluences for visible damage (triangles) and ablation (circles) of Ni films on fused silica [115].

The presented thermal model represents a good start to estimate the ablation threshold of various materials when the optical and thermal properties are known. While the model considers the heat losses to the substrate by including thermal properties of both the thin film and the substrate – however, there are more factors which are likely to play a role, and one of them is the nature of the interface, namely how smooth or rough it is which dictates the surface contact area between the two materials.

In addition to film thickness and how this influences the laser-material interaction, another particularity of the thin films on substrates is represented by the stresses developed during the synthesis process. During ablation, these may lead to deformation of craters and failure of the thin film in the area adjacent to the irradiation spot. For example, the response of single-crystal self-standing chromium film (37 nm) to irradiation with 6 ns laser pulse starts by the formation of parallel domains and by crack formation prior and during melting [116]. The evolution of the crater morphology was studied using a high-speed transmission electron microscope and is shown in Figure 2.12.
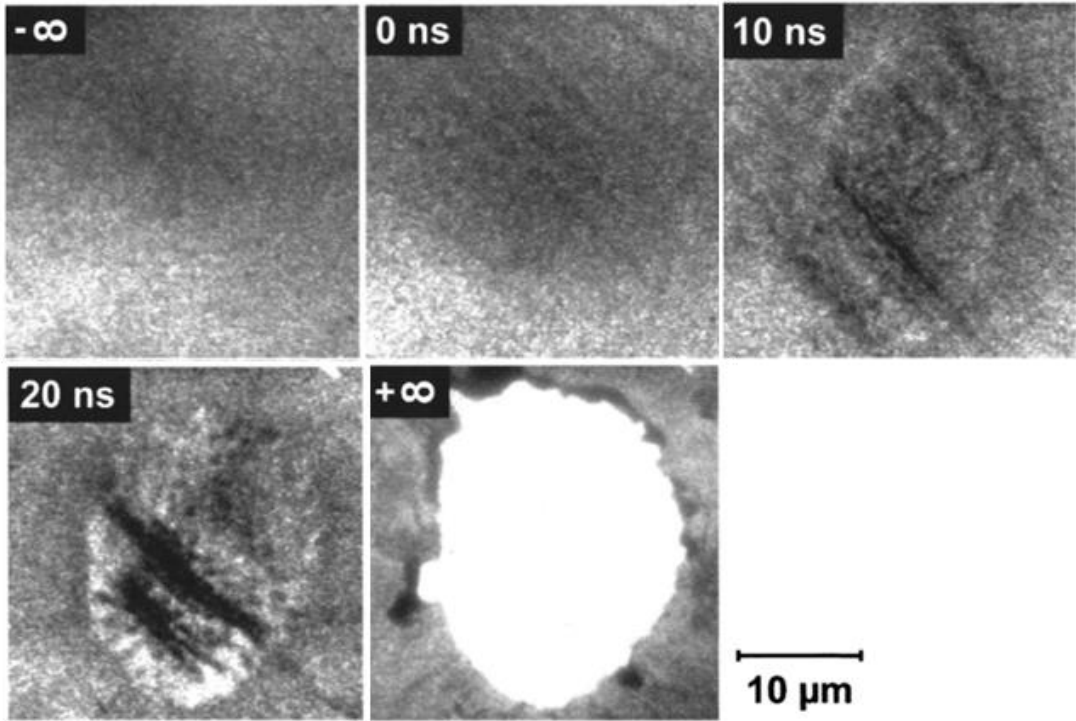
Figure 2.12 Single-frame shots showing early effects in laser-pulsed single crystal chromium film (37 nm): Native crystal (-∞), breaking into parallel domains prior to melting (0 ns), detachment and disintegration of the melt pool (10 and 20 ns). Final hole with ragged edge and ditches (+∞). The moment of electron exposure is counted from the peak of the treating laser pulse. The images were taken from fresh neighbouring regions treated with identical laser pulses (adapted from [116]).

2.3.2 Particularities of thin films with respect to their bulk counterparts

To further discuss PLA on thin films, their particularities with respect to their bulk counterparts needs to be addressed, focusing on the ones relevant in nanosecond PLA (the quantities shown in Equation (2.10)). The film properties relevant to nanosecond laser ablation are given below: (A) density, (B) electrical conductivity, (C) optical properties and (D) thermal conductivity.

(A) <u>Density</u>. The density of thin films is lower than their bulk counterparts, even when deposited by techniques which generally ensure tightly packed films, such as

sputtering [117]. The density is proportional to film thickness and, depending of the material and deposition conditions, a constant value is reached which approaches the bulk density (e.g. 25 nm thick Al films reach a density of 2.58 g/cm^3 when treated above 525 °C, compared to the bulk value of 2.70 g/cm^3). The lower density is explained by the presence of voids which form during the synthesis process. A packing factor $P = (volume\ of\ solid)/(total\ volume\ of\ film\ (solid + voids))$ is used for the measuring the effect of the voids on the film density. For metallic thin films, P is greater than 95% of the respective bulk value ([118], cited in [119]). The packing factor P could be increased during the deposition by increasing the substrate temperature or post-annealing.

(B) <u>Electrical conductivity</u>. The total electrical resistivity of real metals (both bulk and thin film) is the sum of independent scattering processes, i.e. by lattice vibrations and impurities. Generally thin metallic films have a higher resistivity than their bulk counterparts, but the differences are relatively small. The difference originates in the size phenomena which arise because of physically small dimensions involved (known as the classical size effect). The method of thin film preparation (mostly the deposition conditions) plays an important role as well, since this can affect, among others, the crystallinity, defect concentration and grain morphology [120]. These thin film properties may shorten the mean electron path of the electron in the metal, which decreases the electrical conductivity of the material.

(C) <u>Optical properties</u>. As their bulk counterparts, thin film optical properties are governed by the interaction of an external EM field with their electronic structure (discussed in Section 2.2.1). Thus the same film parameters discussed in the previous paragraph (which are usually a result of the synthesis process) will affect the optical properties of metal thin films (i.e. scattering caused by impurities or grain boundaries

[121]). Moreover, significant sensitivity of the reflectivity to the deposition conditions has been observed in metals which have higher affinity for oxygen such as Al [122]. It has been shown that a sharp decrease in reflectivity can occur due to a specific surface morphology, similar to the sub-wavelength structures present on the eyes of a moth [123,124], which act as an anti-reflection thin film coating.

(D) Thermal conductivity. In metals both electrons and phonons are responsible for *heat transport*; however, the electrons dominate the process, not only in bulk metals but also in thin films. The connection between electrical and thermal conductivity (σ and K respectively) at a given temperature T is called the Wiedemann-Franz (WF) law (2.12),

$$\frac{K}{\sigma} = LT \qquad (2.12)$$

where the proportionality constant L is the Lorenz number [125]. The exact value for this constant is disputed (for example see [126]), but generally it is in the range of $L = 2.44 \times 10^{-8} \, W\Omega/K^2$. Like electrical conductivity, thermal conductivity is influenced by the scattering of electrons at grain boundary and surface scattering of electrons and generally it decreases with film thickness. Not only it has been empirically shown that the thermal response of thin films is similar to the bulk one when the thickness is larger than the heat diffusion length, but also a more pronounced lateral heat diffusion is observed at smaller thicknesses compared to the heat diffusion length [127].

Another aspect which may cause a significant difference between PLA on bulk and thin films is represented by the heat losses to the substrate. The thermal transfer between the thin film and the substrate varies with their thermal properties, as well as with the

roughness of the interface (e.g. a rougher surface leads to a slower heat transfer due to less contact area) [128].

2.4 NANOSECOND LASER ABLATION OF THIN FILMS

The use of nanosecond (ns) pulses in the laser ablation of thin film would allow high quality machining to be achieved at lower costs compared to ultra-short lasers. In this context, the challenges are to minimise damage to the substrate and/or the extent of the lateral HAZ [129]. For example an investigation of oxide thin film removal from a silicon substrate (with focus on solar cell materials) revealed that parameter optimisation when using ns lasers was challenging, i.e. no optimal removal could be achieved [130]. Several different wavelengths and pulse durations were used for optimisation of thin films processing, with focus on optimal edge quality without damaging the substrate or adjacent areas. The quality was assessed by considering the ablation threshold, debris and heat-induced damage and a summary of the results is given in Figure 2.13, where good quality is assessed to be a relatively homogeneous ablated region with minimal re-deposited melt and damage to the substrate.

pulse duration	parameter	SiO$_2$	SiN$_x$	PEDOT:PSS	ZnO	SnO$_2$	ITO
ps	laser 1, 515 nm, 7ps irr. side: layer	🟢	🟢	🟢	🟡	🟢	🟢
	ε [J/mm^3]	22	75	55	49	11	66
	laser 2, 1030 nm, 7ps irr. side: layer	🟢	🟢	🟢	🟡	🟢	🟢
	ε [J/mm^3]	36	128	96	20	14	57
sub-ns	laser 3, 532 nm, 600 ps irr. side: layer	🟡	🟡	🟢	🟡	🟡	🟢
	ε [J/mm^3]	67	64	77	9	19	74
ns	laser 4, 1064 nm, 30 ns irr. side: layer	🔴	🔴	X	🔴	🔴	🟡
	ε [J/mm^3]	84	696	-	75	77	250
	laser 4, 1064 nm, 30 ns irr. side: glass	X	X	X	🟢	🟢	🟢
	ε [J/mm^3]	-	-		75	51	300
	laser 5, 532 nm, 10 ns irr. side: layer	🔴	🔴	X	🔴	🟢	🟡
	ε [J/mm^3]	172	304	-	120	27	262
	laser 5, 532 nm, 10 ns irr. side: glass	X	X	X	🟡	🟢	🟡
	ε [J/mm^3]	-	-	-	55	17	378

Figure 2.13 A tentative assessment of results, based on SEM micrographs of the ablated regions; coloured dots represent the quality of the processing in a traffic light scheme. Green is good, red is not good and yellow is not optimal [130]. On the right are shown examples of a "good" (top) and "bad" (bottom) surface quality after ablation.

As demonstrated by Rung et al. [131], thin film laser patterning without damage to the substrate and minimal heat-affected zone could be achieved with ns pulses by using beam shaping optics, i.e. a Top-Hat beam profile instead of the more common Gaussian laser beam (Figure 2.14), and this would contribute to a reduced HAZ and minimal damage to the substrate. However, even when using beam shaping optics, optimal results were obtained by irradiation from the substrate side, which implies that the substrate of choice should be transparent at the laser wavelength (e.g. soda-lime glass) [132].

Not only it is not always practical to irradiate from the substrate side (e.g. in functional coatings used to achieve hydrophobic [133] or antibacterial surfaces [134]), but also beam shaping optics require higher investment, are difficult to calibrate and adapt to industrial lasers. It would thus be of interest to analyse the behaviour of thin films on substrate when irradiated with nanosecond, Gaussian pulses, and to further understand what physical properties and morphological or topographical features contribute to efficient thin film machining.
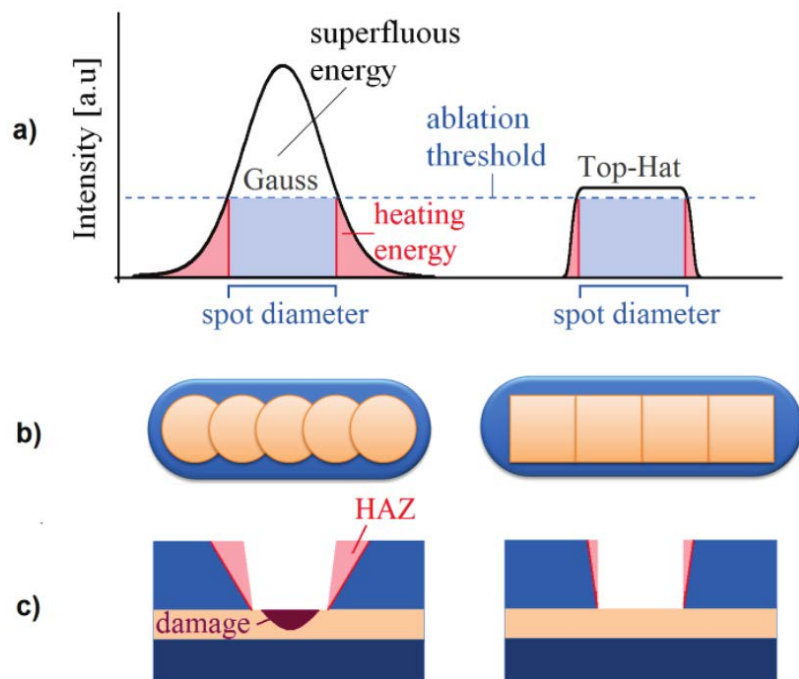
Figure 2.14 Different ablation behaviour of thin films for Gaussian (left) and Top-Hat (right) laser beam profiles. (a) Cross section of laser beam profiles, (b) ablated line with circular and rectangular footprint,(c) schematic cross section of processed material system [131].

Another study which highlights how the quality of ablated regions can be improved is focused on selective ablation of multi-layered structures using conventional ns lasers. This has been achieved when the individual films had different structures,

namely gold nanoparticle (1-3 nm) films, sintered and unsintered [135]. The latter showed a much lower ablation threshold and "cleaner" edges compared to the sintered film (which resembles a typical continuous film), which the authors attributed to a change in the material structure (e.g. weak bonding between the nanoparticles).

While not the central aim of the present work, the patterning of thin films using a commercial laser (operating in infrared with pulse width in the range of ns) will be discussed. It is important to note that extensive studies on laser-material interaction and workpiece response to irradiation have been carried out, aimed at gaining a better understanding of various aspects of laser ablation (usually how variation of laser wavelength, energy or fluence in different atmospheres influence the ablation result). However, only few report consistent results on crater morphology or geometry (see, for example [136,137]), and thus do not provide sufficient information. Thus, the present work will first obtain reference information from the pure thin films and extend the results to binary and ternary material libraries. The binary studies are aimed at showing how changes in chemical composition affect the crater geometry and morphology for both a smooth and structured film. It will also analyse how a sudden transition in film morphology affects the crater shape when the variation in chemical composition is minimal. Finally, the material response of two ternary libraries will be assessed.

3 MATERIALS AND METHODS

This chapter contains detailed information on the materials used (such as bulk properties and thin film properties, synthesis and characterisation), information on laser processing and characterisation techniques used in the research. The aspects related to materials and methods common to all chapters are discussed. Further information on specific experimental parameters (e.g. deposition conditions for thin films or laser parameters) is given in the beginning of each chapter.

3.1 SYNTHESIS OF THIN FILM MATERIAL LIBRARIES BY PHYSICAL VAPOUR DEPOSITION

Physical vapour deposition (i.e. magnetron sputtering) was chosen as it is a well-established and extremely versatile coating technique, where film composition, structure and thickness are easily adjusted by varying deposition parameters such as deposition pressure or substrate temperature. The samples studied in this work are three pure films (Cu, Al, Ni), their corresponding binaries with compositional gradient (Cu-Ni, Ni-Al, Cu-Al) and two ternary alloys, Cu-Ni-Al and Cu-Al-Zr. The samples were studied in an ascending scale of complexity, not only due to the numerous processes which make ablation difficult to characterise and quantify, but also because of variations that appear even in the simplest thin films due to their quasi bi-dimensionality. The metals were chosen due to their different properties relevant to thermal ablation (e.g. density or thermal diffusivity) and to their use in both pure and alloyed forms. The ternary alloys are, for some chemical compositions, either shape memory alloys (Cu-Ni-Al) or bulk metallic glasses (Cu-Al-Zr).

The thin film PVD coatings were co-sputtered using a magnetron deposition technique (Figure 3.1). A Mantis QPREP ultra-high vacuum chamber was used with three magnetron CUSP sources (one RF and two DC cathodes). Each source has a 75-mm diameter and 2-3 mm thick high purity target mounted on top (aluminium, copper and nickel – 99.95%, 99.99% and 99.95% purity respectively). The magnetron heads are water cooled to allow temperature control of the targets during the process.
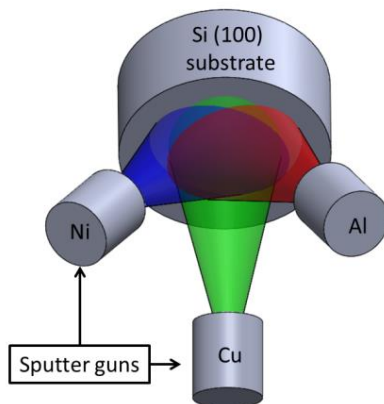
Figure 3.1 Schematic representation of the sputtering setup for the ternary material libraries.

A 100-mm diameter and 525 µm thickness single crystal silicon wafer with <1 0 0> orientation was used as a substrate. The surface was cleaned by immersing the substrate into consecutive acetone and isopropanol baths. The substrate holder was kept at room temperature. For the synthesis of uniform (pure metal) thin films the substrate was rotated with 2 RPM during the process to improve film thickness uniformity across the surface. For the combinatorial thin films libraries, the gradient was obtained by decreasing the target-to-substrate distance (8 cm) and without substrate rotation. The chamber was pumped down to below 10^{-6} mbar base pressure before each deposition. The process was set to ~10^{-3} mbar pressure by flowing high purity argon into the magnetron

heads. The chamber pressure was regulated by a throttle valve. The deposition parameters for particular samples are given in their corresponding chapters (pure films – Chapter 4, binary films – Chapter 5 and ternary films – Chapter 6).

3.2 NANOSECOND LASER ABLATION

3.2.1 Equipment

Laser ablation of the samples was performed with a ns laser operating in the near infrared, instead of using ultra-short pulse durations which are usually preferred in thin film machining. In addition to the advantages of using a ns laser listed in Section 2.3, this choice allowed further analysis of heat transfer to the silicon wafer and to the area adjacent to the irradiation spot.

For laser ablation experiments on the pure (Chapter 4) and binary samples (Chapter 5) the short-pulse laser integrated in the LASEA micro-machining platform was used. The ns laser source is a SPI redENERGY G4 50W HS series S-type air-cooled and with an optical seed pulse generated by a single-mode semiconductor (master-oscillator) laser diode [138]. The nominal wavelength is 1064 nm and the pulse duration can be adjusted between 15 ns and 220 ns by selecting from 25 pre-defined waveforms. Technical specifications of the laser source are given in Table 3.1. The laser travels through the beam delivery path and interacts with the sample at a normal angle as shown in Figure 3.2. To achieve accurate and highly dynamic beam movements a Newson 3D optical beam deflection system is integrated in the machining platform. A similar system was used for ablating the ternary samples (Chapter 6).

Table 3.1 Product parameters for SPI redENERGY G4 50W HS series S-type pulsed fibre laser [139].

Parameter	Value
Wavelength (nm)	1064
Beam quality (M^2)	<1.3
Rated average power (W)	50
Maximum peak power (kW)	>10
Maximum pulse energy (mJ)	>0.7
Pulse repetition frequency range (kHz)	1-1000
Pulse duration range (ns)	10-240

All laser ablation experiments were carried out in air at atmospheric pressure. Identical processing parameters (i.e. wavelength, pulse duration, repetition rate and spot size) were used whenever possible, although small variations in spot size and shape were noticed, dependent of beam alignment. The average power was measured before every experiment using a Gentec-EO Uno laser power meter, which has a resolution of 1 pW on photodetector and 1 mW on the thermal detector. The beam had a Gaussian spatial profile and its diameter was measured using a Beam'R2 (DataRay Inc.) slit scan beam profiler with 0.1 µm resolution and 0.5 µm accuracy.
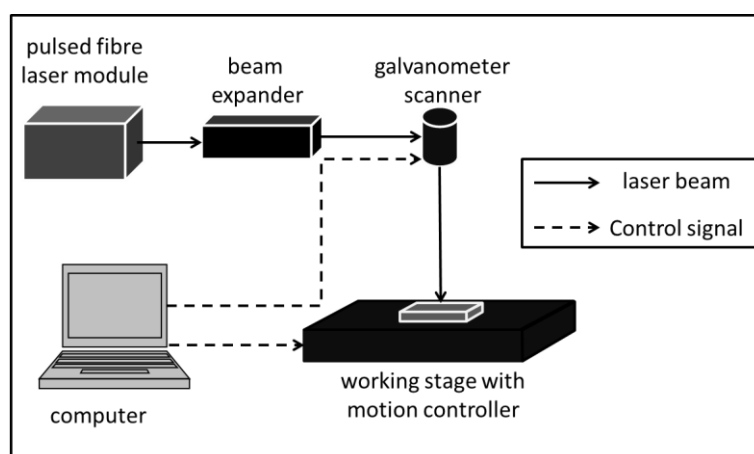
Figure 3.2 Schematic representation of the experimental laser setup.

3.2.2 Laser processing considerations

This section describes the general approach to laser ablation undertaken in this work, on pure (Chapter 4) and binary thin films (Chapter 5), while the processing of the ternary samples is described in Chapter 6.

Single pulse ablated craters were obtained by using 15 kHz repetition rate, which also resulted in no overlapping of the heat affected areas. Ten values for the average pulse power were chosen (between 1.15 W - 100% and 0.23 W – 55%) with a step of 5% in the average power, and ten lines of equally spaced, individual craters were ablated (Figure 3.3).
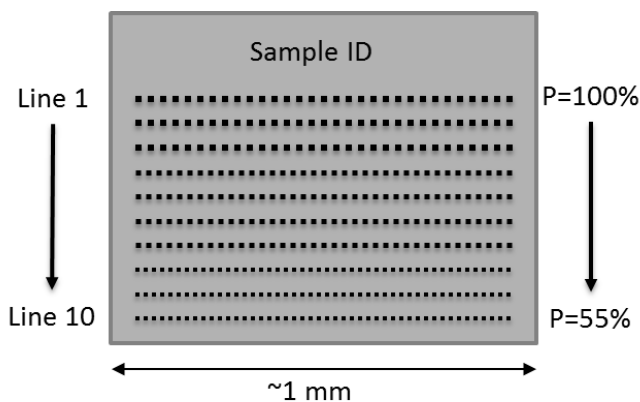
Figure 3.3 Schematic representation of laser patterning.

The choice in the power step ensured that the ablation threshold for all samples were in the chosen range of powers. Line length (~0.8 mm, ~60 craters) was chosen as to have enough craters available for further investigations, while avoiding the beginning and end of line where acceleration/deceleration may lead to overlapping craters. In order to choose the pulse length, several waveforms were tested (by using the same ten lines pattern), and the minimum duration where ablation was observed was chosen for further

patterning. The minimum pulse duration where material removal was observed was 55 ns for the pure and binary samples.

The pattern with the optimal pulse duration (minimum depth penetration for which material removal was achieved) was then used to ablate the pure metals and the samples with chemical composition. The variation in power enabled coverage of ablation phenomena from heat damage to the thin film without melting (lowest power) to strong ablation (at higher average powers). When studying the material libraries, the variation in chemical composition covered by a set of lines was less than 1 at. %, therefore, the chemical composition is considered constant. The pattern was repeated on areas with "extreme" chemical composition and in the centre of the sample. Based on the geometry results (discussed in Section 3.3.4) a line (with a specific average power) was then chosen and used to pattern the whole composition gradient.

Beam diameter in focus was extracted from the beam Figure 3.4. Two sets of data (corresponding to x and y axes) were plotted in OriginPro and fitted using a Gaussian function. The beam diameter in focus ϕ is the 4σ of the function (according to the ISO 11146 international standard for beam width). The average pulse power P, repetition rate f and $S = \pi\phi^2/4$ the spot area in the focal plane are then used to calculate the laser fluence $F_L = 2P/fS$.
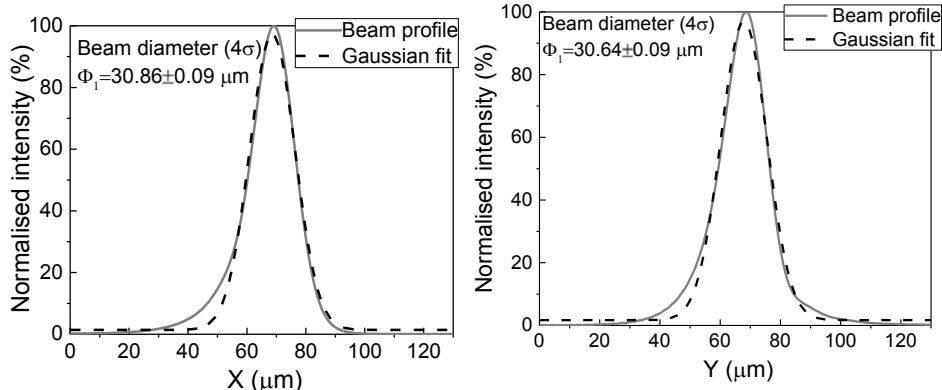
Figure 3.4 Typical intensity profiles of the laser beam (corresponding to x-left and y-right axes) measured in this work.

3.3 CHARACTERISATION TECHNIQUES

Characterisation of the as-deposited thin film was carried out in terms of chemical composition, thickness, reflectivity and surface and cross-sectional morphology, as these properties are highly likely to influence the material response (discussed in Section 2.3). While thin film characterisation can be very time consuming, the characterisation methods used in this work were chosen as to provide reliable information, while maintaining a manageable number of experiments, to make the method presented in this thesis usable by both material scientists and engineers.

3.3.1 Measurement of chemical composition and thin film thickness

Two complementary methods were needed to determine the chemical composition and the film thickness, to achieve a high number of reliable measurements in a reasonable amount of time. A convenient way to measure both parameters is X-ray fluorescence spectroscopy (XRF) as the method is rapid and requires minimal sample preparation. The basis of XRF analysis is secondary (or characteristic) X-ray emission. Specifically, the target is irradiated with energetic X-rays capable of dislocating an

electron from the inner orbital shells of an atom (K or L). The vacancy is then occupied

by an electron from an outer shell resulting in the emission of X-rays (Figure 3.5a). These

X-rays are characteristic to each element and are used for quantitative and qualitative

analysis of a sample. The apparatus used was a FISCHERSCOPE X-RAY XDV-µ

energy-dispersive x-ray measuring instrument for which a schematic representation is

shown in Figure 3.5b. The sample was placed on a programmable *XY* stage, and

positioning was achieved by high-resolution CCD camera together with the incorporated

laser pointer acting as a positioning aid. The measurement spot was ~20 µm and the

element range is Al (13) to U (92) [140]. Based on the chemical composition and known

density of each element, the software also computes the thin film thickness. While the

method is suitable for copper, nickel and binary Cu-Ni films, aluminium is within the

detecting limit of the apparatus so additional methods had to be used.

(a) (b)
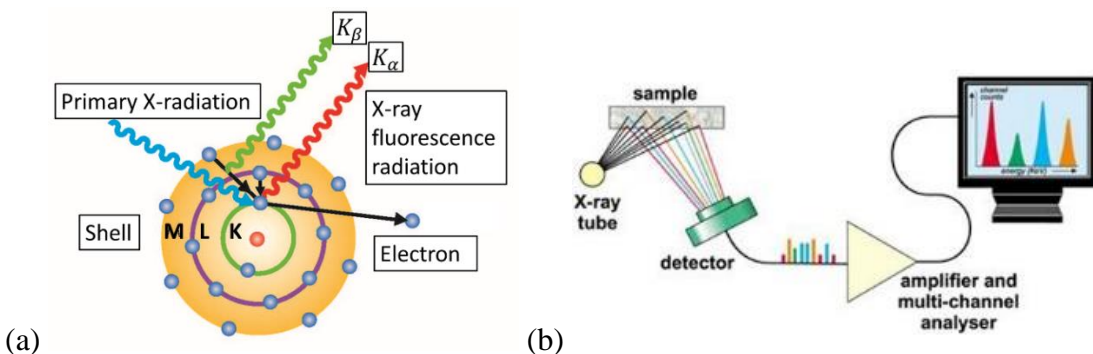
Figure 3.5 Schematic representation of X-ray generation (adapted from [141]) (a). Schematic representation of an energy-dispersive x-ray measuring instrument (b) [142].

For recording the change in Al percentage across the surface, an Oxford Inca 300

energy-dispersive X-ray spectroscopy system (EDS/EDX), equipped on a Philips XL30

scanning electron microscope (SEM) (described in section 3.3.3) was used. The only

difference in the working principle compared to the XRF technique is the creation of the

vacancy in the atom: in EDX an electron beam is interacting with the sample and inner shell electrons are thus removed by collisions with beam electrons. EDX measurements were recorded close to the ablated craters, but outside the heat affected zone (Figure 3.6).
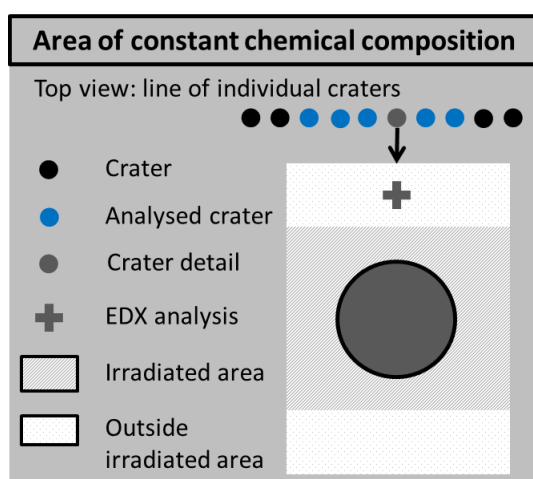
Figure 3.6 Schematic representation of a line of individual footprints (top view).

An acceleration voltage of 20 kV was used to ensure accurate elemental identification (i.e. the minimum beam current should not be lower than twice the maximum excitation energy of the elements present in the specimen). The recommended working distance of 10 mm and 5 spot size were used as to obtain maximum X-ray signal [143].

For additional thickness measurements, a Dektak 3ST surface profiler was used. The measuring system is equipped with a 2.5 μm radius diamond stylus [144]. The thin film was removed from the substrate in several places by scratching 1 mm wide lines. To image the site of interest coarse manual alignment followed by automatic fine adjustments were used. Scan length was 2 mm, with 0.5 mm on each side of the scratch for levelling and thickness measurement. The reported result represents the arithmetic average of multiple measurements of each line.

3.3.2   Measurement of thin film reflectivity

The reflectivity of the sample was measured using a Bruker HYPERION-series FT-IR microscope equipped on a Bruker VERTEX 70 FT-IR spectrometer and controlled by the OPUS software. The supplied gold mirror sample was first used to record the reference spectrum (100% reflectivity). The mirror was placed on the stage and the height was adjusted until the sample was in focus and the maximum signal was achieved. A background signal was then recorded, and all other values were measured with respect to the reference spectrum. The thin film was then placed on the stage and the height was readjusted until the sample was in focus. The reflectivity was measured between 1000 and 1100 nm as to include the laser wavelength (1064 nm). The reported values throughout this work represent the measured reflectivity at the laser wavelength. A standard 15x objective was used and the reflectivity was measured near the laser pattern in an area of 0.5x0.5 mm. The sample was aligned using the optical microscope to avoid any debris which may have been present on the surface because of material splatter during ablation.

3.3.3   Examination of surface and cross-sectional morphology

Scanning electron microscopy was used to evaluate the surface and cross-sectional morphology of thin films, as both play a significant role in ns PLA in terms of reflectivity and heat transfer. In a scanning electron microscope electrons and magnetic lenses are used to form and focus an electron beam (Figure 3.7). When the electron beam interacts with the sample, electrons and X-rays are emitted. Secondary electrons have low energies (<50kV) yet provide a high intensity of the detected signal. The secondary electrons are used for the topographic characterisation of the specimens. The resulting image is formed based on the differences in topography with respect the area tilt.

Backscattered electrons have higher energies and their yield varies with the specimen's atomic number. Thus, they can be used for visual identification of elements present in the sample (Z-contrast). Characteristic X-rays are used to carry out elemental analysis, similar to the XRF described in Section 3.3.1.

The instrument used was a Philips XL30 environmental SEM equipped with a field emission gun (ESEM-FEG). This type of electron gun consists of a point-source tungsten cathode coated with zirconia. It enables higher resolution images to be achieved by providing a higher current density, higher brightness and highly spatial coherence of the electron beam. A resolution of 2 nm can be achieved when using 30kV acceleration voltage.
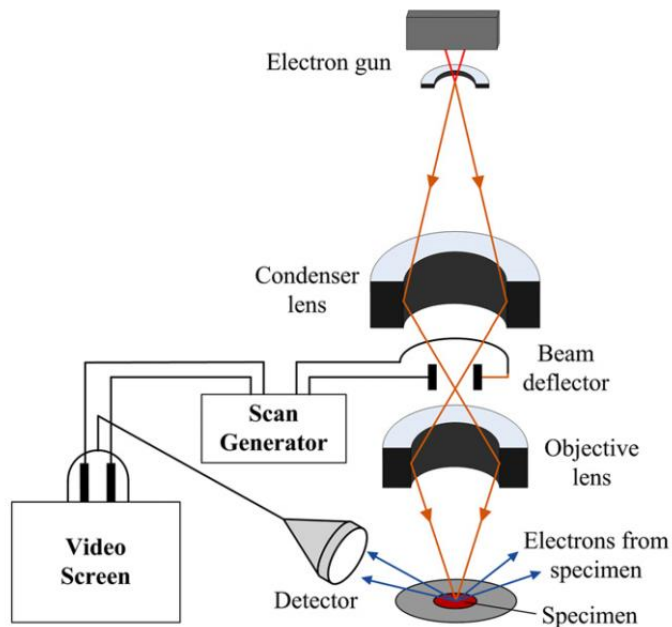
Figure 3.7 Schematic representation of the SEM working principle [145].

Crater cross sections were used to assess the crater penetration into the silicon substrate and/or the extent of the HAZ below the ablated region. The crater cross sections

were prepared via focused ion beam (FIB) technique, using a dual beam SEM-FIB Tescan Vela instrument or a dual beam SEM/FIB (FEI) Strata DB235 instrument.

A focused ion beam is similar in the working principle with a scanning electron microscope but uses gallium ions instead of electrons. This makes it inherently destructive to the sample, even when used for imaging [146]. Hence in this work the FIB was used only for milling pockets in the thin film to enable observation of the sub-surface.

The specimens were prepared in similar manners for both SEM and FIB techniques. The wafers were cleaved to dimensions suitable for the vacuum chamber using a diamond tip. As all thin films were conductive, no additional coating (e.g. Pt) was necessary. The samples were attached on the sample holder using double-sided adhesive conductive tape (either copper or aluminium), to ensure minimal sample charging during the processing and imaging.

The samples were mounted inside the vacuum chamber followed by the adjustment of the focus and working distance. A relative spot size of 3 (where 1 is the smallest spot size the instrument can generate at the selected accelerating voltage) and an accelerating voltage of 10 kV were used for specimen imaging. To achieve higher resolution the working distance used was between 6 mm and 8 mm. Before recording an image, the focus and astigmatism of the beam were adjusted at a higher magnification to ensure optimal image quality.

Cross-sections of the ablated craters were then prepared via focused ion beam. After placing the samples in the vacuum chamber and focusing the beam, a two-step milling approach was used. First, a rough cutting step with high Ga-ion beam (30 kV beam and 0.5 nA/3 nA probe current for the pure and ternary films respectively) was used

to mill a rectangular trench, followed by a fine polishing step (30 kV and 0.1 nA/1nA for the pure and ternary films respectively) in the area of interest.

3.3.4 Measurement of crater geometry and volume

Crater geometry (depth and diameter) and the amount of removed material were measured using *Alicona InfiniteFocus*, an optical 3D micro coordinate system based on focus variation method (Figure 3.8). The system combines the small depth of focus of an optical microscope with vertical movement of scan head to create a 3D image of the workpiece. A detailed description from the manufacturer can be found in [147]. This method allowed for a high number of measurements to be carried out in a reasonable amount of time, compared to more accurate yet more time-consuming techniques (e.g. atomic force microscopy).
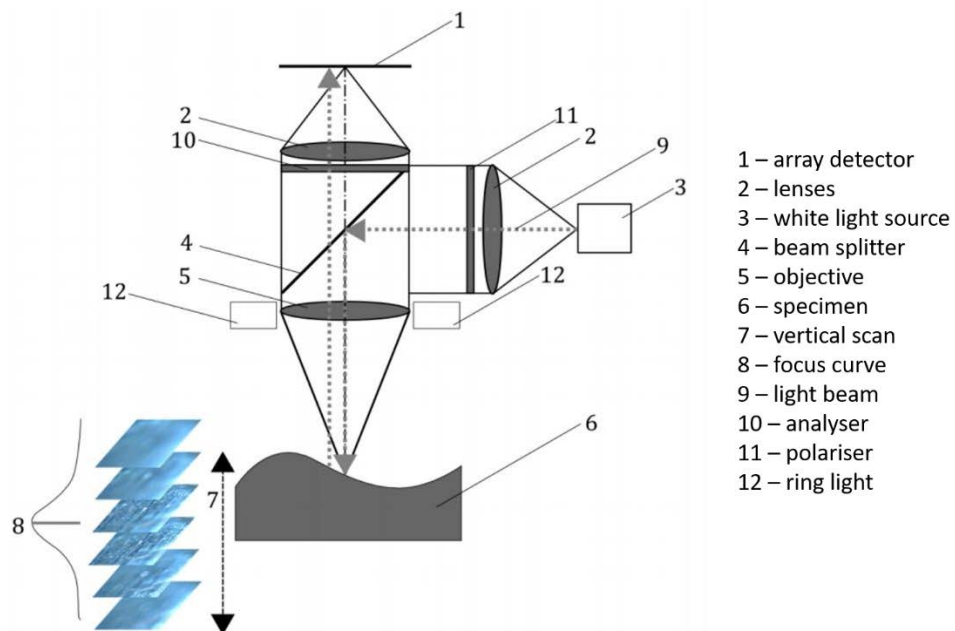
Figure 3.8 Schematic representation of a focus variation microscope (Alicona InfiniteFocus (adapted from [147]).

To collect the data the highest available magnification of 100x objective was used with corresponding resolutions of 20 nm vertical and 1.14 µm lateral. The samples were placed on the *XY* computer-controlled stage. Focus was achieved using the Z-module of the microscope. Light intensity was optimised so at any *Z* position the sample was well illuminated. The most common issue encountered during the measurements was too much light being reflected resulting in missing data from the general image field, which usually occurred when the analysed surface was very smooth. This limitation was countered by using the incorporated polariser for all samples, irrespective of their surface morphology. The measured area contained several lines (3-5) and 10-15 craters on each line, and it was positioned in the centre of the pattern to avoid distortion of footprints caused by acceleration or deceleration of the beam.

Data post-processing was carried out on *Alicona – IF-MeasureSuite*. In the first place, a second-degree polynomial function was then used to level the surface. Slight tilting occurred because of variations in the film thickness, a particularity of compositional gradients. Thus, the function was chosen based on the geometry of the sputtering process.

Crater 2D profiles were extracted from the 3D measurements and were used to measure crater depth and internal diameter (Figure 3.9). The latter usually show significant variations, a consequence of re-deposited material on the crater walls. The diameter of the irradiated spot (top view) was thus analysed further.

The volume measurement feature of *Alicona – IF-MeasureSuite* was used to quantify the amount of removed material. Using a soap-film reference plane (which uses software algorithm for identification of a plane surface), the resultant ablated volume was calculated as the difference between the crater volume beneath the surface, and the

volume of the rim of re-solidified material, which rises above the target surface, as shown in Figure 3.10. Further data post processing and analysis has been done using MS Excel and OriginPro software. The reported values were averaged from 10-12 individual measurements and the standard deviation is indicated on all graphs as *y* error bars.

(a)   (b)
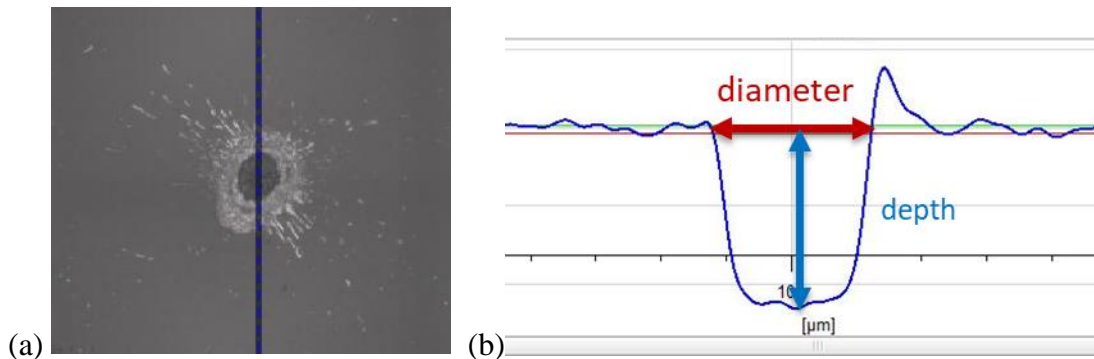
Figure 3.9 Extraction of 2D profile from the 3D dataset (a). Measurement of crater depth and diameter (b).

The method presented had mainly two limitations, which were dealt with accordingly. (*i*) Samples with very smooth surfaces (such as a silicon wafer of the Cu-Ni binary thin film) were difficult to analyse as a large quantity of light is reflected in the detector. The issue was countered by using the polarizer, which generally requires higher exposure and thus compensates for a very smooth surface structure [148]. (*ii*) Light cannot reach underneath the features, so some aspects of crater morphology were shown using other characterisation methods (i.e. crater cross sections analysed using scanning electron microscope). This drawback was also reflected in the measured crater volume, and it is discussed separately in the corresponding sections.
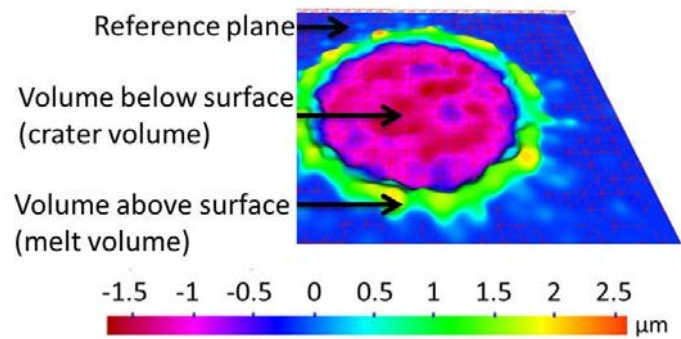
Figure 3.10 Schematic representation of volume measurement. The reference plane parallel to the surface splits the crater in two parts: removed material beneath the surface (crater volume), and re-solidified material that rises above the target surface (melt volume).

4 LASER ABLATION OF PURE COPPER, ALUMINIUM AND NICKEL THIN FILMS

Machining of thin films using laser ablation is typically achieved with sub-picosecond laser pulses or by using top-hat spatial beam profiles. In contrast, this chapter is focused on the machining of thin copper, aluminium and nickel with near-infrared nanosecond pulsed laser with a Gaussian beam profile. The workpiece response (i.e. variations in crater geometry, volume and morphology) with respect to the material properties and film microstructure was investigated. The results revealed similarities between craters in Cu and Al which are different from craters in Ni. The differences in crater geometry were attributed to the combined effects of laser scattering at the surface, thermal diffusivity of the metals and the presence of the thermal barrier between the thin film and the substrate. A preferential lateral heat transfer for the Ni films compared to the more common vertical one in Cu and Al films has been identified. These findings were used as a starting point when analysing ns laser ablation of material libraries, to address the issue of lack of comparable data in literature.

4.1 EXPERIMENTAL DETAILS

The thin films were sputtered using the parameters given in Table 4.1. The identical laser processing parameters are 1064 nm wavelength, 55 ns pulse duration, 15 kHz repetition rate and average power between 0.23 W and 1.15 W given in Table 4.2.

Table 4.1 Specific process parameters used in the deposition of the pure thin films.

	Cu	**Al**	**Ni**
Base pressure (mbar)	1×10^{-7}	5×10^{-7}	8.5×10^{-7}
Gas used	Ar		
Flow rate (sccm)	15		
Sputtering pressure (mbar)	5×10^{-3}		
Deposition time (min)	330	330	480
Sputtering power (W)	40.1(DC)	85.6 (DC)	150 (RF)
Substrate temperature	Room temperature		
Substrate	Si (100)		

Table 4.2 Average pulse power for the ten set of crater lines used to process the thin films.

% of maximum power per pulse	55	60	65	70	75	80	85	90	95	100
Average power (W)	0.23	0.32	0.42	0.52	0.62	0.72	0.83	0.94	1.05	1.15

4.2 MATERIAL PROPERTIES AND ESTIMATION OF THE ABLATION THRESHOLD

While identical processing parameters were used to ablate the thin films, it must be taken into consideration that the effective energy delivered to the sample (which is similar to laser fluence) is diminished by reflection of beam at the surface. In addition, each material has a different threshold for phenomena such as damage and ablation. Thus, for the comparison between craters in different metals to be possible, the crater geometry and ablated volume with respect to the ratio F_0/F_{th} (where F_0 is the absorbed fluence and F_{th} the threshold fluence) was investigated. The absorbed fluence is $F_0 = F_L(1 - R)$, where R is the sample reflectivity at the laser wavelength. The laser fluence F_L was calculated as $F_L = 2P/fS$, where P is the average power, f the repetition rate and S the beam area

in the focus plane. To estimate the ablation threshold fluence of the thin films (which, depending on thickness, may vary from their bulk counterparts) the equation corresponding to ablation threshold was adapted from [115]:

$$F_{th} = (\Delta T_v + L_m/\rho c)\left[\left(\rho c_p - \frac{\delta'_{th}}{\delta_{th}}\rho'c'\right)d + \delta'_{th}\rho'c'\right],\qquad (4.1)$$

where ΔT_v is the variation between the evaporation and room temperature, L_m the melting enthalpy, ρ the density, c the specific heat at constant pressure, d the thin film thickness and $\delta_{th} = \sqrt{(\tau\,K/\rho c)}$ the thermal diffusion length (τ is the pulse duration and K the thermal conductivity). The material properties used to calculate the ablation threshold are given in Table 4.3. While common values were taken from literature, the thin film thickness and reflectivity were measured for Cu, Al and Ni respectively (0.60 µm, 0.56 µm and 0.87 µm thickness, 87%, 97% and 61% reflectivity at 1064 nm). The density used in the model was 90% of the bulk value, because of the voids which may be present in the thin film as a consequence of the deposition technique (as described in Section 2.3). For temperature-dependent properties, the values in the table correspond to room temperature. The estimated ablation thresholds were consistent with values reported in literature [30].

4.3 EXPERIMENTAL RESULTS

The variation in both crater geometry and ablated volume were plotted against the ratio between the absorbed fluence and the threshold fluence, as discussed in the previous section (Figure 4.1). This allowed for the evaluation of material response to laser ablation

while considering several material properties (which were used to calculate the ablation threshold).

Table 4.3 Material properties of Cu, Al Ni and Si and the calculated threshold fluence for single pulse laser ablation.

Property	Unit	Cu	Al	Ni	Si
(Measured) Thin film thickness	µm	0.60	0.56	0.87	-
(Measured) Reflectivity at 1064 nm	%	87	95	61	-
Density [149]	kg/m^3	8059	2436	8015	2330
Specific heat [149]	J/(kg K)	383	896	446	703
Boiling point [150]	K	2835	2791	3157	-
Latent heat of melting [151]	x 10^3 J/kg	203.48	396.98	297.82	1787.68
Thermal conductivity [152] [153] [127] [149]	W/(m K)	376.8	230	91	153
(Calculated) Threshold fluence	J/cm^2	1.77	1.57	1.78	-

Overall the depth and diameter of all samples were proportional to the fluence ratio, until a limit value was reached, where these values showed little variation. This is explained by maximum energy effectively used for material removal which is usually limited by the laser produced plasma; at higher densities, the plasma becomes opaque for the laser radiation and thus may act as a barrier shielding the workpiece [154]. In particular, craters in aluminium were deeper (~2.3 µm) even before reaching the plateau, followed by copper (~1.7 µm) and nickel (~0.9 µm). Even at lower fluences (below the estimated threshold), for aluminium and copper samples, the substrate was damaged; in

contrast, for the nickel sample, the craters seemed to "stop" at the film-substrate interface, the ablation causing minor damage to the substrate (melting) even at higher fluence ratios.
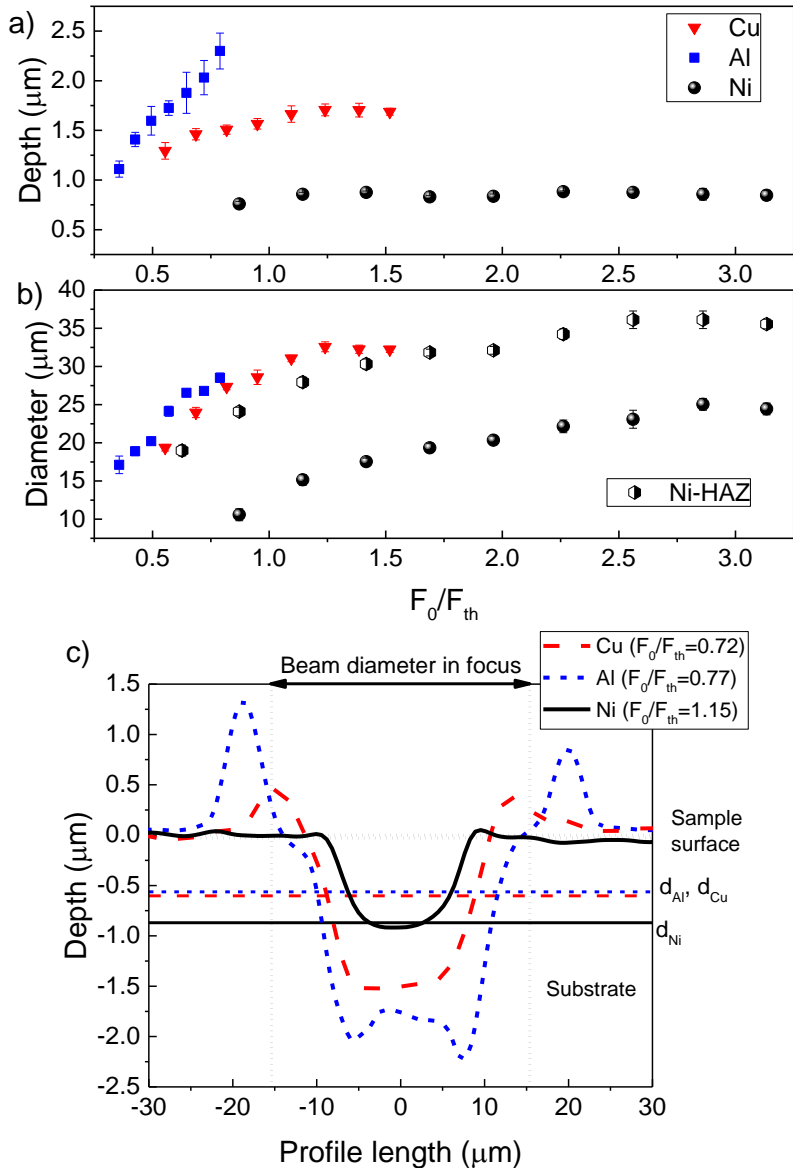
Figure 4.1 Crater depth (a) and diameter (b) versus fluence ratio. For the diameter of the nickel craters an extra set of values is shown, corresponding to the heat affected area. Typical crater profiles (c) are used to illustrate the differences in geometry. The beam diameter in focus and thin film thickness are indicated for reference.

In addition, the diameters of Cu and Al craters had similar trends, with values tending towards the beam size diameter in focus (30.75 µm). On the other hand, craters in the Ni

thin film were narrower (maximum 25 μm), but exhibited a non-ablated, HAZ with a diameter in the range of the beam spot size. Further, to assess the effects of thin film morphology, crater and as-deposited thin film cross sections are shown in Figure 4.2.
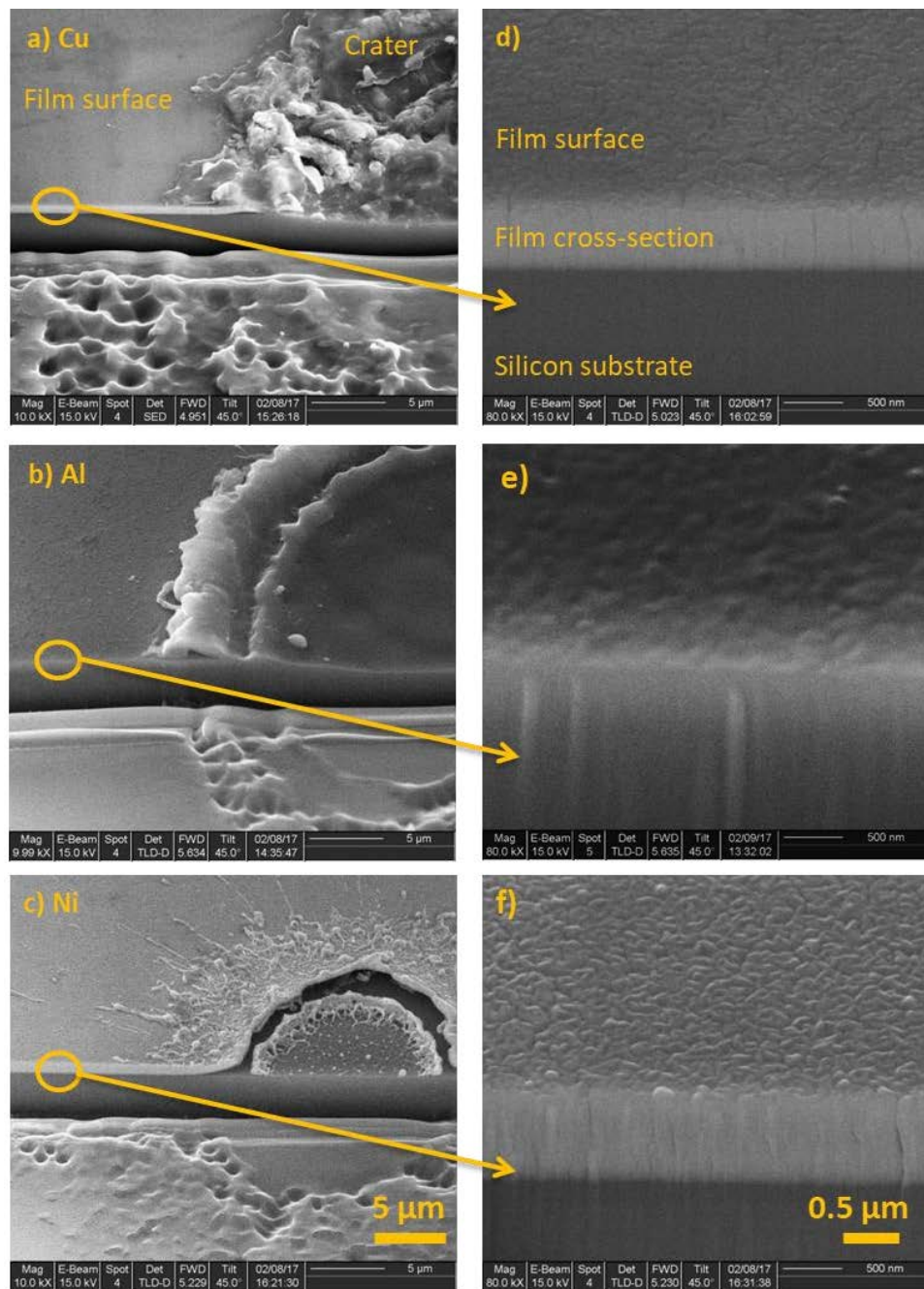
Figure 4.2 Micrographs of crater cross section (a-c) and as-deposited thin film (d-f) for Cu (top, a and d), Al (centre, b and e) and Ni (bottom, c and f) thin films. The craters were ablated with the same parameters as those shown in Figure 4.1c.

The crater cross sections (Figure 4.2a-c) revealed different heat affected areas for the three materials: for Cu and Al (Figure 4.2a,b) the crater edge consisted mainly of re-solidified material transported outside the irradiated zone by drag forces; in contrast, craters in Ni (Figure 4.2c) showed a wider irradiated area, with signs of melt but without significant ablation. The thin film cross sections (Figure 4.2d-f) revealed a columnar structure for the Ni thin film (Figure 4.2f), which became smoother for Cu (Figure 4.2d), while for Al (Figure 4.2e) the as-deposited thin film had a continuous, homogenous structure. The cross-section of nickel showed the film being removed from the substrate in areas adjacent to the irradiated zone. This aspect must be taken into account when considering the reliability of the volume measurements performed with an optical microscope: while the variation in the measured volume could be reliable, the actual ablated volume may differ slightly.

Finally, measured volumes are shown in Figure 4.3 (crater – a, melt – b and ablated – c). The crater volume (Figure 4.3a) is a direct result of crater geometry (depth and diameter, Figure 4.1a,b). Thus, the highest crater volumes were obtained in aluminium and copper (~600 μm^3), increasing steeply with the fluence ratio, while the crater volume in nickel showed a much slower rise and a lower volume (~300 μm^3) even at higher fluence ratios. The melt volume (Figure 4.3b) was lowest for nickel, meaning there was little to none re-solidified material at the crater edge (below 50 μm^3), followed by copper (150-250 μm^3) and aluminium (250-500 μm^3). By analysing crater depth (Figure 4.1a) and the crater micrographs (Figure 4.2a-c) the melt volume was found to be mostly re-solidified silicon from the crater bottom, resulting in more melt for the craters which reached deeper into the silicon substrate. The total amount of removed material (Figure 4.3c) showed a similar trend for copper and aluminium, with the negative values

explained by a smaller density of the re-solidified silicon (i.e. the density of specially prepared amorphous silicon is 1.8±0.1% less dense than crystalline silicone [155]). Since the nickel sample was ablated without significant substrate melting, the volume showed a steady increase, with only positive values.
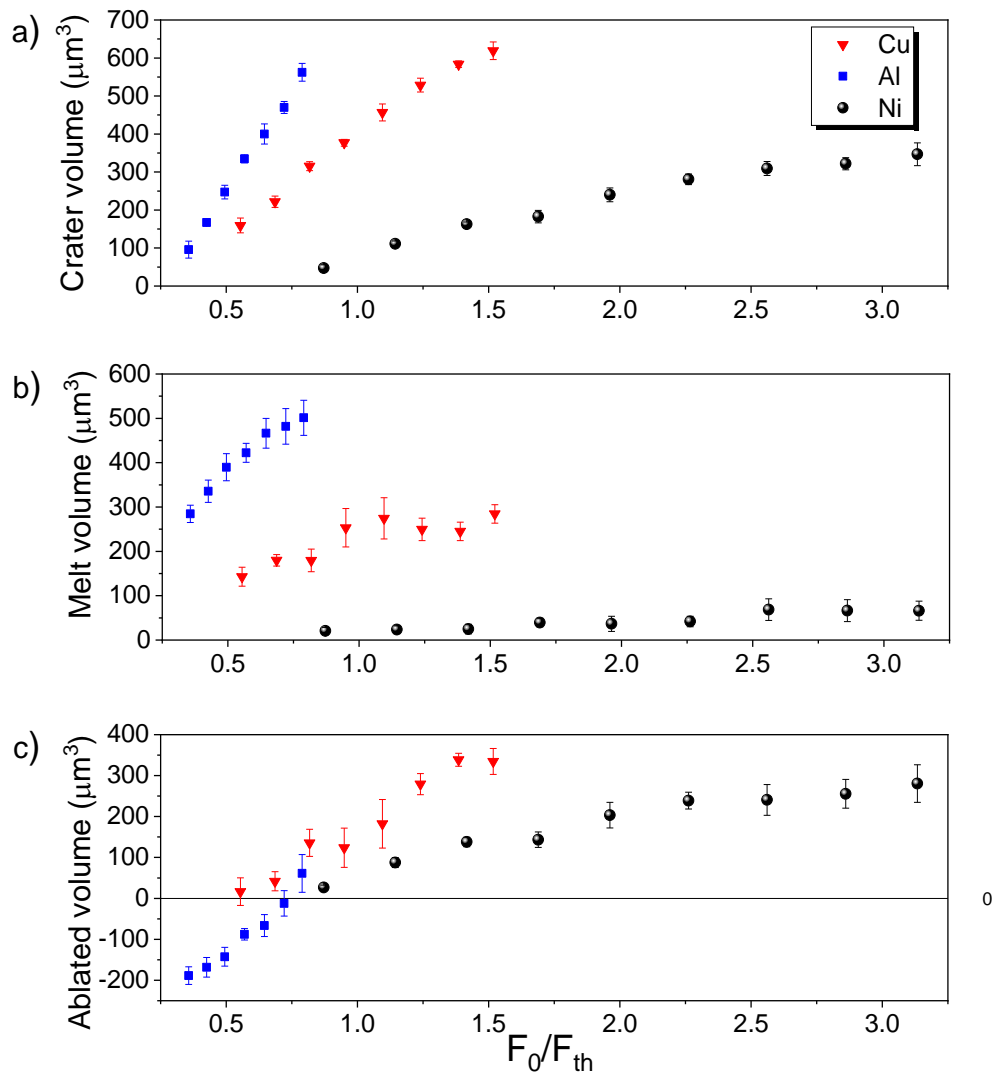
Figure 4.3 Crater (a), rim (b) and total ablated volume (c) versus the fluence ratio.

Overall, the results presented revealed similarities between craters in copper and aluminium which were different from craters in nickel in terms of morphology and geometry (and hence the amount of removed material). The difference in crater geometry

could be attributed to the combined effects of laser scattering at the surface, thermal diffusivity of the metals and the presence of the thermal barrier between the thin film and the substrate. A preferential lateral heat transfer for the Ni film compared to the more common vertical one in Cu and Al has been identified.

Wider craters in Al and Cu compared to Ni (Figure 4.1b,c) could be explained by the higher thermal diffusivity $k = K/\rho c$ of copper (k_{Cu}=100 µm²/s) and aluminium (k_{Al}=94 µm²/s) compared to the nickel sample (k_{Ni}=19 µm²/s). Craters in Al and Cu showed significant re-solidified substrate material on the edges, while Ni craters exhibited signs of melt without significant ablation and little to no redeposited material. The different nature of the heat affected zones could be explained by the thin film surface structure. The wider irradiated area in Ni craters may be due to scattering of laser light at the surface, which could have led to a change in the spatial energy distribution of the absorbed radiation [156]. The scattering would have had significant effects in the nickel sample due to its surface morphology shown in Figure 4.2f (i.e. particles smaller than the laser wavelength, in the range of 100 nm, measured using ImageJ), as opposed to the smoother surface of copper and aluminium thin films (shown in Figure 4.2d,e).

Deeper craters in Al and Cu samples (as shown in Figure 4.1a) and the ablation of the silicon substrate (Figure 4.1c) even at lower fluence ratios (F_0/F_{th}<1) could be attributed to the differences in thermal diffusivity discussed in the previous paragraph, resulting in a faster heat transfer and hence higher heat losses to the substrate. Crater depth was also influenced by the interfacial thermal resistance (i.e. how heat transfer took place from the thin film to the substrate and the partial reflection of the heat wave back into the metal), combined with more energy distributed to the lateral of the irradiated area for Ni, compared to Cu and Al. The interfacial thermal resistances for Al, Cu and Ni thin

films on silicon substrate (calculated for low temperatures, based on the acoustic mismatch model) are 11.8, 14.3 and 15.5 $K^4/(W/cm^2)$ respectively [128]. A smaller value would lead to a more facile heat flow towards the substrate and indicates that minimum heat losses to the silicon wafer were in the case of Ni. While these values for interfacial thermal resistance account for the nature of the materials (density and sound velocity), they do not consider scattering or reflection effects which can occur at the interface. A more structured thin film could mean a rougher interface, meaning lower heat transfer rates to the substrate and a higher amount of heat reflected, an effect observed previously regarding damage initiation on fused silica coated with absorbent films [157]. The effect of energy re-distribution by the surface structure and the wave reflection at the Ni-Si interface can be seen in Figure 4.2c which shows the Ni thin film detaching from the substrate in areas adjacent to the crater.

By comparing the geometry and amount of removed material in the three samples, it was concluded that the nickel thin film could be selectively ablated (without causing damage to the silicon substrate) by using 55 ns IR laser pulses. Extrapolating to other thin films, it would be possible to pattern a variety of materials without damaging the substrate (by using a typical Gaussian beam) by enhancing the thermal barrier between the thin film and the substrate during the deposition process. Potentially this could be achieved by adjusting the deposition parameters for changing the thin film morphology and thus the topography of the interface.

4.4 SUMMARY OF FINDINGS

In this chapter, pure metals were used to assess various aspects of crater geometry and morphology as a reference for the study of the binary and ternary composition

gradients. Similarities in terms of crater geometry and HAZ were identified for copper and aluminium thin films and optimal ablation results were obtained for the nickel thin film.

Three thin films (Cu ~ 0.60, Al ~ 0.55 µm and Ni ~ 0.90 µm) were irradiated with a similar set of laser parameters (1064 nm, 55 ns pulse duration, 15 kHz repetition rate and 30 µm Gaussian beam diameter in focus). Pulse average power was varied between 100% (1.5 W) and 55% (0.23 W) to investigate the material response (crater geometry, morphology and ablated volume) with respect to material properties.

The crater depth was generally largest in aluminium (2.3 µm), followed by copper (1.7 µm), showing significant removal of the silicon substrate, even at lower fluence ratios, and typical crater profiles were Gaussian shaped. In contrast, the nickel sample showed a "cleaner" ablation, with minimal damage to the substrate, having an overall depth around 0.9 µm. The craters seemed to stop at the thin film-substrate interface, with more square-shaped crater bottom. Crater cross sections revealed peeling of the Ni thin film in the area adjacent to the crater, indicating a stronger lateral heat flow than in the other two samples, which seemed to undergo the typical vertical one. Crater diameters were similar in copper and aluminium, with values tending towards the beam diameter in focus as the fluence ratio increased. The nickel craters had a smaller diameter (maximum value ~25 µm), and a noticeable HAZ with dimensions up to 35 µm. The existence of the HAZ was attributed to the redistribution of laser energy at the sample surface, a possible result of scattering of the beam by the sub-wavelength surface structures.

Cross sections of the as-deposited thin film revealed a columnar structure in the Ni sample, which was less pronounced in Cu, and not observable in the Al thin film. The thin film structure is likely to have increased the magnitude of the thermal barrier at the

thin film-substrate interface, by decreasing the contact area. Thus, the reflection of the heat wave at the interface would have been strongest for Ni, resulting in the specific crater shape.

When analysing the amount of removed material, the direct influence of crater depth and diameter on the volume below the surface was observed. The total amount of removed material was also influenced by the volume of the re-solidified melt (above the surface). A correlation between the amount of material above the thin film surface and crater depth has been noticed, suggesting that the molten volume is mostly recast silicon.

Overall, a cleaner removal of the nickel thin film has been observed, suggesting that it is possible to achieve thin film patterning using a typical ns IR laser with a Gaussian beam by altering the deposition process in such a way as to increase the thermal barrier between the thin film and the substrate.

5 LASER ABLATION OF BINARY ALLOYS

After the investigation of pure Cu, Al and Ni films in the previous chapter, the following work studies the response of binary material libraries when irradiated with a laser beam of constant parameters. Binary combinations of Cu, Al and Ni were studied, and each was used to highlight certain aspects of laser ablation on thin film material libraries, as follows. First, the binary Cu-Ni solid solution was investigated to understand how changes in chemical composition affect the material response to irradiation in the absence of well-defined film microstructure. Further, by irradiating a binary Ni-Al film with constant laser parameters, the variation in crater morphology and geometry was investigated when both the composition and thin film morphology varied. This section also analyses how a sudden change in film microstructure affected the crater characteristics. The last section on Cu-Al discusses variations in the ablated craters with the chemical composition, when the thin film showed both well-defined surface and cross-sectional morphology all over the compositional range.

5.1 EXPERIMENTAL DETAILS

The deposition parameters for the binary films are given in Table 5.1. The resulting thickness had small variations across the compositional spread because of the synthesis method. The overall thickness was 0.78 µm ± 10% for Cu-Ni, 1.34 µm ± 18% for Ni-Al and 1.51 µm ± 21% for Cu-Al films.

Imaging of thin film cross sections has been achieved by cleaving the sample in the vicinity of the laser pattern and tilting of the specimen in the SEM chamber by 45°. Imaging of the cleaved areas was preferred to FIB milling as it was less time consuming

and thus allowed for a greater number of experiments to be carried out in a reasonable amount of time. The micrographs were then used to analyse the variation of cross-sectional microstructure with the chemical composition to gain a better understanding of its contribution to crater morphology.

Table 5.1 Specific process parameters used in the deposition of the binary thin film libraries.

	Cu-Ni	Ni-Al	Cu-Al
Base pressure (mbar)	$2x10^{-7}$	$1x10^{-6}$	$2x10^{-7}$
Gas used	Ar		
Flow rate (sccm)	45	15	15
Sputtering pressure (mbar)	3x10-3	5x10-3	5x10-3
Deposition time (min)	210	300	240
Sputtering power (W)	Cu: 26.1 (DC) Ni: 150 (RF)	Al: 46.4 (DC) Ni: 150 (RF)	Cu: 40.5 (DC) Al: 82.8 (DC)
Substrate temperature	Room temperature		
Substrate	Si (100)		

As described in Section 3.2.2, nine areas of constant chemical composition (covering the whole compositional spread) were ablated using the same laser parameters as for the pure samples (1064 nm wavelength, 55 ns pulse duration and 15 kHz repetition rate); the average power per pulse for all the lines are given below (Table 5.2).

*Table 5.2 Average pulse power for the ten crater lines used to process the binary material
libraries (identical with the parameters used for the pure films).*

%	55	60	65	70	75	80	85	90	95	100
Average power (W)	0.23	0.32	0.42	0.52	0.62	0.72	0.83	0.94	1.05	1.15

To understand the variation of material properties (e.g. reflectivity) and ablation result with respect to the chemical composition, aluminium atomic percentage was chosen as the *x* axis for the Al alloys (Ni-Al and Cu-Al). The choice was based on the relation between the melting point of the material and the thin films' surface and sub-surface microstructure, as shown by Thornton [158]. The melting point of aluminium is lower than copper or nickel, so it is likely to have the most influence on the thin film structure and its thermal properties.

5.2 LASER ABLATION OF THE COPPER-NICKEL SOLID SOLUTION

The aim of this section is to study the laser ablation of a compositional spread for a thin film with a smooth surface and in the absence of well-defined microstructure. The binary Cu-Ni material library represents a good starting point in analysing the material response to laser ablation for a target with varying chemical composition. This is due to the similarity between Cu and Ni in terms of density and melting points compared to Al, as well as the two metals' complete miscibility, which allowed for a simple estimation of thermal properties based on the rule of mixtures [159]. The ablation results were thus plotted against the ratio between the absorbed fluence and the threshold fluence, similar to the results on the pure metals (Chapter 4). Thermal properties and density were calculated as shown in Equation (5.1), where ρ is the density, X can be specific heat,

enthalpy of fusion or thermal conductivity and m is the weight percentage of the element in the alloy. The melting temperature as a function of chemical composition was taken from the binary Cu-Ni phase diagram.

$$\frac{100}{\rho_{alloy}} = \left(\frac{m_{Cu}}{\rho_{Cu}} + \frac{m_{Ni}}{\rho_{Ni}}\right)$$

$$X_{alloy} = m_{Cu}X_{Cu} + m_{Ni}X_{Ni}$$

(5.1)

Two areas of different chemical composition were chosen for analysis: a copper rich area (23% Ni at. %) and a nickel rich area (65% Ni at. %). The measured reflectivity at 1064 nm was 0.84 for both areas. The value was higher than reflectivity of Ni and lower than reflectivity of Cu ($R_{Ni} = 0.73$, $R_{Cu} = 0.92$ [75]), which indicated no influence of the surface on the reflectivity. Material properties used to estimate the ablation threshold are given in Table 5.3. The boiling point for both areas was taken as the one of Ni (highest of the two metals), on account of the lack of data in literature or details on the calculation method.

Crater geometry and volume are shown in Figure 5.1. Despite the difference in chemical composition, the two areas exhibit very similar response to irradiation with the same laser parameters, as shown below. The crater diameter (Figure 5.1a top) was slightly higher for the Cu rich area and this resulted in minor differences in the crater volume (Figure 5.1b top). Crater depth (Figure 5.1a bottom), melt volume and ablated volume are practically identical with variations occurring only at a laser fluence below the ablation threshold (i.e. $F_0/F_{th} < 1$). Irrespective of the fluence ratio, the silicon substrate was ablated,

indicating a strong vertical heat flow. Re-solidified silicon on the crater edge resulted in increased melt volume and smaller (even negative) amount of removed material.

Table 5.3 Material properties for the Cu-rich and Ni-rich areas and the estimated threshold fluence for 55 ns single pulse laser ablation.

Property	Unit	Cu-rich area	Ni-rich area
(Measured) Thin film thickness	x 10^{-9} m	0.75	0.80
(Measured) Reflectivity at 1064 nm	%	84	84
Melting point	K	1482	1630
Boiling point	K	3003	
Density	kg/m^3	8949	8927
Specific heat	J/(kg K)	397	423
Latent heat of melting	x 10^3 J/kg	224	263
Thermal conductivity	W/(m K)	314	196
Thermal diffusion length	x 10^{-6} m	3.29	2.52
Threshold fluence	J/cm^2	1.94	1.89

Crater profiles in both areas are shown in Figure 5.2a. At the lowest absorbed fluence the irradiated area was swollen, probably due to the change in density caused by the re-solidification of molten material. At higher fluence all crater profiles had a typical shape similar to the spatial energy distribution beam (Gaussian) – similar to the craters in the pure Cu film (Chapter 4). This typical shape indicated a heat transfer normal to the sample surface. Micrographs of the as-deposited thin film (Figure 5.2b) are shown to support this idea, as they revealed a smooth surface and a compact (dense) thin film. The absence of well-defined grains indicated a lower interface roughness and, thus, a lower contribution of film morphology to the magnitude of the thermal barrier between the binary film and the silicon substrate.
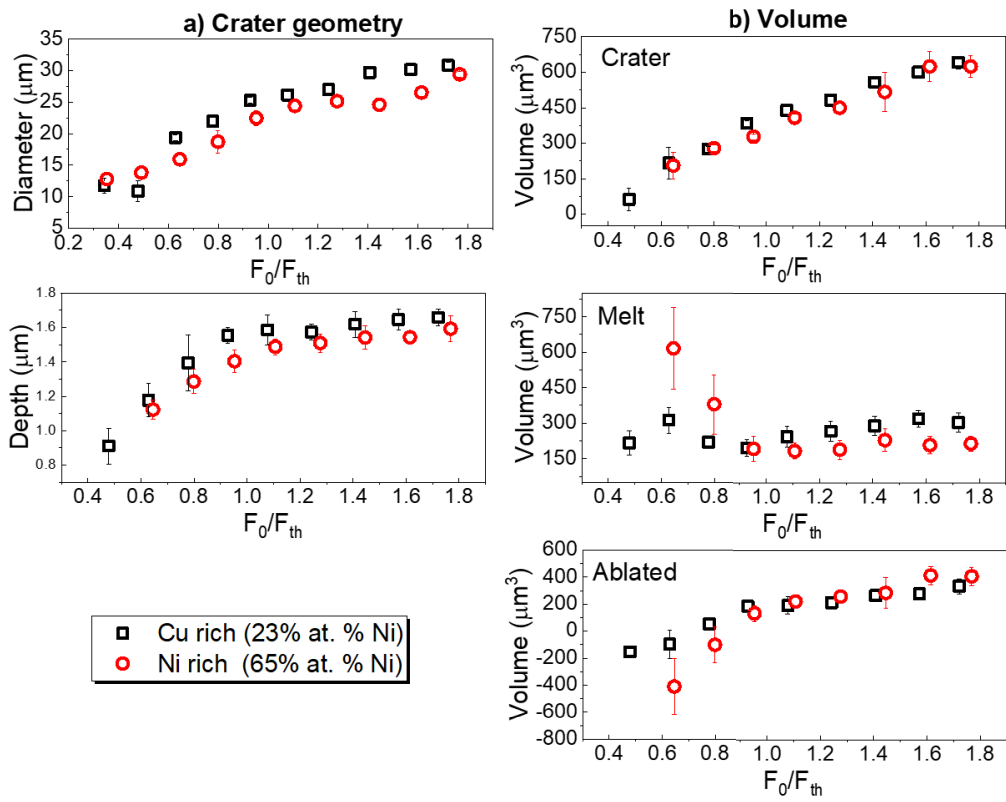
Figure 5.1 Crater geometry (a) and measured volumes (b) versus the fluence ratio for two areas of constant chemical composition.
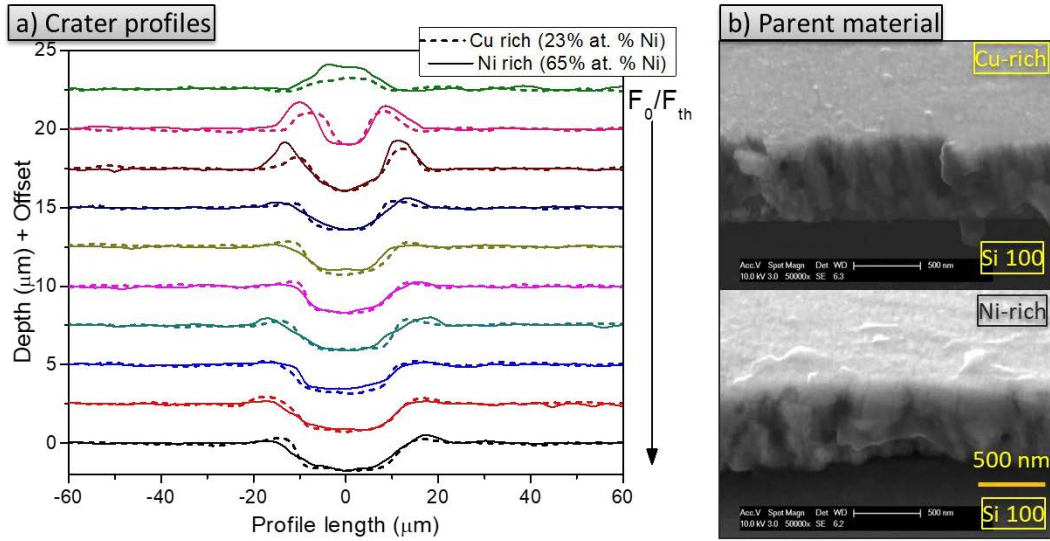
Figure 5.2 Typical crater profiles (a) and as-deposited thin film cross-sections (b) for two areas of constant chemical composition.

5.3 Laser ablation of nickel-aluminium thin film material library

The aim of this section is to study the material response to irradiation when the variation in chemical composition is accompanied by significant changes in film microstructure. To understand the laser ablation results of the more complex nickel-aluminium (this section) and copper-aluminium systems (Section 0) it was necessary to characterise not only the films' chemical composition, but also the associated variations in film microstructure and reflectivity. The compositional range covered by the aluminium-nickel sample is shown superimposed on a binary diagram for the Ni-Al system in Figure 5.3. Films deposited via sputtering often form metastable and non-equilibrium phases which are not represented in a phase diagram generated by slow cooling, so it is quite possible that the phases present within the sputtered film differ from those shown here.

Thin film reflectivity across the compositional spread is shown in Figure 5.4 as a function of the aluminium at. %. Considering the typical higher reflectivity of Al and Ni at 1064 nm (0.80 Al [76], 0.73 Ni [75]), the sample overall reflectivity was generally lower than the values reported for polished surfaces. This variation in reflectivity could be partially explained by the lower reflectivity of Ni compared to Al, which would result in an overall decrease in reflectivity. In addition, optical properties of the material are also influenced by surface microstructure and topography which would affect the measured reflectivity (specular – measured by FTIR) by light scattering at the surface (diffuse). Surface micrographs are shown in Figure 5.4 to illustrate the evolution of surface morphology and its correlation to sample reflectivity.
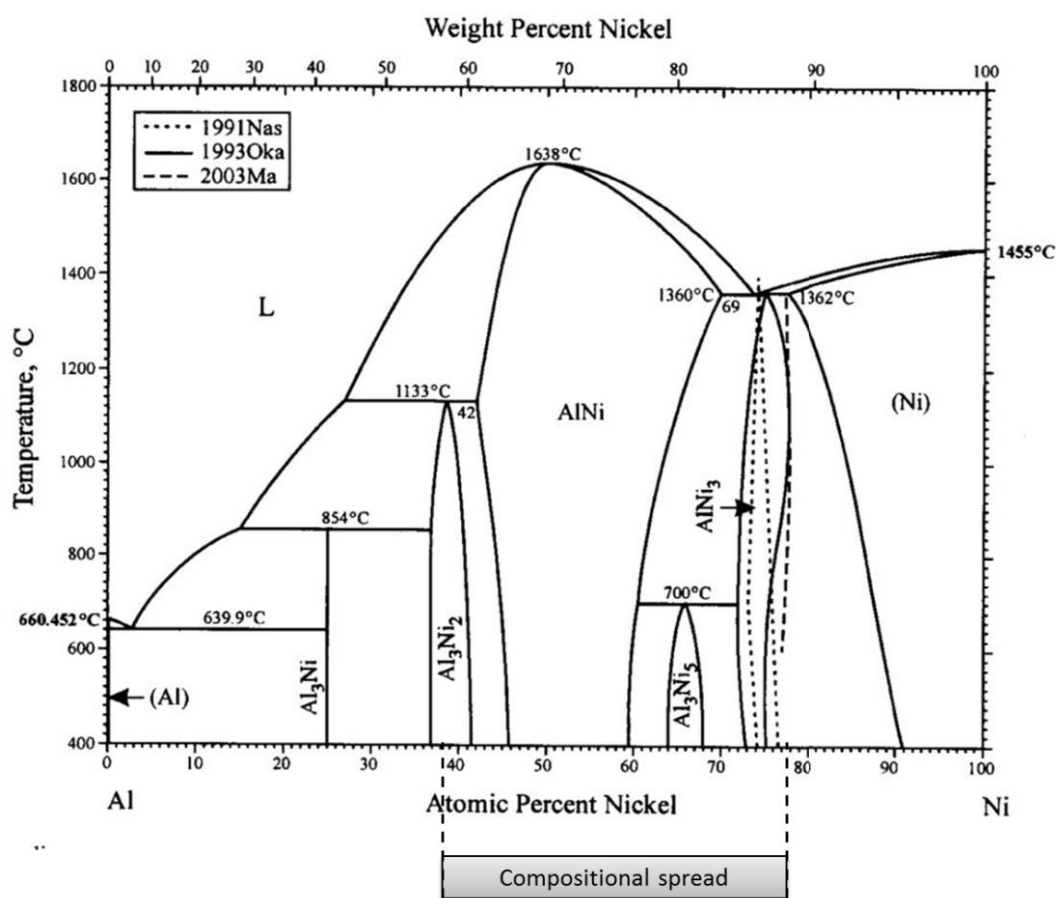
Figure 5.3 Binary Ni-Al phase diagram, adapted from [160] showing the region covered by this compositional gradient sample (Ni at. %: 38.79 – 77.92, Al at. %: 61.21 – 22.08).
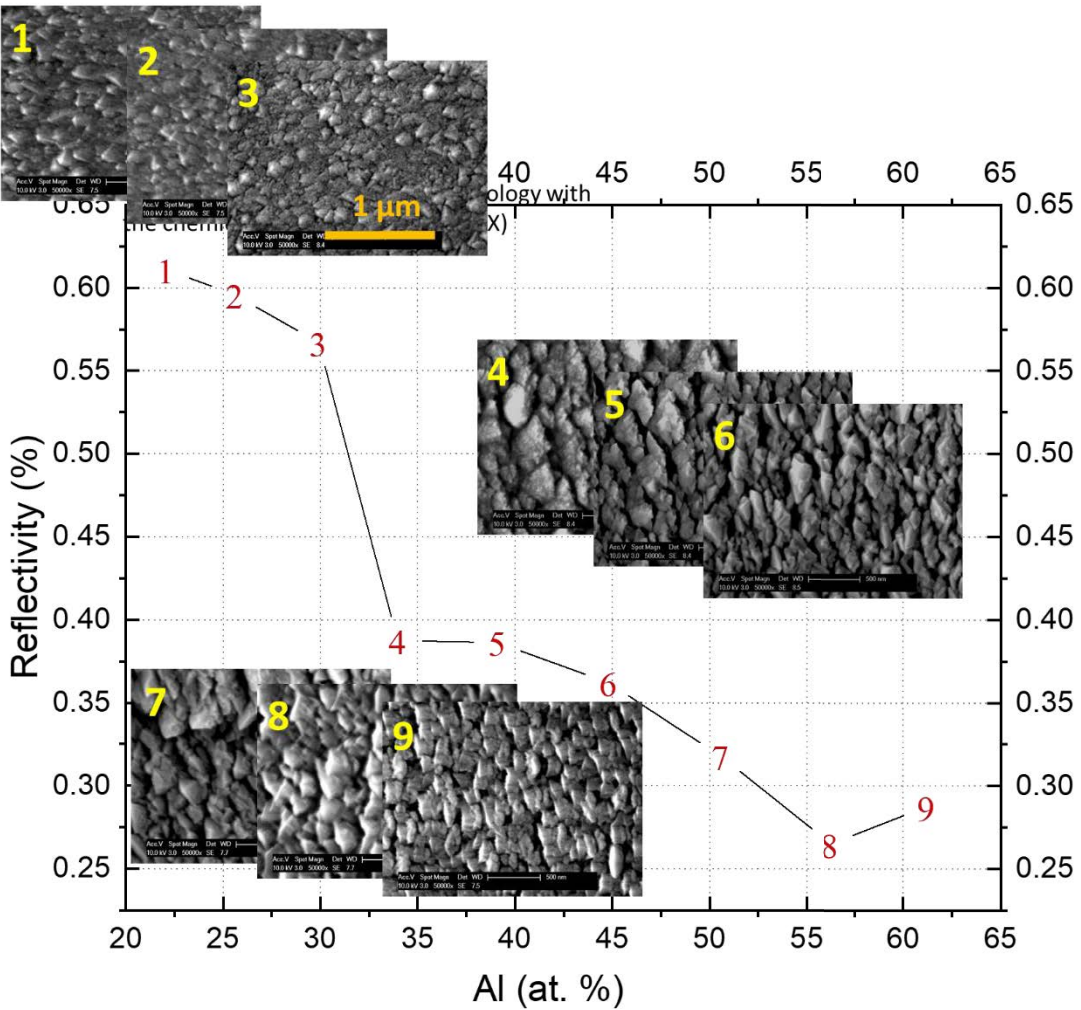
Figure 5.4 Reflectivity of the binary Ni-Al film as a function of Al at. %. Thin film morphology of the corresponding areas is shown to underline the correlation between reflectivity and surface morphology. Numbers are used instead of symbols to facilitate the identification of the corresponding surface morphology.

A sudden drop in reflectivity was observed above 30 at. % Al (*transition* area, between *zones 3* and *4*), and seemed to be correlated with the change in surface morphology. Thus, thin film micrographs in the transition area are shown in Figure 5.5 to understand the evolution of grain formation. The addition of Al encouraged the formation of surface structures with the appearance of particle clusters, which eventually formed a well-defined microstructure.
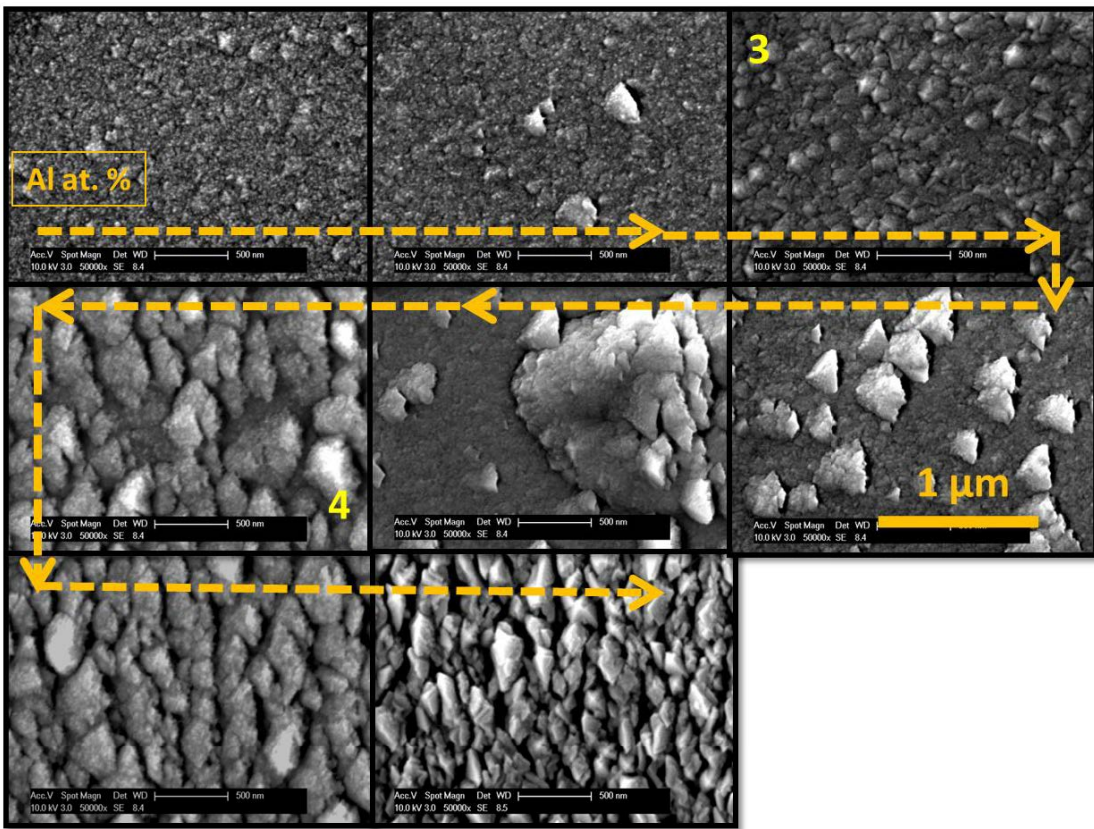
Figure 5.5 Micrographs of the transition area illustrating grain formation with the addition of aluminium (the direction is indicated by the arrows). Zones 3 and 4 from Figure 5.4 are indicated.

Following as-deposited thin film (i.e. the sample before irradiation) characterisation, the first step in crater analysis was to study areas of extreme chemical composition (*Zone 1* – 22 Al at. %, *Zone 9* – 61 Al at. %) and the centre of the composition range (*Zone 5* – 39 Al at. %), irradiated with similar laser parameters and different average pulse power, as shown in Table 5.2. Typical crater profiles for the studied areas corresponding to all average powers are shown in Figure 5.6. Craters in *zone 1* are widest, with diameter approaching the beam diameter in focus as the fluence increases, while craters in *zone 5* and *zone 9* are narrower, with a significant amount of re-deposited material on the edges. Well defined craters were found in *zones 1* and *5*, while in *zone 9*

below 14.9 J/cm^2 the irradiated area was swollen. Based on these observations, craters ablated with 18.9 J/cm^2 (where typical crater shape is clearly observed for all three zones) were chosen for further analysis of crater geometry and morphology as a function of chemical composition.
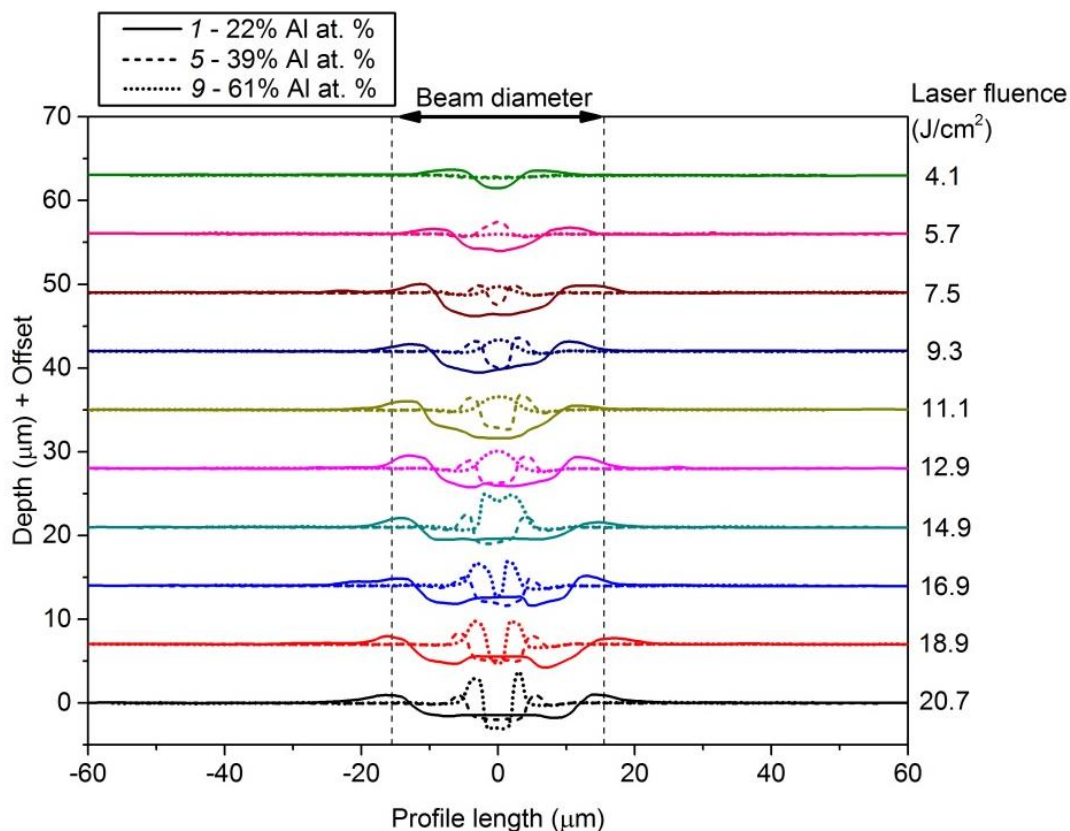
Figure 5.6 Typical crater profiles for three areas of constant chemical composition: Zone 1 – 22 Al at. % (continuous line), Zone 5 – 39 Al at. % (dashed line) and Zone 9 – 61 Al at. % (dotted line). Laser fluence is indicated on the right-hand side.

Crater geometry and absorbed fluence (with respect to Al at. %) are shown in Figure 5.7. As strong variations in the reflectivity were recorded along the compositional gradient, the absorbed fluence (after reflection of radiation) $F_0 = F_L(1 - R)$ is given as a reference. Crater diameter (Figure 5.7a) generally decreased with increasing aluminium percentage, despite the increase in the absorbed fluence.
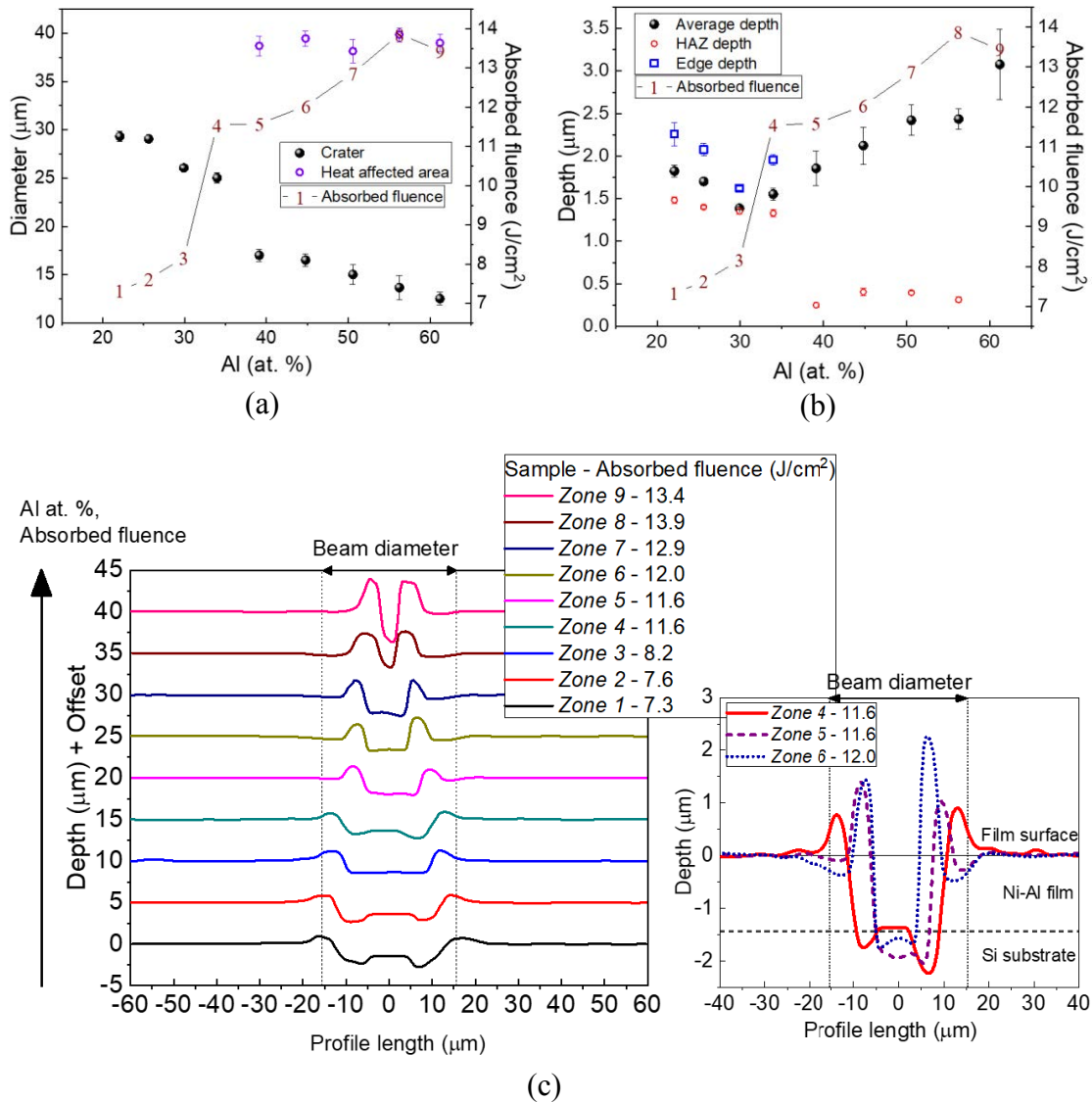
Figure 5.7 Crater geometries for the Ni-Al film obtained at a laser fluence of F_L =18.9 J/cm². Diameter (a) shows the diameter of the crater and heat affected area (HAZ). Depth (b) shows the average crater depth (marked as average depth), as well as depth of the HAZ, marked as HAZ depth and the depth of the crater bottom extending to the substrate on the outer edge, marked as edge depth. Typical crater profiles for the Ni-Al compositional spread (c). The legend indicates the zones of constant chemical composition and the absorbed fluence. The beam diameter in focus is given as reference (c- left). Typical crater profiles for the transition identified based on the crater shape: zones 4-6 are shown and beam diameter in focus and film thickness are marked (c-right).

A drop in the measured diameter and the apparition of the HAZ marked a transition in material response to irradiation between *zone 4* and *zone 5*. While crater diameters decreased the diameter of the HAZ remained relatively constant. Crater depth (Figure 5.7b) revealed a wider transition area, between *zones 3* and *5*. Crater depth decreased with the addition of Al in *zones 1-3*, followed by a linear increase in *zones 4-9*. Craters up to zone *4* have a flat bottom (i.e. depth was around the film thickness) with edges extending deeper into the silicon substrate (Figure 5.7c). Craters in *zones 5-9* had a shallow ablated area outside the re-solidified material, and the Si substrate was generally ablated.

Further, to understand the material response to irradiation based on these geometrical observations, cross sections of the as-deposited thin film (prior to ablation) together with crater morphology are shown in Figure 5.8 to Figure 5.10.
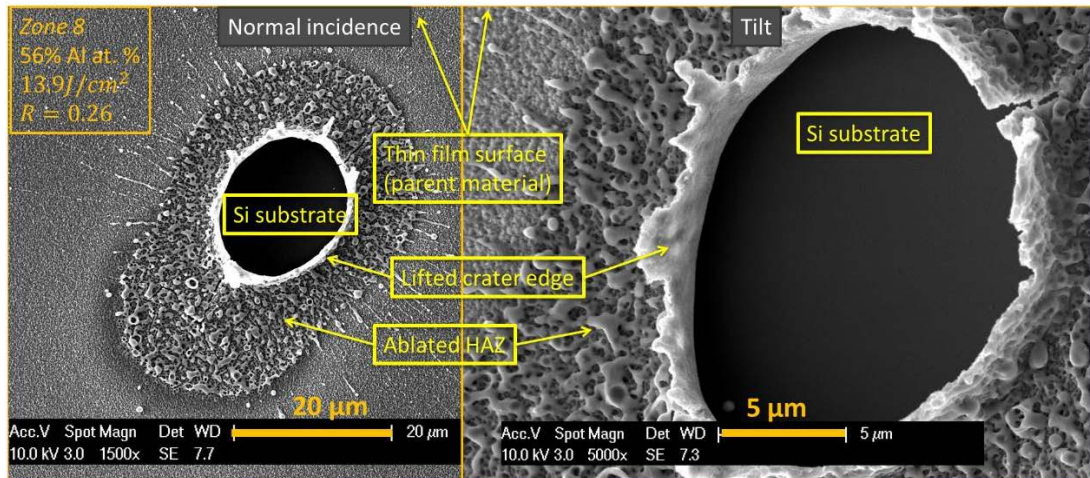
Figure 5.8 Typical crater in Zone 8, normal incidence view (left) and tilted view (right). Chemical composition, absorbed fluence and reflectivity are indicated on the top left of the image. Various crater elements are identified.

In Figure 5.8 a typical crater from *zone 8* is shown in both top and tilted views, to identify various crater elements and to understand how 3D features appear in a normal

angle incidence micrograph. This facilitates analysis of crater morphology and is significantly less time consuming than FIB cross-sectioning. The craters showed a smooth bottom, where the silicon substrate was clearly visible. The film on the crater edge was molten and lifted from the substrate. The HAZ showed signs of melt and ablation, with cracks appearing due to cooling-induced stress. The as-deposited thin film surrounding the material exhibits few signs of damage, i.e. splashes as the material was expulsed from the centre of the irradiated area. A magnification which allowed for complete crater observation did not allow for detailed observation of the as-deposited thin film, so in Figure 5.9 and Figure 5.10 cross-sectional micrographs are shown.

The craters in *zones 1-3* (Figure 5.9a) showed significant amount of re-solidified material on the edges, and with the increase in Al, the crater edge was increasingly lifted from the substrate. This behaviour was attributed to the micro-structured thin film, which could increase the magnitude of the thermal barrier between the thin film and the substrate compared to a less structured material. A stronger thermal barrier enabled more heat to be reflected into the film, resulting in the observed edge lift due to lateral heat transfer. Usually discontinuities in the film (i.e. boundaries between structures) act like thermal barriers, so it would be expected that the presence of well-defined vertical grains would impede to some extent lateral heat transfer. However, this effect was not noticed, probably because the reflection of the heat wave at the thin film-substrate interface was the dominating process in heat distribution. The transition area previously identified in crater geometry (*zones 4 and 5*) is shown in Figure 5.9b. Crater edge detached from the substrate, showing that lateral heat transfer was dominant. The HAZ in *zone 4* showed signs of molten material. In *zone 5* a different HAZ was observed, with signs of material removal (by melt and evaporation). The lateral spread of the affected area (even beyond

the laser beam size in focus) was potentially a consequence of beam deformation when interacting with the surface structures

(a)

(b)
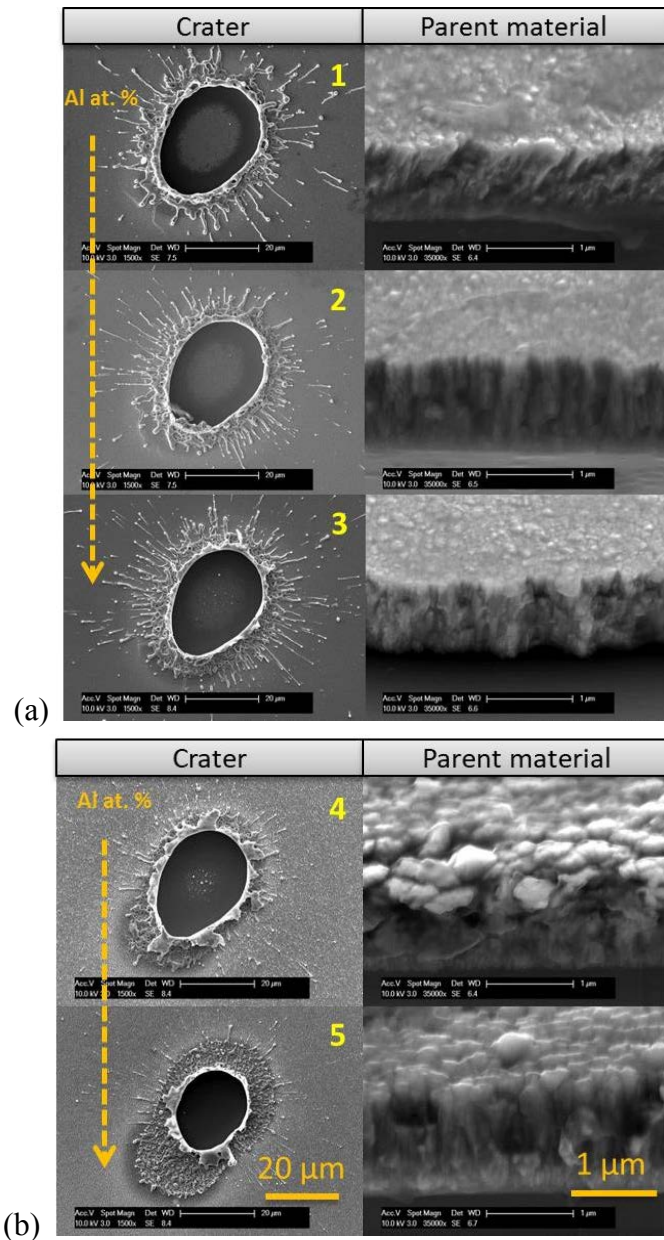
Figure 5.9 Typical craters (left) and parent micrographs (right) for zones 1-3 (a) and zones 4-5 (b).
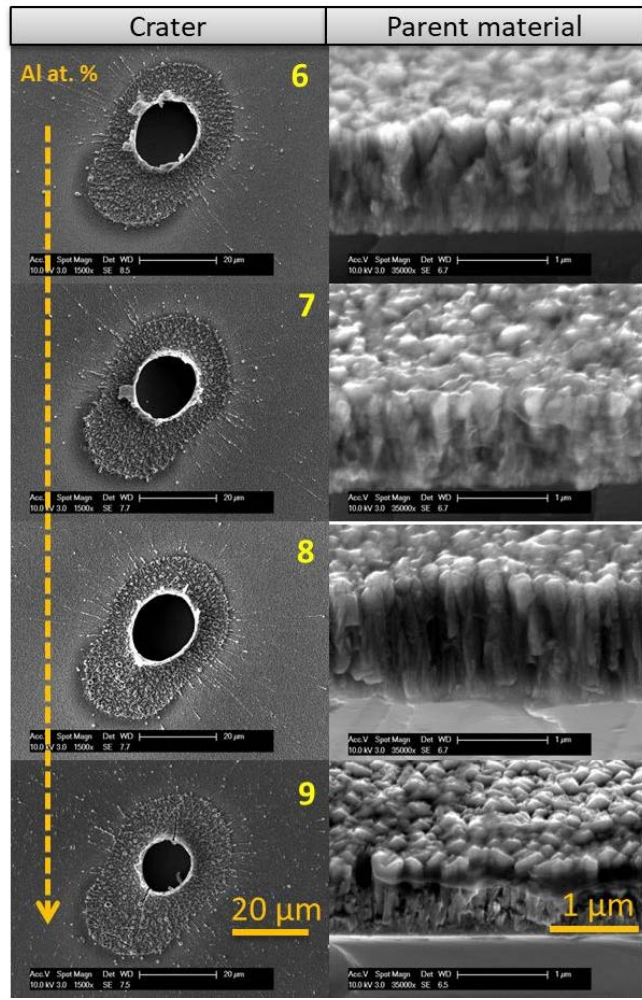
Figure 5.10 Typical craters (left) and parent micrographs (right) for zones 6-9.

The change of energy beam distribution at sample surface could be responsible for the decrease in crater diameter observed in *zone 5* and further in *zones 6-9* (Figure 5.10), as more energy was delivered to the sides, less energy was available in the centre of the beam for complete film removal. The craters exhibit similar heat affected areas, as shown in Figure 5.7a. Crater profiles and depth measurement for *zones 6-9* reveal that crater depth and diameter were inverse proportional. This behaviour was attributed to both an increase in the absorbed fluence and to a decrease in the threshold fluence with the

addition of aluminium, up to a point where the strength of the thermal barrier was not enough to stop thermal damage and subsequent ablation of the substrate.

5.4 LASER ABLATION OF COPPER-ALUMINIUM MATERIAL LIBRARY

The aim of this section is to study the laser ablation of a compositional spread for a micro-structured thin film. Like Ni-Al, the Cu-Al sample was first characterised in terms of chemical composition, reflectivity at the laser wavelength and morphology. The material library used in this study ranged from 29.5% to 71.2% Al at. % (70.5% to 28.8% Cu at. %) and potentially covered a variety of phases as shown in Figure 5.11.
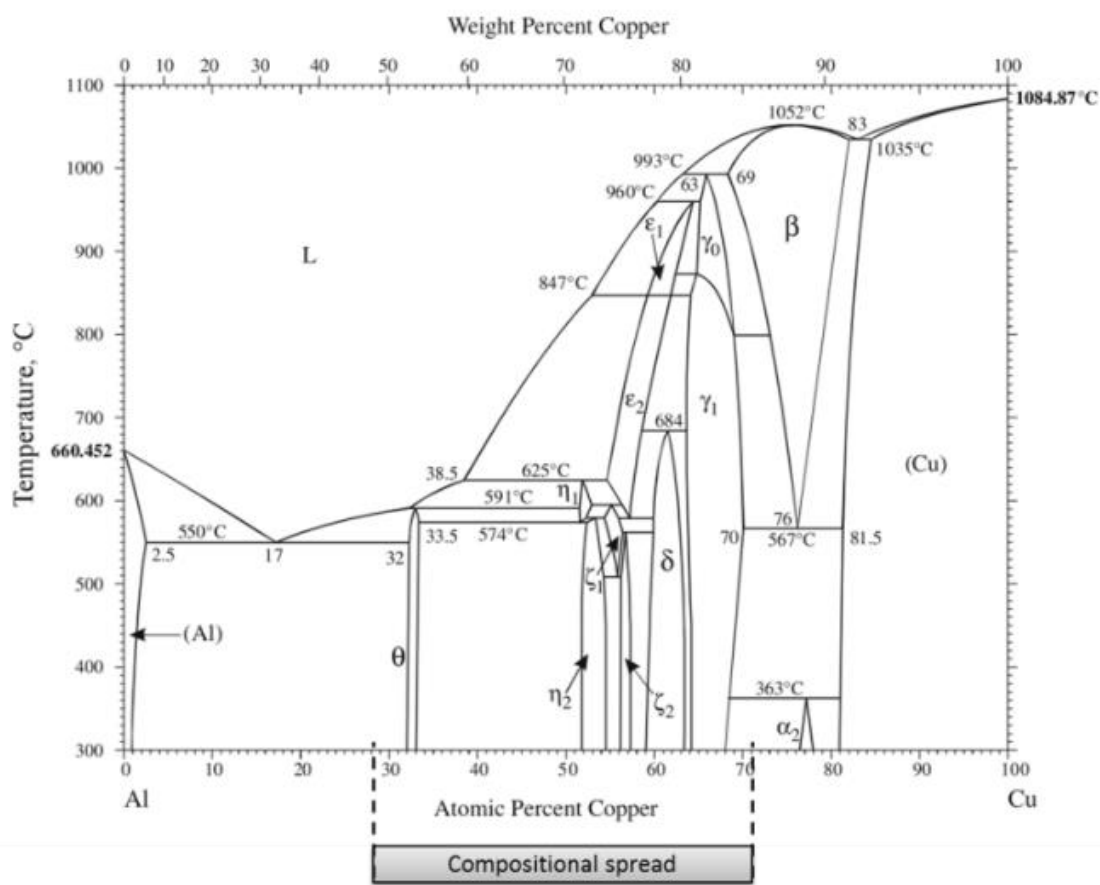
Figure 5.11 Copper-aluminium binary system phase diagram (adapted from [161]) indicating the composition range covered by the thin film.

The reflectivity of the sample at 1064 nm and the surface morphology of the thin film prior to irradiation are shown in Figure 5.12 as a function of Al at.%. As opposed to the binary Ni-Al sample (where a decrease in reflectivity with the addition of aluminium was observed), the binary Cu-Al sample showed an overall increase of reflectivity with the Al at. %. This difference could be a consequence of the different microstructures in the two binary films.

Two distinct types of well-defined surface morphologies were identified in the case of Cu-Al material library. At lower aluminium percentages (below 55%) the surface structures were larger (up to 500 nm) with a 2D shape, like knife edges (*zones 1-4*). Above 55% Al at. % the surface consisted of diamond-like particles, smaller (~100 nm) and more compact (*zones 6-9*). While not within the aim of the present work, a notable feature of surface morphology was identified, regarding the dominant direction of the structures' growth changing from vertical (in *zone 1*) to horizontal (in *zone 4*). This was a potential result of different intermetallic phases formed in the film. Moreover, sputtered films commonly exhibit a fibre texture, but it is also possible to have a mosaic epitaxy in which the crystal lattice is aligned along multiple axes. Considering the sputtering technique used (where copper and aluminium were co-sputtered) the flux coming from the different targets varies along the substrate position, which could also contribute to the surface morphology.
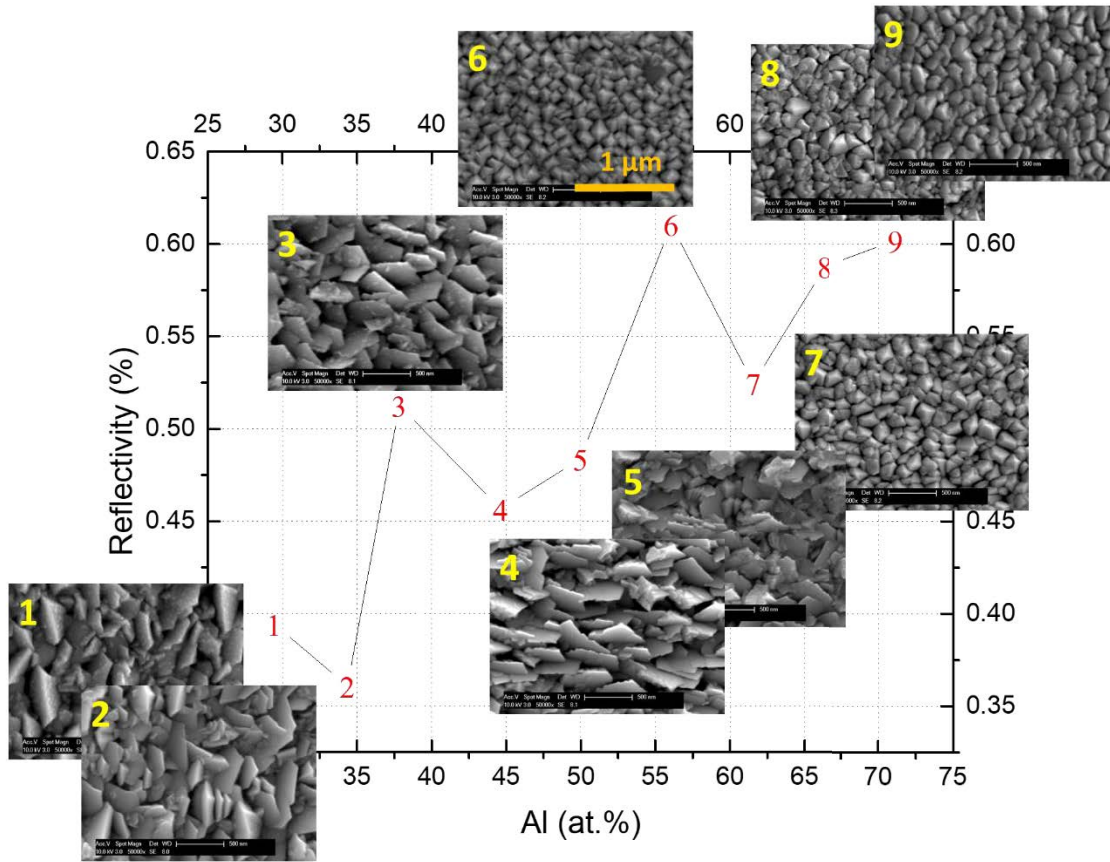
Figure 5.12 Reflectivity of the binary Cu-Al film as a function of Al at. %. Thin film surface morphology of the corresponding areas is shown to underline the correlation between reflectivity and surface morphology.

Cross sections of the as-deposited thin film are shown in Figure 5.13 to assess the zones with similar structures. Areas with similar surface and cross-sectional morphology are *zones 1-4* where the structures are pyramidal/conical but become more compact with the increase in Al at. %, and *zones 7-9* with densely packed, vertical structures having a more cylindrical shape. Based on these observations, the craters in *zones 7-9* are further analysed as they showed the least variation in surface and cross-sectional morphology.
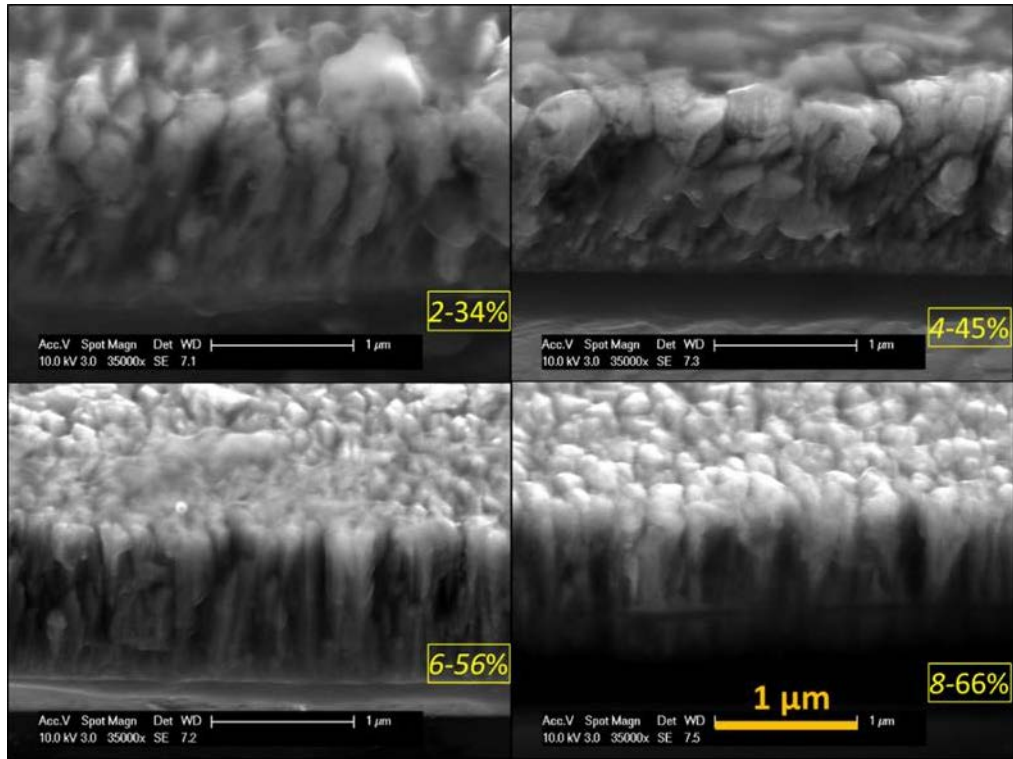
Figure 5.13 Typical cross-sections of the Cu-Al film. The zone and aluminium atomic percentage are indicated on each image.

The film's response to irradiation was first evaluated by investigating crater profiles obtained by using ten different average powers on three areas with different chemical composition (29%, 50% and 71% Al. at. %, *zones 1, 5* and *9*) are shown in Figure 5.14. At lower fluences the irradiated area was swollen (in *zone 1 – 29% Al at. %*) and craters were Gaussian shaped (*zones 5 and 9,* 50% and 71% Al at. % respectively). This confirmed that indeed, the ablation threshold was proportional to the aluminium content in the film. As the fluence increased, the crater bottom became flatter, suggesting a strong thermal barrier between the film and the substrate. All craters had a well-defined shape with the main difference between various fluences being the crater diameter. Since the craters irradiated with a fluence of 18.9 J/cm^2 had a diameter close to the beam size

in focus without excess energy being deposited in the sample (i.e. at higher fluence), these were chosen for further analysis.
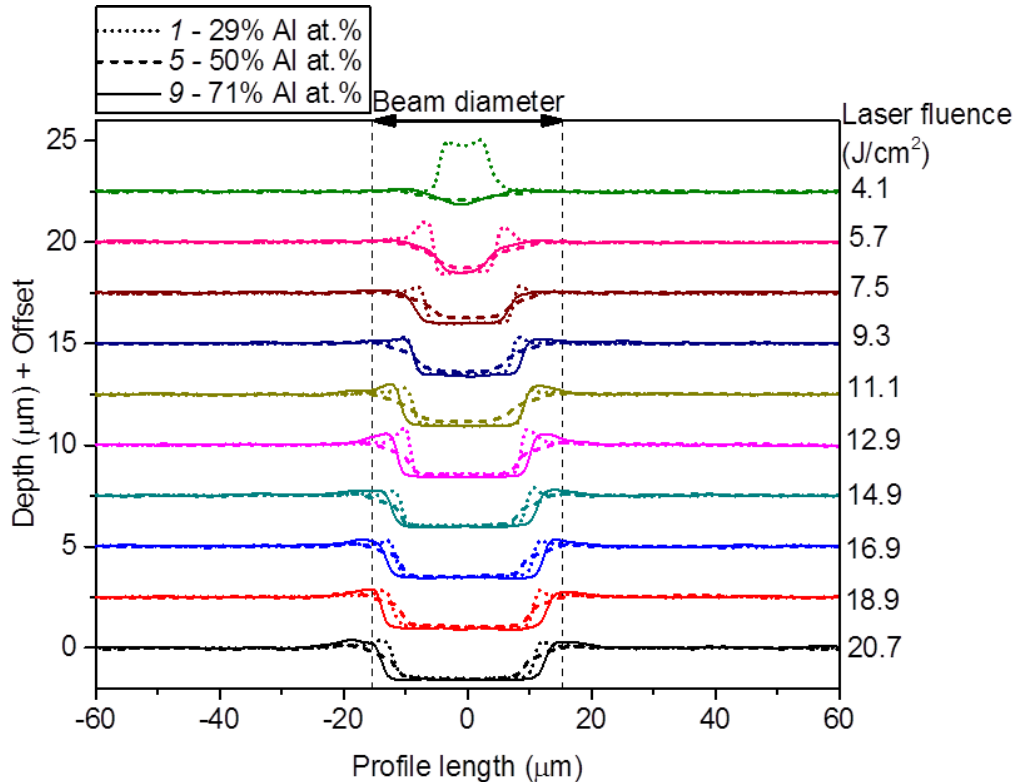
Figure 5.14 Typical crater profiles for three areas of constant chemical composition: Zone 1 – 29 Al at. % (dotted line), Zone 5 – 50 Al at. % (dashed line) and Zone 9 – 61 Al at. % (continuous line). Laser fluence is indicated on the right-hand side.

Typical crater profiles and morphology, crater geometry and the amount of removed material for *zones 7-9* (62%, 66% and 71% Al at. %) ablated with a laser fluence of 18.9 J/cm^2 are given in Figure 5.15. The ratio between the absorbed fluence and the estimated threshold fluence is shown for comparison. Crater profiles (Figure 5.15a) and SEM images (Figure 5.15b) revealed similarities between *zones 8* and *9,* with irradiated areas where the silicon substrate was slightly damaged and a HAZ consisting mainly of re-deposited melt on the crater edge. Craters in *zone 7* show, in contrast, a HAZ where the thin film was removed by evaporation but did not reach the substrate.
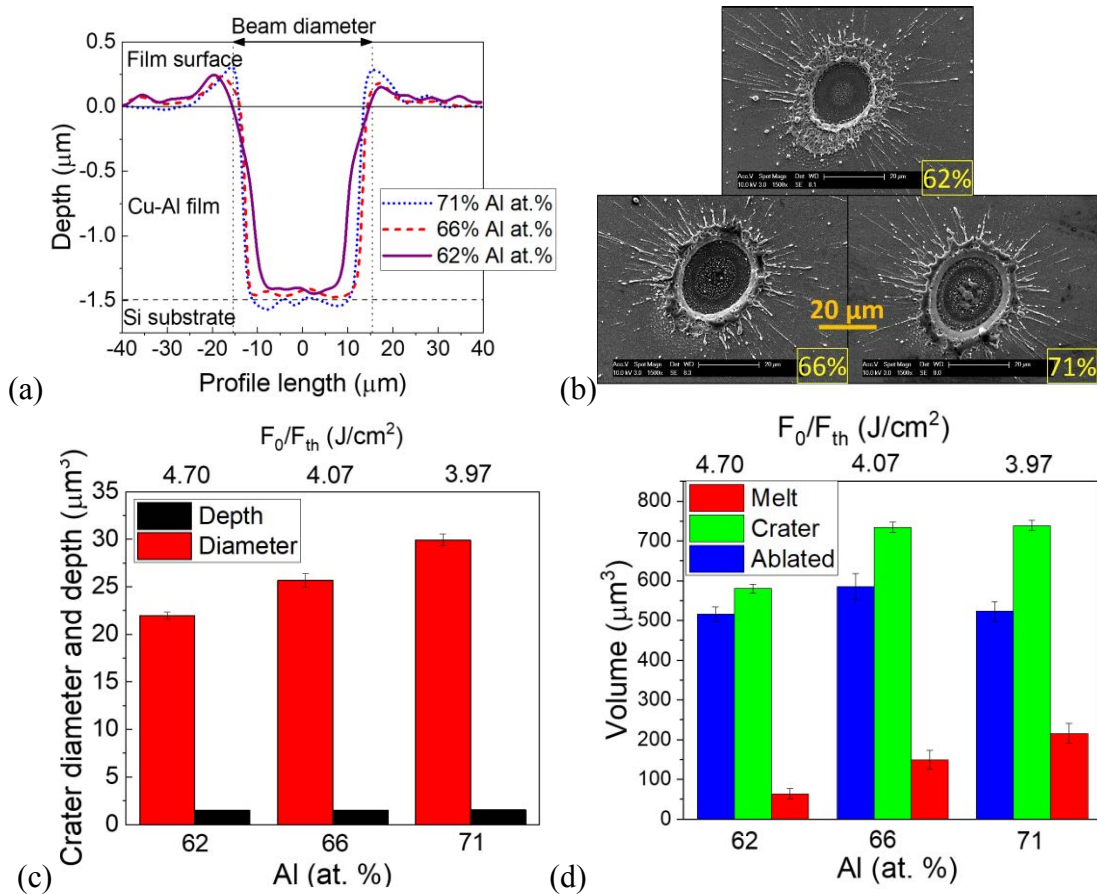
Figure 5.15 Experimental results for zones 7-9 irradiated with a constant laser fluence of 18.9 J/cm² : typical crater profiles (a); typical crater morphology – the scale bar is 20μm (b); crater depth and diameter (c); Measured volumes (d).

Crater depths were overall in the range of the film thickness, while crater diameter increased with the addition of aluminium (Figure 5.15c), which reflect in the measured volumes (Figure 5.15d). The change in the crater diameter was correlated with the variation of the re-deposited material, suggesting that at the end of the ablation process more melt was carried away from the irradiated area by the drag forces through piston effect and cooled down in the process. It is likely that at an earlier stage in the ablation all three craters had similar morphologies (resembling the one in *zone 7*). The first direction of the heat flow (vertical) together with the Gaussian energy distribution

(highest intensity in the centre) would have led to material being removed first in the centre of the irradiated area. The reflection of the heat wave from the substrate back into the thin film would have then increased the diameter of the fully ablated area (where the substrate is visible in Figure 5.15b). A potential explanation of the different heat affected areas (and crater diameter) would be the higher melting point of *zone 7* (921 K) compared to *zones 8* and *9* (870 K and 862 K respectively, values obtained from the phase diagram). A higher melting point would mean a delayed onset of material vaporisation and less energy reaching the substrate to be used for laterally expanding the crater.

5.5 SUMMARY

This chapter investigates how slight changes in chemical composition affect the material response to irradiation, which is evaluated by crater shape, volume and morphology. Laser ablation of the binary Cu-Ni alloy was used to investigate how variation in the chemical composition affects the material's response to irradiation with constant laser parameters for a smooth surface and a compact thin film. Estimation of the ablation threshold showed very similar threshold fluences for a Cu-rich and a Ni-rich area (with a 42% variation in Ni at. %), and measurements indicated almost identical behaviour in both crater geometry and volume. The craters had a typical Gaussian profile and the silicon substrate was ablated, suggesting a strong vertical heat flow and little thermal resistance at the thin film-substrate interface. Crater diameter was only slightly higher in the copper-rich area and craters showed a significant amount of recast material on the edges due to re-deposition of substrate material. The results in the binary Cu-Ni alloy resemble the ones obtained for pure Cu and Al samples, indicating that the influence of the change in chemical composition to the crater shape was minimal.

The analysis of the binary Ni-Al system enabled the study of ns laser ablation of thin films when a change in chemical composition was accompanied by variations in thin film microstructure. This contributed to understanding the separate influence of surface morphology and film microstructure on the geometry and morphology of the craters. The film where tightly packed structures were present possibly had an enhanced interface roughness which would in turn increase the magnitude of the thermal barrier as to reflect the heat wave. The presence of a well-defined surface morphology seemed to have changed the energy distribution of the beam, redirecting more energy towards the edges and away from the centre. These effects combined could, to some extent, limit thermal damage to the silicon substrate, up to a point where the energy delivered to the sample exceeds a threshold value.

The third section was aimed at investigating the material response to laser ablation of a Cu-Al thin film compositional gradient with well-defined microstructure. Based on preliminary results, three areas with different chemical composition and similar microstructure were analysed in terms of crater geometry, morphology and amount of removed material. It has been shown that the change in the chemical composition would potentially affect the ablation result provided that a steep change would occur in the alloy properties. In this particular case, the different melting point of the three areas enabled further understanding of the vertical and lateral heat flows in the material, in terms of their temporal sequence and effect on crater morphology.

6 LASER ABLATION OF TERNARY COMBINATORIAL THIN FILM LIBRARIES

The previous chapters were dedicated to the study of pure copper, aluminium and nickel thin films and their binary compositional gradients. The final experimental chapter presents one of the first studies which investigate laser ablation of a ternary copper-aluminium-nickel alloy thin film using a single laser pulse of constant parameters (fluence, wavelength and pulse duration) on combinatorial material libraries. It is aimed at illustrating how variations in chemical composition and film morphology affect the crater characteristics. In the end of this chapter, in addition to the binary Cu-Ni-Al film, a second ternary film with compositional gradient (Cu-Al-Zr) was used to emphasise similarities in terms of crater shape and morphology between the two ternary alloys.

A part of the results presented in this chapter has been published by the author [162].

6.1 EXPERIMENTAL DETAILS

Dictated by the variations which naturally exist in material libraries, the first part of this chapter is aimed at the characterisation of the as-deposited thin film. Measurements of reflectivity, elemental distribution and thin film thickness prior to irradiation are relevant to ns pulsed laser ablation ("thermal regime") and they are used for a qualitative analysis of the single-pulsed ablated craters. Subsequently, micrographs obtained by scanning electron microscopy are used to illustrate the variations in both the thin film sample (prior to ablation) and the crater morphology (after ablation). The variations in the crater morphology and geometry are discussed with respect to the optical

characteristics of the as-deposited thin film as well as its elemental distribution and the physical properties of Cu, Al and Ni. Profiles and ablated volume of the craters are obtained by 3D optical microscopy and used to quantify the ablation result.

The ternary compositional gradient film used in this study was deposited on a 4-inch diameter silicon (100) wafer, in a magnetron sputtering facility (Mantis Deposition Ltd, UK, Model: QPrep). The targets used were aluminium, copper and nickel (99.95%, 99.99% and 99.95% purity respectively), and were sputtered simultaneously at different discharge powers to achieve the desired composition (RF – 173 W, DC – 67 W, DC – 28 W respectively). A turbo-molecular pump backed by a dry rotary pump ensured a base pressure of 2×10^{-4} Pa. The gradient was obtained by decreasing the target-to-substrate distance to 8 cm and without substrate rotation, in argon atmosphere (Ar = 45 sccm, 0.3 Pa) and at room temperature.

Mapping of the chemical composition was done by energy-dispersive X-ray (EDX) spectroscopy, equipped on a Philips XL30 scanning electron microscope. Certificated microanalysis standards (Oxford Instruments Link ISIS EDX microanalysis system) were used for the quantification of the three elements with an acquisition time of 60 s. Surface characterisation of the as-deposited thin film was performed by high-resolution electron microscopy (SEM Hitachi S480, acceleration voltage 1.5 kV) and atomic force microscopy (AFM NT-MDT Solver Pro-M operating in tapping mode, using a nominal tip radius with 15 nm radius of curvature). Topographic parameters (i.e. root mean square roughness and height-height correlation length) were obtained from the 10x10 μm^2 AFM scans using Gwyddion software. The size of surface features was determined from the micrographs using ImageJ software. The reflectivity R (%) was measured at 15 areas

(5x10 mm) on the sample, with a Perkin Elmer UV/VIS/NIR Lambda 900 spectrophotometer.

Laser ablation was carried out using a SPI G4 20W HS Series L Type air cooled ns pulsed fibre laser module, operating at 1064 nm wavelength, with a focused spot size diameter of 49.8 µm. The experiments were performed in air at atmospheric pressure. The target surface was treated as consisting of 72 square areas, each with 5 mm side length, in an 8x9 matrix (Figure 6.1). Within a given area a_{ij}, the chemical composition varies by less than 1 at. %, which can be considered constant. The brighter coloured areas designated in Figure 6.1 were chosen for further investigation to cover the full compositional spread while maintaining a manageable number of experiments. Each area had a line of individual ablated craters using a constant laser fluence of 4.54 J/cm^2 and pulse duration of 30 ns (optimised to prevent the crater from penetrating the substrate), separated by adjustment of the machine feed speed to avoid crater overlapping. As opposed to the experiments carried out on pure and binary films where damage and ablation of the films was obtained at pulse duration of 55 ns, the ternary films ablation was noticed at shorter pulse duration. This could be due to the different temporal shape of the beam, considering that different laser equipment was used.

Crater geometry was measured with *Alicona InfiniteFocus* as described in 3.3.4. A magnification of 20× was used, with a corresponding resolution of 50 nm vertically and 2.93 µm laterally. The ablated volume per crater in any area of constant chemical composition was calculated by averaging the values measured in 10-12 different craters. Cross-sections of the ablated craters were then prepared via focused ion beam using a dual beam SEM-FIB Tescan Vela instrument in a two-step approach. First, a rough cutting step with high Ga-ion beam (30 kV beam and 3 nA probe current) was used to

mill a rectangular trench, followed by a fine polishing step (30 kV and 1 nA) in the area of interest.
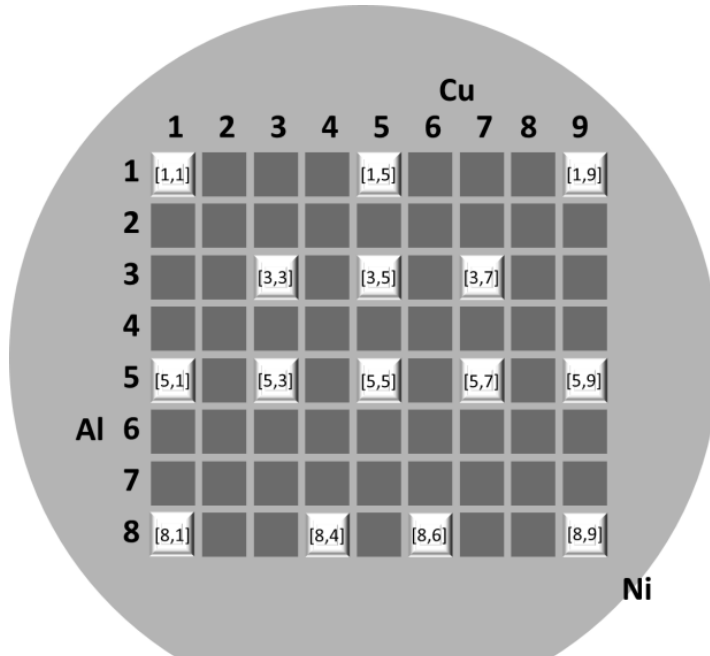
Figure 6.1 Schematic representation of laser processing and analysis of the ternary alloys. The position of the sputtering targets with respect to the substrate is shown.

6.2 LASER ABLATION OF TERNARY CU-NI-AL MATERIAL LIBRARY

The 30-ns IR laser irradiation of a metal thin film places the ablation process in the thermal regime, which consists of three main steps. *(i)* Laser radiation is absorbed by the workpiece in an area under the surface equal to the skin depth (several nm in the case of metals irradiated with IR), and the amount of energy absorbed by the sample is directly related to its reflectance at the laser wavelength (1064 nm). *(ii)* The energy is then distributed to the rest of the material by heat transfer. The maximum temperature and heat diffusion length are dictated by the thermal properties (e.g. thermal diffusivity, fusion and boiling points, melting and evaporation enthalpies) of the thin film, as well as the surface

morphology and topography. Particularly in the case of thin films, heat transfer is influenced by the thickness of the film, substrate type and the nature of the interface between those two. *(iii)* Significant ablation occurs when the surface reaches the vaporization temperature, or even sooner (around the melting point), depending on the vapour pressure at the target surface. Depending on the laser pulse duration and thermal properties of the thin film, heat transfer to the substrate becomes significant and leads to the ablation of both film and substrate.

To study the laser-material interaction on a compositional spread it is essential to understand the workpiece properties prior to laser irradiation. However, published information about the material properties (e.g. reflectivity), particularly on such broad range of chemical compositions, is very limited and the synthesis technique itself can lead to different material properties and surface morphology. Hence, the first part of the results focuses on the as-deposited sample characterisation.

The compositional range covered by the sample is shown superimposed on a ternary phase diagram for the Cu-Ni-Al system in Figure 6.2. The equilibrium phases present at these chemical compositions represent a good starting point for analysis and are given in Table 6.1.

Table 6.1 Expected equilibrium phases present in chemical composition range covered by sample.

Symbol	Phase	Structure
α	Ni-Cu	FCC solid solution
α_1	$Ni_3Ni\text{-}Al_2CuAl$	FCC superlattice
β_2	NiAl	BCC superlattice
γ	Cu_9Al_4	Complex cubic
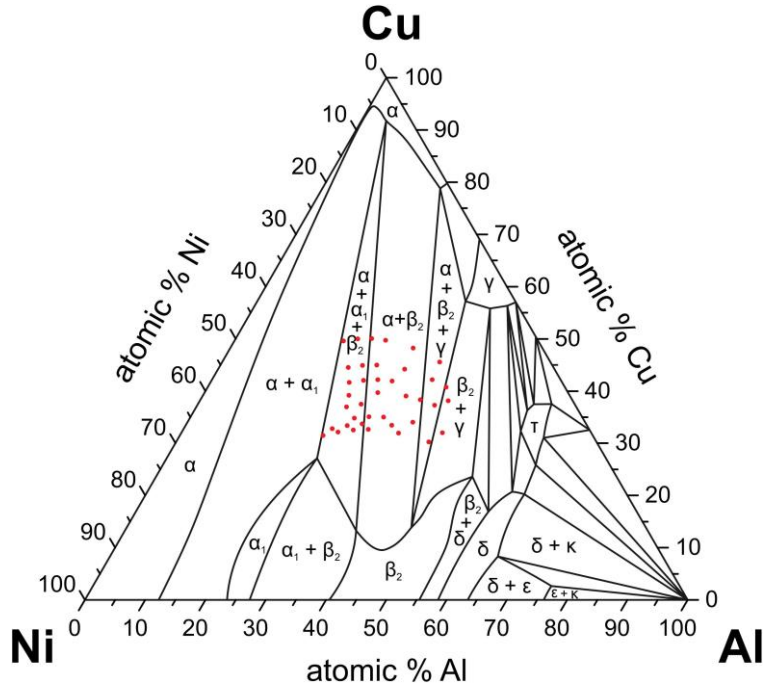
Figure 6.2 Ternary Cu-Ni-Al phase diagram adapted from [163] showing the region covered by this compositional gradient sample.

The sample thickness varied between 1 and 1.35 μm and was used as a reference when analysing crater depth. Previous experiments on laser ablation of metallic thin films have demonstrated that the ablation threshold increases linearly with the film thickness up to the thermal diffusion length, after which it remains constant [115]. A simple calculation of the thermal diffusion length for each of the elemental film components is useful for understanding heat transfer in these experiments. Using a film thickness of 1 μm and a pulse duration $\tau = 30 \; ns$, the thermal diffusion length ($\delta_{th} = \sqrt{2\tau k}$, thermal diffusivity $k = K/\rho c$, where k is the thermal conductivity, ρ the density and c the specific heat) is $\delta_{th-Cu} = 2.60 \; \mu m$, $\delta_{th-Al} = 2.25 \; \mu m$, $\delta_{th-Ni} = 1.16 \; \mu m$ for copper, aluminium and nickel respectively (thermal diffusivity at room temperature taken from [149]). As the film thickness is smaller than the thermal diffusion length and the beam spot is around 50 μm, heat conduction is effectively unidimensional, and the thermal

behaviour of the system is affected by the properties of silicon, with the substrate acting as a heat sink in these experiments.

The reflectivity at 1064 nm wavelength (Figure 6.3) decreases with aluminium content (for concentration see Figure 6.2); the area richest in Al has the lowest reflectivity (R~30%) and will thus absorb a higher amount of the incoming laser radiation compared to the area with least Al (R~70%). These values are found to be generally lower than the overall values for reflectivity of the three metals at 1064 nm (Cu ~ 90%, Al ~ 80% and Ni ~ 70% of the incident radiation [75,76]). The optical properties of a material are not determined solely by chemical composition, therefore surface microstructure and topography analysis was performed.
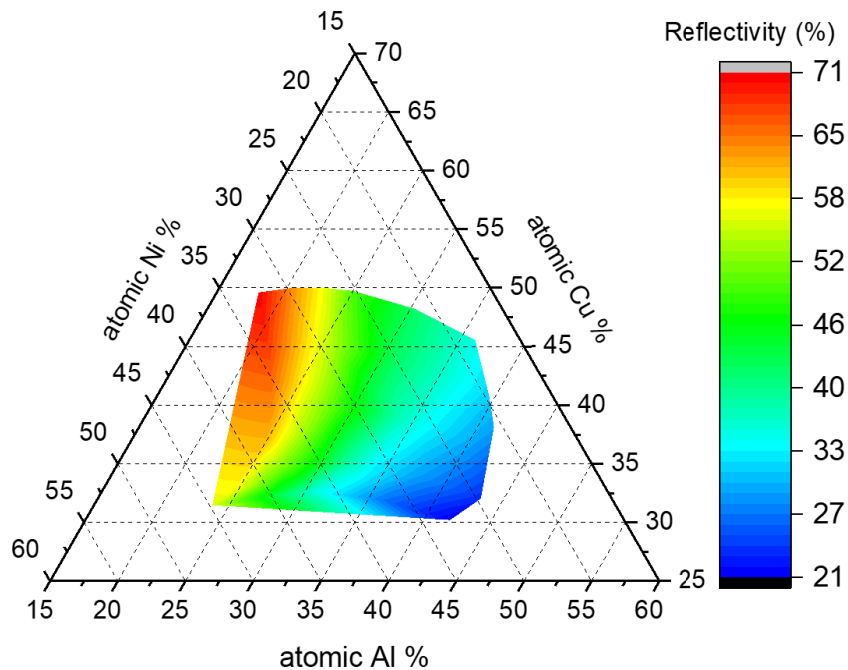
Figure 6.3 Total reflectivity of ternary Cu-Ni-Al sample (1064 nm) as a function of chemical composition.

The micrographs taken at five different areas across the film surface (shown in Figure 6.4) revealed variations in film microstructure. The legends shown in Figure 6.4a-

e are the reflectivity (R), root mean square roughness (σ_{RMS}) and chemical composition (Al, Cu, Ni at. %). The SEM images and the AFM scans are in good agreement in terms of surface characterisation. The results show that, besides the compositional gradient across the surface, the Cu-Al-Ni thin film exhibits a morphological gradient as well, as observed in the Al-metal binary films. In the area with least aluminium (at. %), dominated by a copper-nickel solid solution, the surface is relatively smooth, with surface structures in the range of 10 nm (Figure 6.4a). The results indicate that with an increase in the Al concentration (18% - 43%), the structures develop and grow in number and size (Figure 6.4a-e). As the structures increase in size (up to ~500 nm, shown in Figure 6.4d), their morphology also changes, and they develop 'clear cut' edges. Finally, the Al rich area is covered in tightly packed, well-defined structures with a smooth texture, which are about 200 nm in size (Figure 6.4e). The structures on the sample surface are a consequence of both the compositional gradient [164] and the sputtering process dynamics [158]. While the shape and size of the structures varies from the pure and binary films, similarities in surface morphology were identified for all samples.
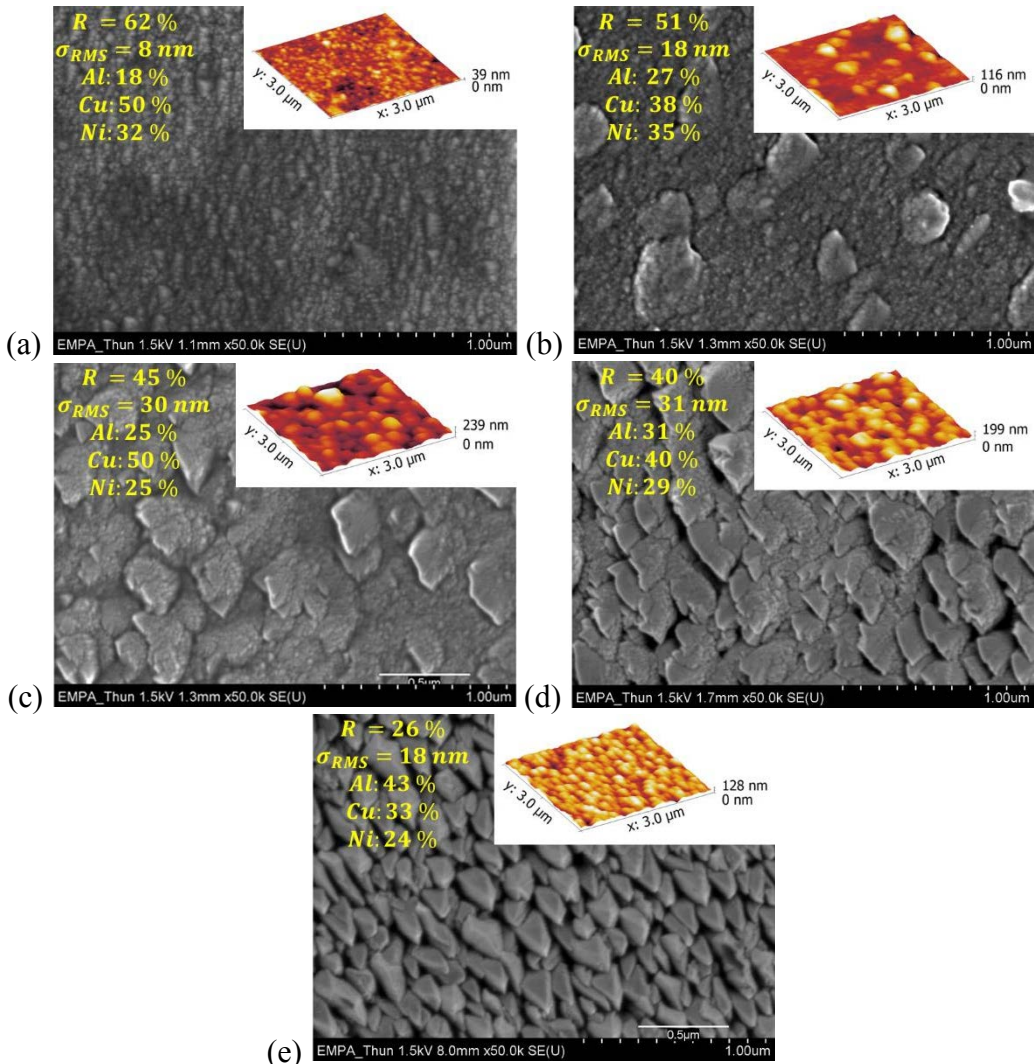
Figure 6.4 SEM images and 3x3 μm² AFM scans of the as-deposited thin film in several areas across the target surface: (1,8) (a); (5,7) (b); (1,5) (c); (5,5) (d); (8,1) (e). The values for the reflectivity, surface roughness, and chemical composition are given for comparison.

The physical dimensions of the structures should be considered when trying to assess the correlation between surface morphology and the increased absorption of laser (as shown in Section 3.2). Root mean square roughness (σ_{RMS}) and height-height correlation length ($h - h$) are given in Table 6.2. The values indicate a smooth sample surface, with features at least one order of magnitude smaller than the laser wavelength.

The topography with higher σ_{RMS} and $h - h$ (e.g. Sample (8,1) shown in Figure 6.4) is hypothesized to increase the absorption by creating a gradual change in the refractive index [165] (i.e. "moth-eye effect").

Table 6.2 Surface parameters of five areas across the sample.

Sample ID	σ_{RMS} (nm)	h-h (nm)
(8,1)	18	80
(5,5)	31	138
(1,5)	30	179
(5,7)	18	214
(1,9)	8	286

The first step in crater analysis was to estimate the amount of energy needed to ablate the ternary compositional spread. The ablation threshold of several areas on the sample matrix was obtained using the measured reflectivity and the calculated thermal properties of the sample (see Sections 4.2 and 5.2). The preliminary results indicated that the ablation threshold was strongly dependent on the aluminium atomic percentage in the studied thin film, while the amounts of copper and nickel had a negligible influence. As the surface morphology was dependent on the Al content, the results were plotted against the aluminium atomic percentage.

The crater depth and the average diameter are given in Figure 6.5. Crater depth has been shown in previous studies to have a linear increase with the fluence, i.e. where the target was a material with known properties and the laser parameters were varied (see, for example [166]). However, as discussed in previous chapters, surface structures could lead to deformation of the beam (i.e. widening), so less energy would become available to induce a vertical heat flow and material removal.
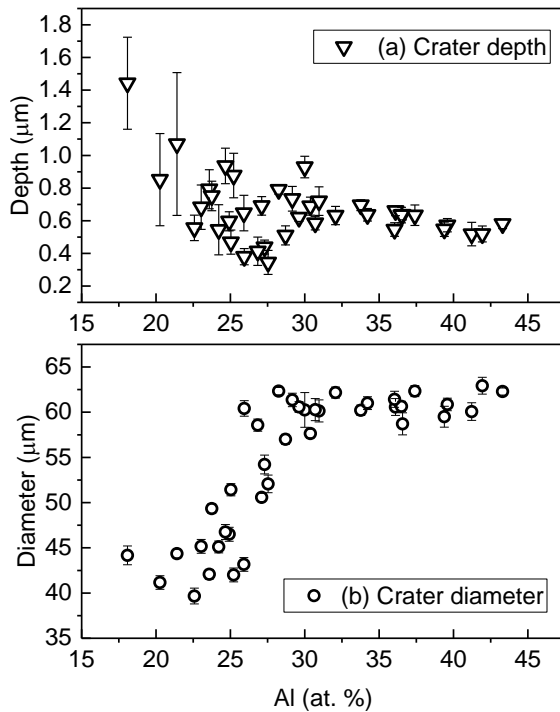
Figure 6.5 Crater depth (a) and average diameter (b) as a function of Al at. %.

In Figure 6.6 the variation of the rim volume (top), crater volume (middle) and resultant ablated volume (bottom) as a function of aluminium concentration are shown. The rim volume (top) was inversely proportional to the amount of Al (*region 1*) up to 27 at. %, after which it slightly increased (*region 2*). The crater and ablated volumes (middle and bottom respectively) showed an inverse correlation with Al content, i.e. both increased rapidly (*region 1*) up to 30% Al, after which they slightly decreased (*region 2*). These two turning points (27 at. % and 30 at. % Al) marked a transition area which was not only observed when quantifying the amount of removed material, but also indicates where the transition in crater morphology occurred. Figure 6.6 (bottom) also shows that the lowest volume corresponds to the area with least Al. This could be explained by the
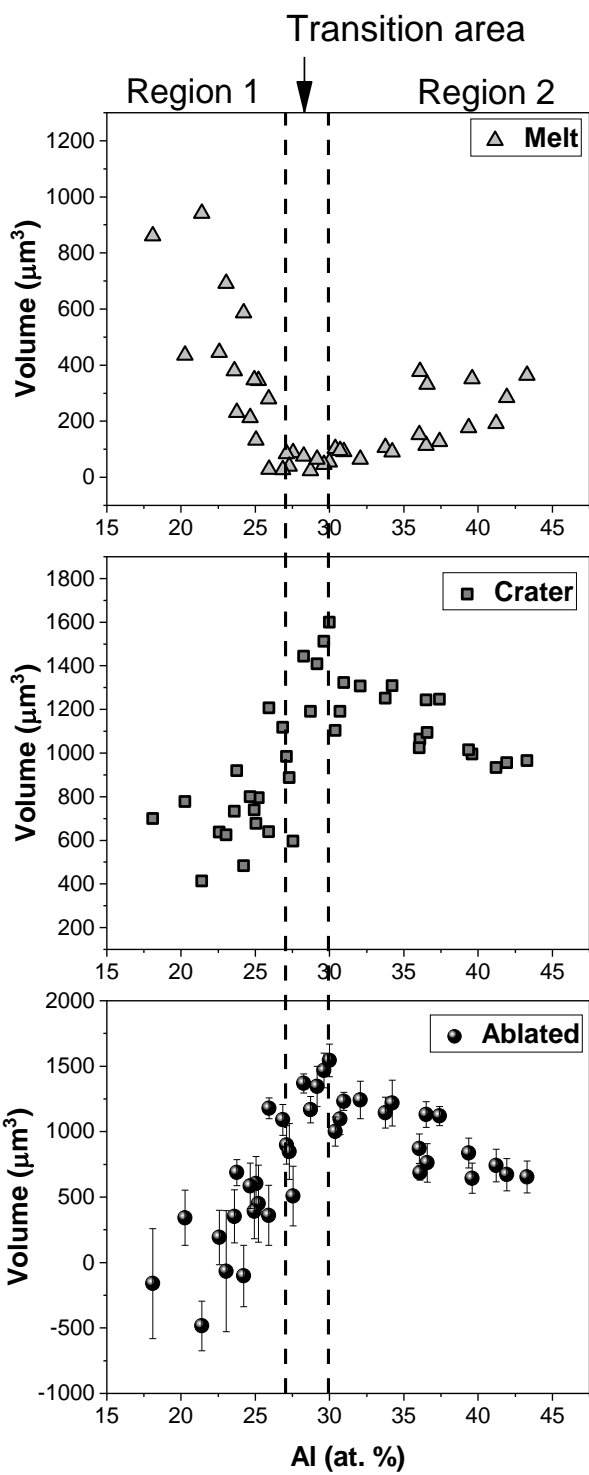
Figure 6.6 Melt (volume above the surface) – top, crater (volume below surface) – middle, and resultant ablated volume – bottom, as a function of aluminium atomic percentage.

similar values of the crater volumes (Figure 6.6 – middle) and the rim volumes (Figure 6.6 – top) at lower Al concentration, revealing that material was transported rather than actually removed from the sample. This, together with the quite large error bars (which may be considered evidence of the non-linear interaction between the beam and the workpiece), indicated that the energy input was close to the ablation threshold of the sample. With further addition of aluminium, the ablated volume increased up to the maximum value of ~1500 μm^3, suggesting that the sample absorbed more energy than the ablation threshold value. The subsequent decrease in the resultant ablated volume was caused by both diminishing of the crater volume itself, as well as the built-up of re-solidified material around the craters. To illustrate the behaviour of both variations of crater-melt and crater geometry, crater profiles corresponding to *region 1*, *region 2* and the transitional area are shown in Figure 6.7.
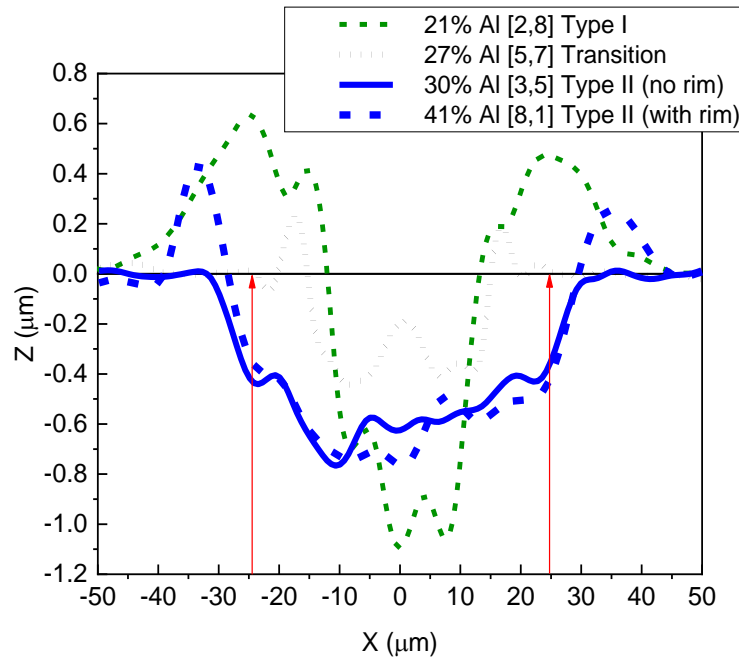
Figure 6.7 The evolution of typical crater profiles with an increase in Al percentage. Z=0 represents the surface of the thin film and the red arrows indicate the beam diameter at the target surface.

The reduced amount of removed material after the maximum value found at ~30% Al (at. %) could be explained by an increase in the optical density of plasma, which absorbs the laser radiation. In other words, when irradiating metals with ns IR laser pulses in atmospheric conditions, plasma formation threshold was reported to be just 0.1 – 0.2 J/cm^2 higher than the ablation threshold [75,76]. Thus, with the lower ablation threshold more material vaporised, leading to the formation of a dense cloud in front of the target. The plasma is ignited and, depending on its density, absorbed a certain amount of the incoming laser radiation [85]. The smaller the ablation threshold, the more material vaporises early in the process, and the more absorbent the plume becomes. Along with the ablated volume, crater shape and morphology gradually changed across the sample surface, with transitional features observed in areas with 27% - 30% Al at. %. Judging by the similarities observed in shape, re-deposited material and the quantities of material removed, two categories of craters have been identified, corresponding to *region 1* and *region 2* discussed in Figure 6.6. Craters in *region 1* ('Type I' in Figure 6.7) had a higher aspect ratio than craters in *region 2* ('Type II' in Figure 6.7), and had a significant amount of re-solidified material on the edge. The shape changed in the transitional area ('Transition' in Figure 6.7) between *region 1* and *region 2*, as the craters became wider and shallower, and the rim of re-solidified material significantly decreased. Craters in *region 1* exhibit a relatively smooth crater bottom, up to the transition area (as shown in Figure 6.8a – right hand side), after which all the craters (found in *region 2*) had an interconnected, porous surface, which appeared to be re-solidified material 'frozen in motion' (Figure 6.8b – right hand side).

In addition, the composition of the thin film, the change in crater shape for craters in *region 2* was attributed to the columnar structure of the as-deposited thin film (Figure

6.8b – left hand side). This morphology reduced the thermal contact between the thin film and the substrate (i.e. higher thermal contact resistance), minimising heat losses to the substrate compared to craters in *region 1*, as discussed in the previous chapters. The type I craters identified in the ternary sample correspond to craters in pure copper and aluminium, and type II craters are similar to the one identified in pure nickel in terms of crater morphology and the extent of the HAZ.

(a)

(b)
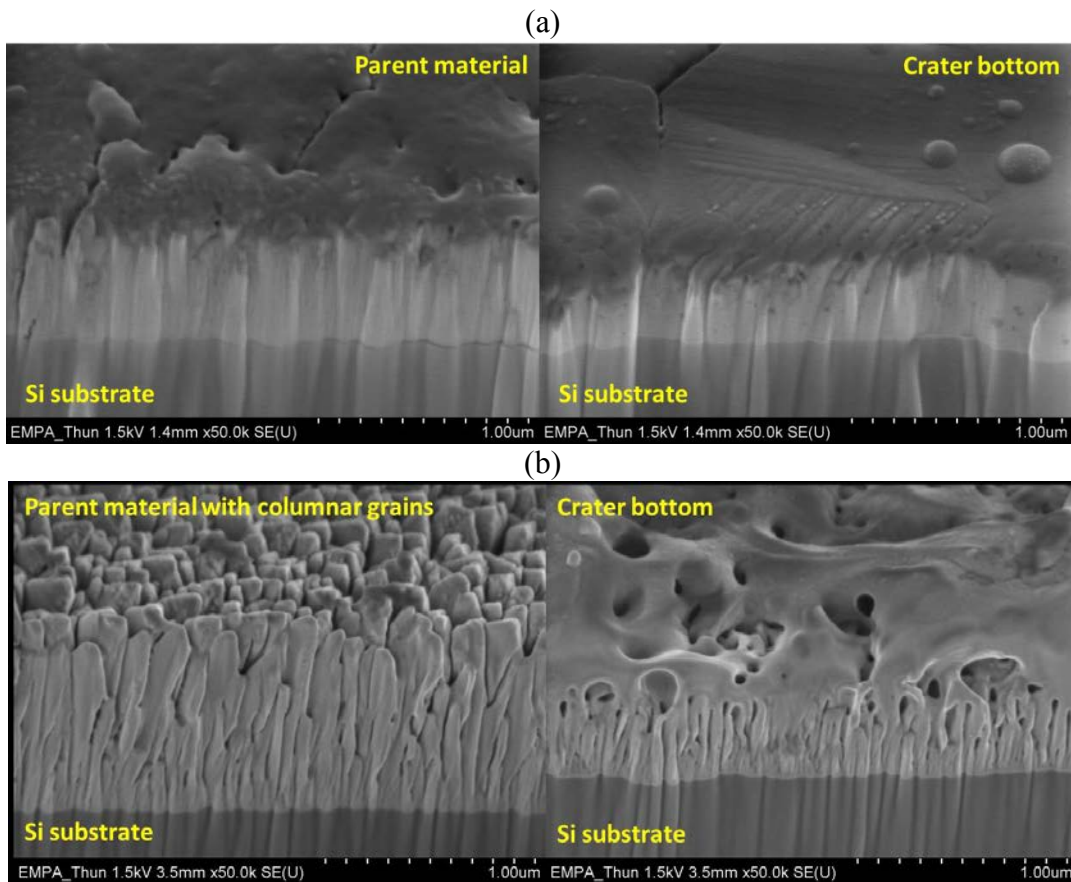
Figure 6.8 : SEM images of cross sections of the as-deposited thin film (left) and crater (right) in (a) region 1/ transitional area and (b) region 2, showing the typical film morphology.

A notable difference regarding crater shape was related to the top-view of the irradiated areas which, in certain areas of the Cu-Ni-Al ternary sample was elongated (i.e.

elliptical shape), while in other areas it had the typical circular shape (corresponding to the cross-section of the beam profile). This could be a consequence of the deformation of the laser beam in contact with a structured surface. Further discussion on these elliptical craters is carried out in the next section, which is aimed at understanding whether the identified material response is limited to the studied samples (i.e. alloys of copper, aluminium and nickel).

6.3 TERNARY CU-NI-AL AND CU-AL-ZR: A COMPARISON OF CRATER GEOMETRY AND MORPHOLOGY

Identical laser processing with the one carried out on copper-aluminium-nickel detailed in Section 6.1 has been carried out on a different ternary compositional gradient, a Cu-Al-Zr ternary alloy (i.e. single pulse craters using 30 ns pulse duration and 4.54 J/cm^2 fluence). In addition to its potential applications as a bulk metallic glass [167,168], Zr has much higher melting and boiling points and an even lower thermal conductivity compared to Ni. The aim of this comparison was to investigate whether the observed variations in the ablation result were sample specific. The chemical composition covered by the material library is indicated on the phase diagram in Figure 6.9.

Thin film thickness was in the range of 0.77 – 1 μm, and the overall reflectivity of the sample (Figure 6.10) was higher than the reflectivity of the ternary Cu-Ni-Al alloy (Figure 6.3), which resulted in shallower craters, with irregular profiles when irradiated with the same conditions. Hence for comparison between the two ternary alloys only crater diameter was further discussed.
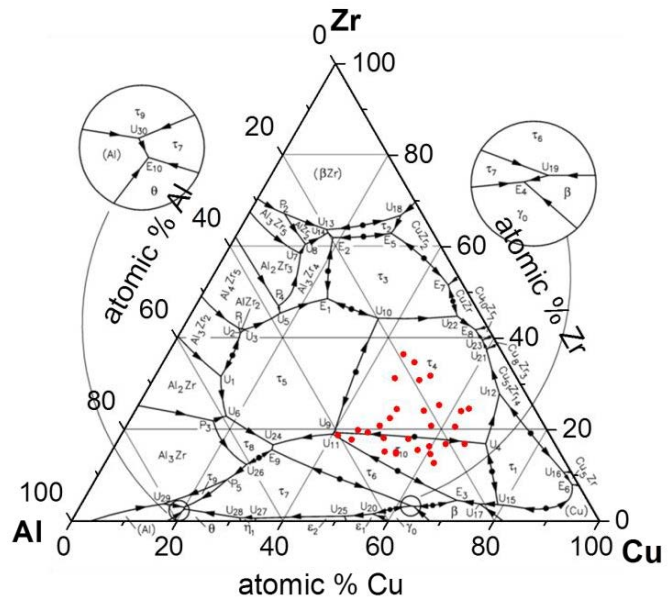
Figure 6.9 Ternary Cu-Al-Zr phase diagram (computed liquidus projection) adapted from [169] showing the region covered by the compositional gradient sample.
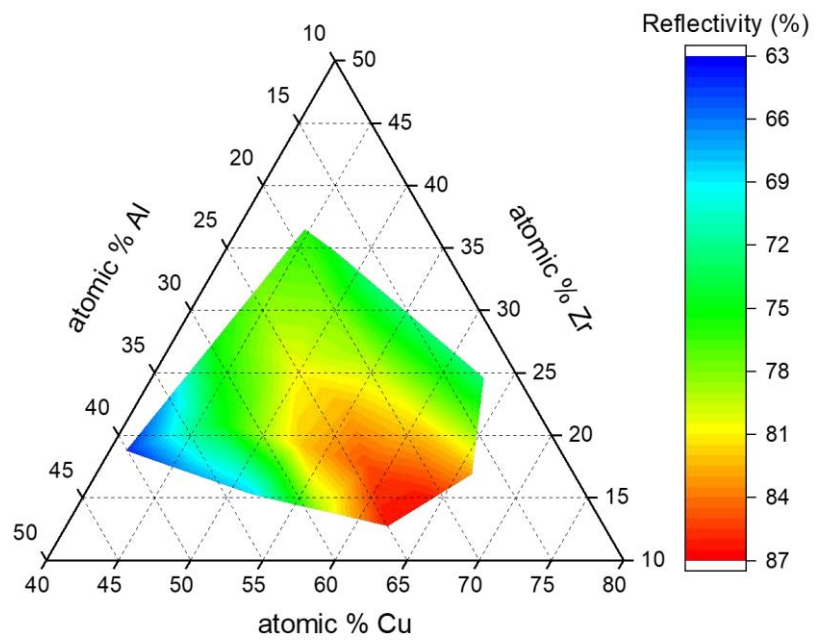
Figure 6.10 Reflectivity of the ternary Cu-Al-Zr sample at 1064 nm.

In the previous section on ternary Cu-Ni-Al film, it has been shown how crater morphology changes with the chemical composition and microstructure of the as-deposited thin film. To gain a deeper understanding of the extent of these variations, first a step-by-step SEM imaging of the transition area has been performed (shown in Figure 6.11).
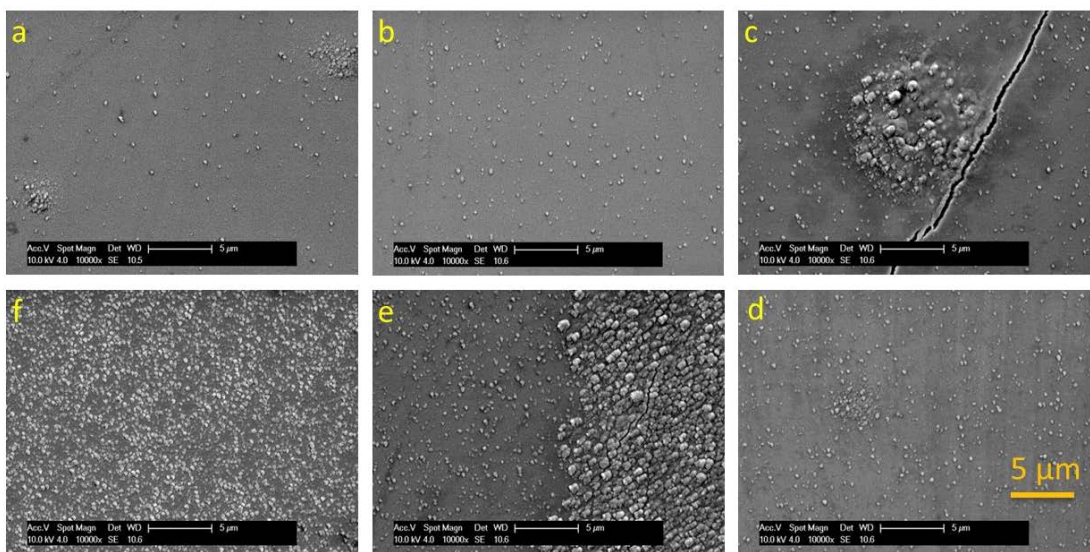
Figure 6.11 Transition area in film morphology, clockwise: from a smoother surface (a) to a rougher surface (f) for Cu-Ni-Al material library. The variation in chemical composition for all areas is less than 2 at. % Al, with maximum concentration in image f.

On the smooth thin film surface (see Figure 6.4a) isolated grains were present and small clusters started to form (Figure 6.11a). With minor variations in chemical composition the grains became denser (Figure 6.11b-f) and the clusters grew. In Figure 6.11a clusters were around 2 μm, increasing in size and causing what appeared to be stress fractures in the film (Figure 6.11c). Highest observable cluster size was in the range of tens of microns and is partially seen in Figure 6.11e, right hand side. Cluster growth and

111

agglomeration of grains eventually led to the micro-structured surface shown in Figure 6.4f.

Further, two areas of similar chemical compositions (i.e. 31-24-45 and 32-26-42 Cu-Al-Ni at. % respectively) were investigated. The as-deposited thin film morphology and chemical composition together with the crater details are given in Figure 6.12. Although the two typical craters were in the transition area, these are representative of *region 1* (left hand side) and *region 2* (right hand side). Despite a slight change in chemical composition, the as-deposited thin film microstructure differed considerably between the two regions: *region 1* showed a smooth surface covered partially in grains, and this resulted in deeper and narrower laser ablated craters which exhibit re-deposited material on the thin film surface. In *region 2* the surface was packed with grains which in turn lead to wider and shallower craters. The crater bottom showed dark marks which could be associated with boiling centres (Figure 6.12c, right hand side).

A similar variation in the as-deposited thin film microstructure was also identified in the second ternary composition gradient, namely the Cu-Al-Zr sample, with transition areas delimiting a smooth surface of the film from the one with well-defined surface structures. The step-by-step characterisation of the Cu-Al-Zr thin film microstructure is given in Figure 6.13. Despite surface grains having different shapes, comparable ablation results were observed, i.e. for areas of similar chemical composition, variations in crater shape and morphology was observed. To illustrate these changes, SEM micrographs of thin film prior to ablation and their corresponding craters are shown in Figure 6.14 and Figure 6.15.

Chemical composition (Cu-Al-Ni, at. %)	
31-24-45 (*region 1*)	32-26-42 (*region 2*)

a) Parent material

2 µm

b) Crater – top view

V=687
D=49
h=0.75

V=1178
D=60
h=0.38

20 µm

c) Crater bottom - detail

1 µm
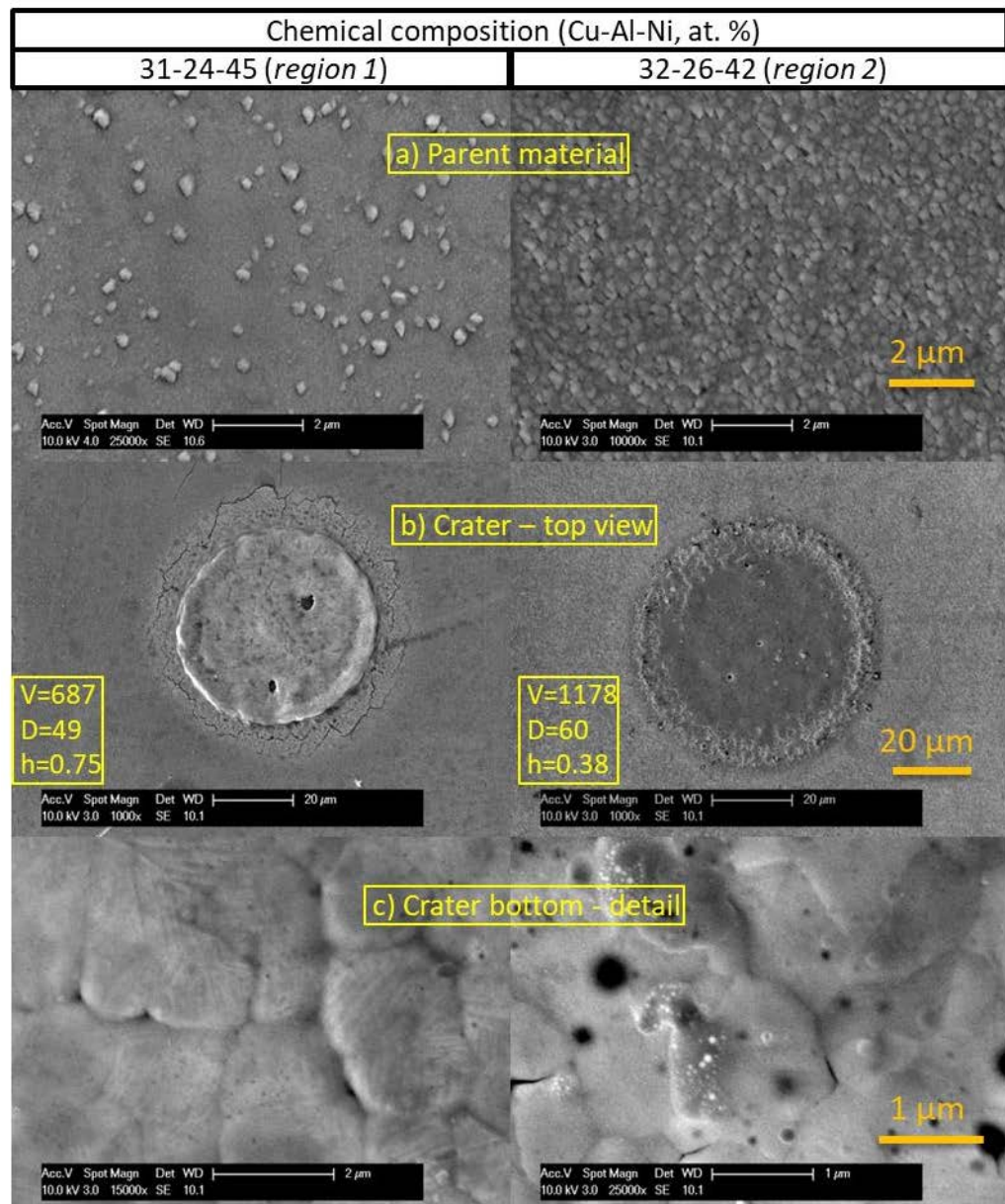
d) Crater profiles

Figure 6.12 Investigation of the laser ablated craters in the transition area. Two regions of similar chemical composition are shown: as-deposited thin film (a), top view of craters (b), detail of crater bottom (c) and crater profiles (d). Marked on the crater images are the ablated volume V (µm³), crater diameter D (µm) and depth h (µm).

The crater morphology is essentially given by the state in which the material re-solidified. When the energy absorbed by the sample is high compared to what the material requires for the onset of evaporation, the ablation result is a well-defined crater, as seen in the case of the copper-aluminium-nickel sample. However, when the absorbed energy was closer to the ablation threshold, as was the case for the copper-aluminium-zirconium, the ablation footprints were representative of earlier stages of ablation, for example the onset of boiling and evaporation. This effect is illustrated in the next paragraphs. The following figures show the as-deposited thin film, a crater overview and a crater detail to depict ablation results. To offer a rough guide to the reader, on each set of images is indicated the chemical composition of the area, as well as the estimated ablated threshold calculated as shown in Section 4.2.
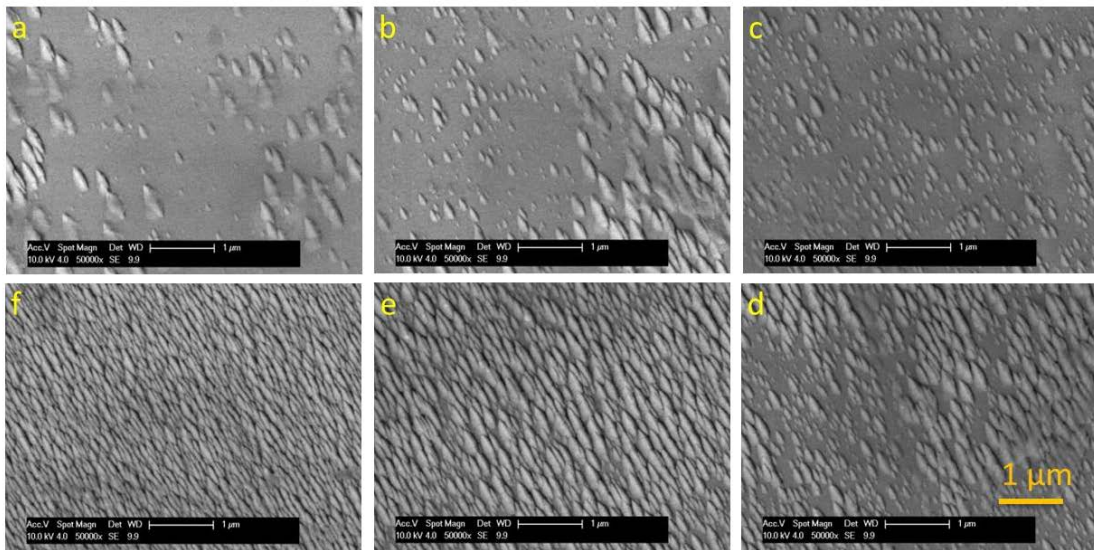

Figure 6.13 Transition area in film morphology, clockwise: from a smoother surface (a) to a rougher surface (f) for Cu-Al-Zr material library. The variation in chemical composition for all areas is less than 2 at. % Al with maximum concentration in image f.

A relatively smooth as-deposited thin film (i.e. scarce grains and clusters formed on the surface) with the corresponding craters are shown in Figure 6.14. All craters initially showed a smooth bottom (Figure 6.14b, Area 1) with ripples forming at the edges (Figure 6.14c, Area 1).
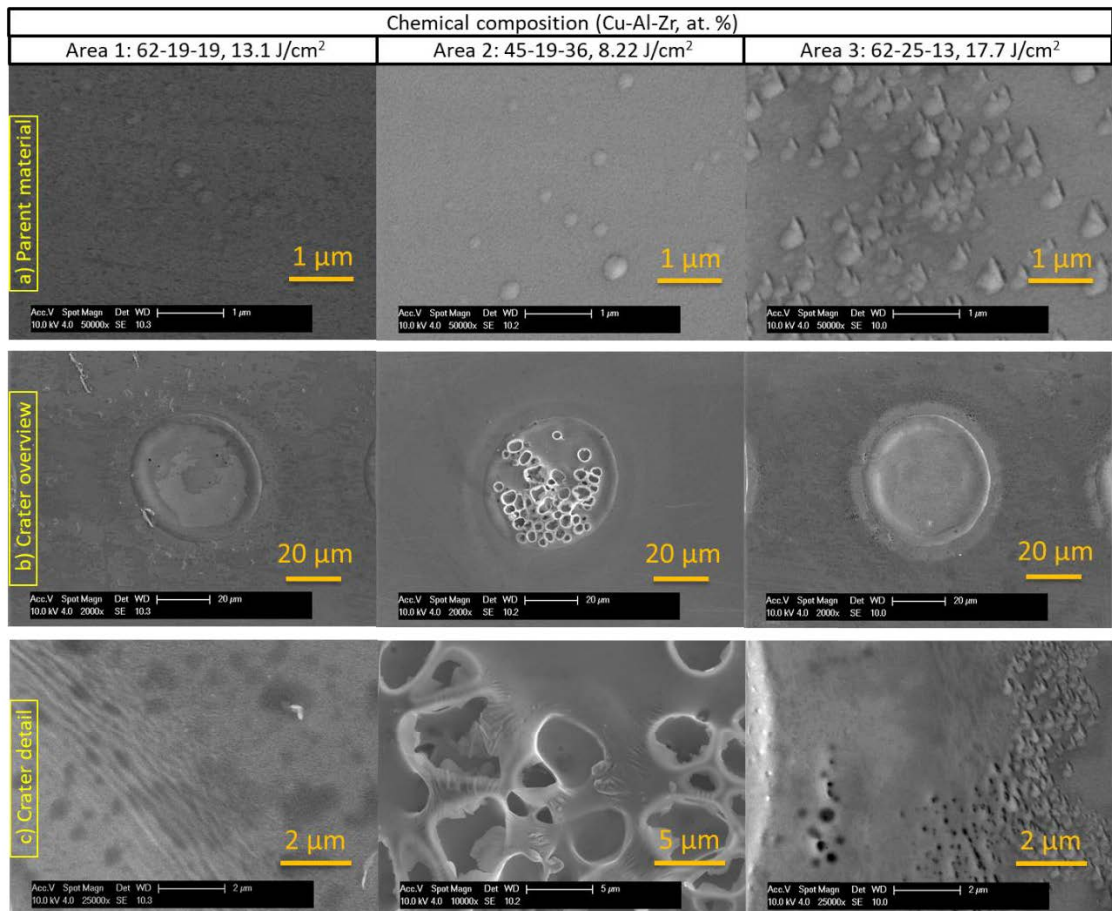
Figure 6.14 Micrographs of the as-deposited thin film (a) and the corresponding ablated craters (b) and detail (c) for three areas of the Cu-Al-Zr thin film where the thin film is relatively smooth. The chemical composition and the estimated ablation threshold based on material properties is given at the top of the image.

These ripple patterns are similar to the ones discussed in [168], therefore their formation could be attributed to the two different fluid layers (i.e. the molten layer and plasma plume) having different densities and velocities. As the absorbed energy increased

(or, in the case of our approach, the threshold fluence was lower) boiling occurred, as seen in Figure 6.14b, Area 2, and as the surface cooled, boiling marks re-solidify (Figure 6.14c, Area 2). Figure 6.14a, Area 3 depicts an agglomeration of grains on a smooth surface. The craters were similar to Figure 6.14b, Area 1; at a closer look, however, the crater edge showed signs of boiling where the laser spot reached a cluster. This led to the formation of smaller boiling centres, and this phenomenon is further examined in Figure 6.15. Several types of surfaces, rougher than the ones shown in Figure 6.14 and their corresponding craters are shown. Despite the minor changes in morphology, all craters exhibited a wavy, rougher bottom than craters in Figure 6.14. As the surface cooled, the smaller boiling centres (compared to the ones in Figure 6.14c, Area 2) remained on the crater bottom forming, when the absorbed energy was high enough, an interconnected porous structure as seen in the copper-aluminium-nickel alloy.

The micrographs of the as-deposited thin film and laser ablated craters reveal a potential cause for the observed variations in crater morphology. Isolated defects (or surface grains shown earlier) could act as centres of ignition, as they can be thermally isolated for the rest of the sample. Thus, higher local temperatures can be achieved, and boiling may occur earlier than in the surrounding area. This effect is visible when comparing the middle columns of Figure 6.14 and Figure 6.15: grains on the surface reveal smaller boiling centres compared to a smooth surface. Another potential explanation would be the shape of the scattered light at the surface [170] (i.e. deformation of the beam), which would lead to wider craters.
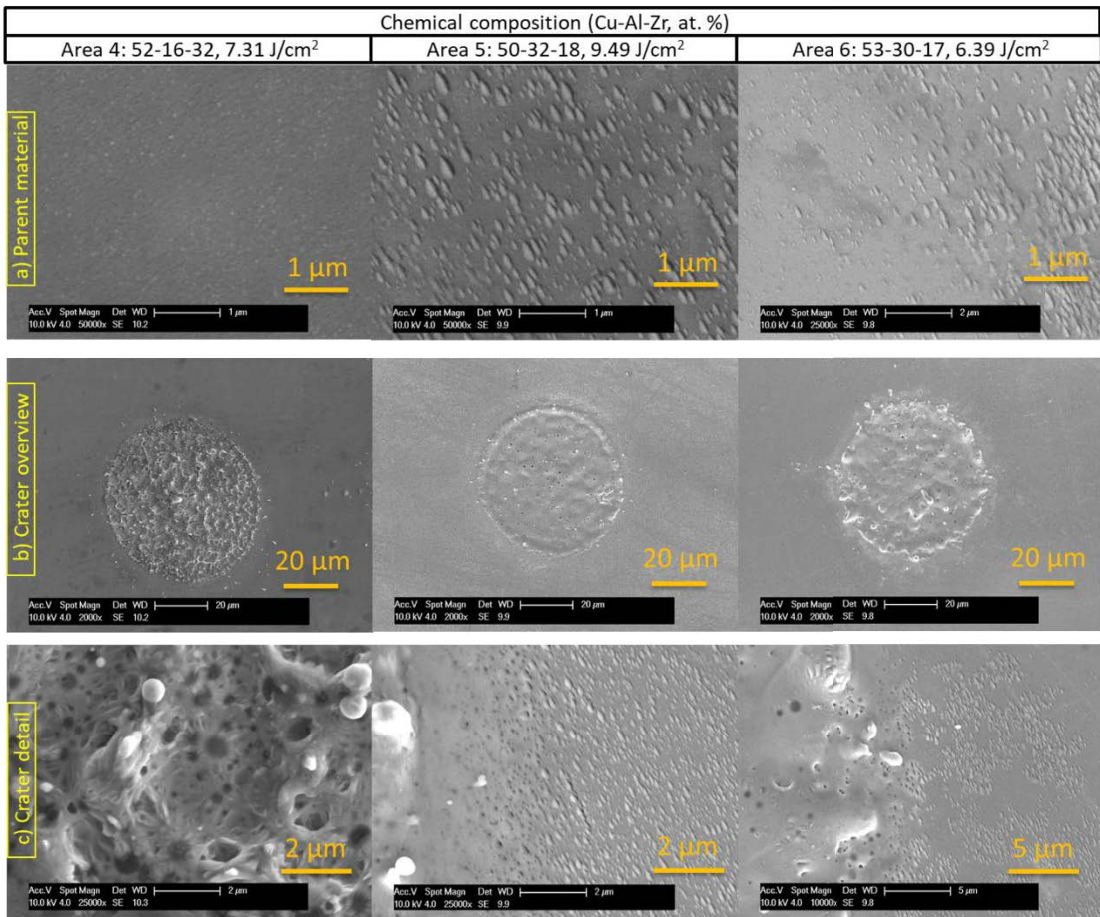
Figure 6.15 Micrographs of the as-deposited thin film (a) and the corresponding ablated craters (b) and detail (c) for three areas of the Cu-Al-Zr thin film with micro-structured surface. The chemical composition and the estimated ablation threshold based on material properties is given at the top of the image.

This phenomenon could be responsible for another finding in this work, shown in Figure 6.16. For both ternary material libraries, while most of the thin film had circular craters (corresponding to the cross-section of the Gaussian beam), a very well-defined surface morphology (i.e. well beyond the transition phase) showed elongated (i.e. elliptical) craters. It is worth noticing that craters had similar shape and morphology with the wider, shallower craters identified throughout this work.
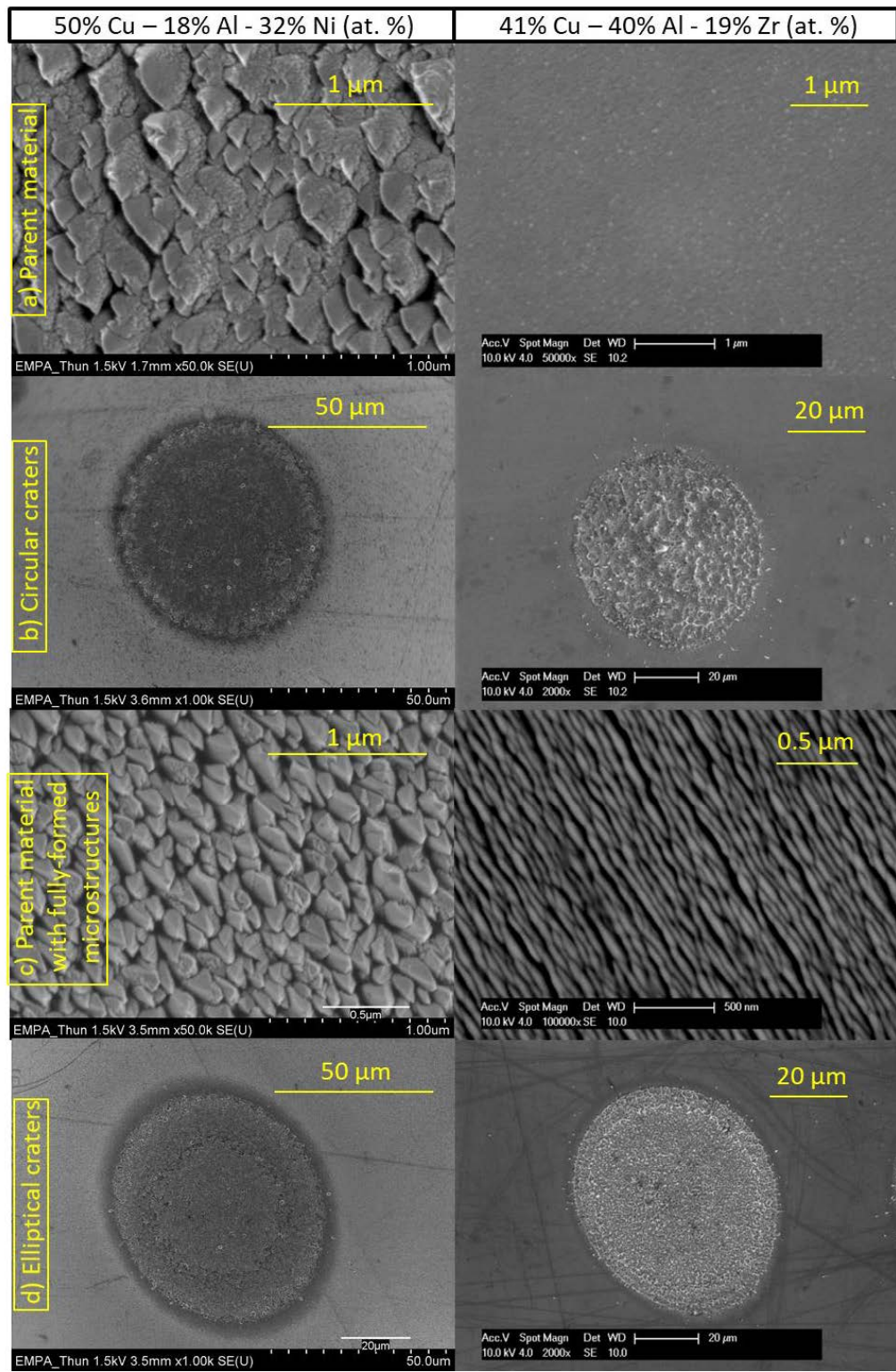
Figure 6.16 Micrographs of the as-deposited thin film (a, c) and corresponding craters (b, d) illustrating the change in crater shape in the case of both (left) Cu-Ni-Al (left) and Cu-Al-Zr (right) thin film libraries irradiated with identical laser beams.

6.4 SUMMARY

This chapter studies laser ablation of two ternary material libraries using a beam of constant parameters (30 ns, 1064 nm, 4.54 J/cm^2), and it represents, to the author's knowledge, the first work of this kind. Both samples were characterised in terms of chemical composition, thickness and reflectivity, as well as investigation of the morphological gradient. It has been noticed that an increase in the aluminium percentage led to the formation of surface structures which, with further addition of aluminium, changed their shape and size, eventually resulting in surface structure with well-defined edges.

The investigation of Cu-Al-Ni sample revealed two distinct types of craters separated by a transition area: deeper and narrower craters with a smooth bottom but a significant amount of re-deposited material on crater edge corresponded to a smooth, relatively grain-free as-deposited thin film; wider and shallower craters, with little melt re-deposited material on the edges (thus resulting in an overall larger ablated volume) were found on a rougher, micro-structured thin film. This finding is consistent with the results presented in Chapters 4 and 5.

The Cu-Al-Zr film had an overall higher reflectivity, and thus no significant material removal was observed at the same laser fluence. The absorbed energy textured the surface instead, enabling the observation of crater formation close to the ablation threshold. In terms of crater morphology, several types of craters were identified, related to both the ablation threshold of the film and to the structure of the as-deposited sample prior to ablation. Smooth irradiated areas were observed where the absorbed energy was below the boiling threshold; when the absorbed energy exceeded that threshold, two types of boiling were observed, one with larger boiling marks corresponding to a relatively smooth

as-deposited thin film, and another with smaller boiling centres, corresponding to a micro-structured thin film. As these surface features could be thermally isolated from the surrounding areas, the faster increase in temperature led to localised boiling. This phenomenon also led to the lateral expansion of craters, because the film was able to respond to heating on the exterior of the Gaussian beam, where the intensity is lower.

7 CONCLUSIONS

7.1 MAIN FINDINGS

The material response to irradiation with a laser beam has been studied by using an innovative approach, where the laser parameters were kept constant and the material was variable. The "variable" nature of the samples was achieved using thin film material libraries, i.e. exhibiting a gradual change in the chemical composition. The crater characteristics (geometry, volume and morphology) were analysed after irradiation of the samples with a beam of constant parameters (i.e. wavelength, pulse duration, energy per pulse, fluence).

The material libraries were co-sputtered using a physical vapour deposition method (magnetron sputtering) and their thickness was in the range of 0.6 µm – 1.5 µm. Nanosecond near-infrared lasers (1064 nm, 30-55 ns) were used in the experiments due to their well-established industrial use and wide availability. As ns laser ablation is dominated by thermal processes such as heat transfer, melting and evaporation, the materials used in this study (Cu, Al, Ni and later Zr) were chosen first due to their different physical properties relevant to thermal ablation and second, because of their wide range of applications, both in pure and alloyed forms.

A step-by step approach has been used. Initially, the pure Cu, Al and Ni samples were studied separately to gain insight on typical craters in metallic thin films. Subsequently, binary combinations (Cu-Ni, Ni-Al, Cu-Al) and finally ternary alloys (Cu-Ni-Al/Zr) were analysed in terms of both material characterisation (prior to irradiation) and ablation result.

Because of the considerable number of experiments required, the characterisation of both thin films and craters was conducted using time-efficient techniques which still provided the necessary information. The films were characterised in terms of reflectivity (which dictates the amount of energy received by the sample), film thickness (used as a reference for crater depth and calculation of the heat diffusion length) and the chemical composition range. Thin films and crater cross sections were studied to understand the nature and the extent of the heat affected zone, the surface and sub-surface morphology, and crater geometry and volume were analysed to quantify the material response when comparing areas of different chemical composition.

The first set of experiments was carried out on pure thin films, by using 55 ns laser pulses and varying the pulse fluence. The ablation threshold was calculated to be similar for Cu and Ni (1.77 and 1.78 J/cm^2) and slightly lower for Al (1.57 J/cm^2), but craters were obtained even below these values. Two types of craters were found. The craters in Al and Cu samples were Gaussian shaped (matching the beam spatial profile), and the Si substrate was ablated even at lower fluences. There was a high amount of recast material on the crater edges which was identified as re-solidified Si from the substrate. In contrast, clear ablation of the Ni film was achieved by single pulse processing without damage to the Si substrate, irrespective of the fluence, and little to none recast material (Ni) was observed. These craters showed a heat affected area significantly wider than the beam diameter in focus, where signs of melt with little evaporation were observed as well as peeling of the thin film at higher fluences. These differences in the ablation result were attributed to preferential horizontal heat diffusion in Ni, compared to the typical vertical one which was noticed for Al and Cu. The study of as-deposited films in terms of optical and thermal properties, surface and cross-sectional morphologies revealed that the

differences in the ablation result could be a superposition of several factors: (*i*) laser scattering at the surface by features within the range of 100 nm was observed only in Ni film; (*ii*) thermal diffusivity of the metals (which in the following experiments translated into the variation of the chemical composition) was higher for Cu (100 $\mu m^2/s$) and Al (94 $\mu m^2/s$) than Ni (19 $\mu m^2/s$); (*iii*) the magnitude of the thermal barrier between the film and the substrate (i.e. cross-sectional morphology of the films), which, calculated based on the acoustic mismatch model yielded results of 14.3, 11.8, and 15.5 $K^4/(W/cm^2)$ for Cu, Al and Ni respectively.

Additional experiments were carried out on the three binary alloys, following the same method used with the pure samples.

- The Cu-Ni binary sample was initially used to analyse how slight changes in chemical composition affect the crater geometry and morphology, because the thin film did not have a well-defined microstructure. The results revealed that, despite large variations in chemical composition, the difference in crater characteristics were negligible. All craters were Gaussian-shaped (as the spatial distribution of the laser beam) and the Si substrate was damaged irrespective of the fluence used, resulting in a significant amount of recast material on the crater edge. These results resembled the ones obtained for pure copper and aluminium samples.

- The second binary composition gradient (Ni-Al) had a morphological gradient, with surface structures gradually increasing in size and cross-sectional structures well-defined across the film. Damage to the substrate occurred irrespective of the fluence used; however it was possible to assess the effects of the surface and cross-surface film morphology. The film was peeled off, suggesting that a heat wave

was reflected from the thin film-substrate interface. Variations in crater diameter and heat affected zone suggested that a well-defined surface morphology affected the energy beam distribution at the sample surface.

- The third binary sample, Cu-Al, had well-defined microstructure across the composition gradient, like the Ni-Al binary thin film. Several areas with different chemical composition but exhibiting similar surface and cross-sectional morphology were analysed to identify how slight changes in chemical composition affect the ablation result for a microstructured film. All craters stopped at the film-substrate interface showing the effect of the thermal barrier. It was noticed that with an increase in the absorbed fluence the craters extend laterally into the heat affected zone, with only minor damage to the Si substrate. While crater morphology was similar for the entire sample, a higher crater diameter was associated with a lower melting point.

The results for the binary thin films revealed that the structure of the as-deposited thin film has a major influence on the crater shape and morphology, while the slight variations in chemical compositions were noticed in the ablation result only for "constant" film microstructure. This sample is an example of desirable outcome of thin film processing, achieved with common nanosecond infrared laser.

This work presented new insights into laser processing of ternary material libraries. Besides the composition gradient, the films also exhibited a morphological gradient, which, throughout this work, has been correlated with the presence of aluminium in the alloy. The structures in Cu-Ni-Al varied in size (from 10 nm to 500 nm) and shape, and their presence contributed to both the decrease of the sample reflectivity (at 1064 nm) and the thermal contact between the thin film and the Si substrate. Based on

the variations found in the geometrical and morphological characteristics of the craters and the sub-surface changes, as well as on the variations in the ablated volume, two regions were identified, separated by a transition area (between 27 at. % and 30 at. % Al).

- In the first region, the ablated volume was proportional to the amount of Al in the sample; the craters had a higher aspect ratio, and the sub-surface was noticeably affected by heat; a higher amount of re-deposited material compared to the second region was present, identified as re-solidified Si from the substrate. This revealed that the energy delivered by the beam was close to the ablation threshold, so less energy was available for evaporation of the molten material.

- In the second region, the craters were wider and shallower, and the sub-surface showed little heat damage; the variation of the volume was inversely proportional to the amount of aluminium, despite the threshold continuously decreasing. This behaviour was attributed to the increase in plasma density followed by partially decoupling of the workpiece from the incoming laser radiation.

The first region was similar in terms of crater morphology and geometry with pure Cu and Al, and binary Cu-Ni sample. The second region resembled craters in pure Ni and binary Ni-Al/ Cu-Al. These similarities suggested that thin film response to irradiation was more dependent on the film microstructure, which influenced heat flow in the film more than the variation in the thermal properties caused by the change in chemical composition.

To confirm that the variations in crater geometry and morphology were not typical to only Cu, Al, Ni and their corresponding alloys, a second ternary library (Cu-Al-Zr) was investigated. Similarities between the two ternary alloys were identified in terms of a microstructural gradient on the sample surface and how it affected the ablation result,

in terms of crater width and morphology of the irradiated area. Moreover, due to a higher overall reflectivity of the Cu-Al-Zr alloy, crater morphology was representative of how the boiling occurred, revealing that microstructures on the surface acted like ignition centres and could be responsible for the increase in crater width observed throughout this work. As the microstructures can be thermally isolated from the surrounding film, the local rise in the temperature would be very steep, and thus cause melting also at the outer edge of the beam. In contrast, craters corresponding to a smoother film surface were narrower, as the increase in temperature and subsequent evaporation occurred predominantly in the centre of the irradiated area.

7.2 ORIGINAL CONTRIBUTIONS

The literature review highlighted the necessity of a comprehensive study regarding the ns PLA of thin films. The currently available state-of-the-art literature appeared both scarce and scattered, with little data available to be used as a reference for researchers and engineers seeking to further understand and optimise the thermal laser ablation of thin films.

This thesis presented a systematic study of specific aspects of nanosecond pulsed laser ablation of thin (metallic) films. To achieve this, an original approach to the investigation of laser-material interaction was used. Most attempts at investigating the response of a material to laser irradiation use the laser as a variable in the process, while irradiating a target with constant chemical composition. Instead, constant laser parameters were used throughout this work, while the samples exhibited gradual changes in the chemical composition as well as film microstructure. As a reference, material response to

irradiation of three pure metal films was analysed, followed by their binary and ternary alloys in the form of material libraries.

This approach was used to investigate several key issues regarding nanosecond pulsed laser ablation of thin metallic films:

1) While thin film laser patterning has been previously achieved using sub-picosecond or nanosecond lasers with a top-hat spatial beam profile, the results presented in this work revealed processing conditions (a combination between thin film characteristics and laser parameters) where thin film ablation without damaging the substrate could be achieved.

2) As the name suggests, material libraries cover a wide range of compositions, so it would be useful to estimate ablation threshold for these materials without performing the typical ablation threshold tests. An existing model (which uses reflectivity, film thickness and thermal properties of the material) was adapted for alloys and used in this study. This provided an estimate for the ablation threshold by considering the material properties, but disregarding morphology-induced variations.

3) As a thin film material library may exhibit a morphology gradient in addition to the compositional one, separation between the influence of the chemical composition and the influence of thin film surface and cross-sectional morphology were first assessed separately. As the Cu-Ni sample showed no strong variations in surface and cross-sectional morphology. The influence of surface and cross-sectional thin film morphology was discussed separately, depending whether the thin film had a well-defined microstructure, when investigating the Ni-Al and Cu-Al alloys.

4) A ternary Cu-Ni-Al alloy was analysed to observe the superposition of the effects named previously, while a Cu-Al-Zr one was used to establish whether the material response of combinatorial libraries studied in this work were material specific.

7.3 LIMITATIONS AND FURTHER WORK

Several aspects are worth considering regarding the work presented in this thesis. Overall, the approach used was meant to achieve an in-depth physical understanding while maintaining a more practical engineering approach. However, due to the novelty of the topic, limited resources were available in literature which means there are various aspects to be pursued further:

1) Optimisation of material libraries and study of ultra-thin films

Variation in thickness of the material library is a consequence of the synthesis method. In laser ablation of thin films, the threshold increases linearly with the sample thickness, until the thickness reaches the heat diffusion length. It would thus be useful to obtain samples of different compositions, but with a constant thickness. In addition, ultra-thin films (i.e. below tens of nm) may respond differently to ablation, so films of various thicknesses could be investigated.

2) Detailed characterisation of thin films

For the study of material libraries characterisation of the film is needed, and that may prove to be challenging, as thin films require special characterisation techniques compared to bulk materials. In this work suitable results were obtained by measuring the thin film thickness and reflectivity and estimating the thermal properties. However, sometimes more detailed characterisation may be needed, such as thermal diffusivity.

3) Investigation of dynamic ablation using time-resolved techniques

An investigation targeting the real-time change in crater shape with respect to the beam profile (i.e. crater widening and, in certain cases, deformation) would be of interest, possibly using time-resolved measurements of, for example, the local increase in temperature which comes from the presence of micro-structures on the surface. Moreover, surface defects, impurities and peak-like structures lead to air breakdown or laser produced plasma even before the laser fluence reaches the vaporisation threshold of the material. Plasma ignition is significant in the case of metals where the ablation threshold and plasma formation threshold are similar, so a time-resolved measurement of plasma ignition and expansion would be worth pursuing.

4) Implementation of the presented technique discovery of new materials

A potential application of this original approach could be the discovery of new easy-to-process materials. As material libraries are already used to investigate composition-property relationship, if more than one chemical compositions exhibit the desired property, the choice of composition could be given by its machining capabilities.

5) Upscaling the laser processing

A further step to be taken from an application point of view would be to upscale the process, i.e. to laser-machine trenches and surface patterns, to obtain the desired surface functionality (for example the porous craters could be promising hydrophobic surfaces).

LIST OF REFERENCES

[1]   R. Potyrailo, K. Rajan, K. Stoewe, I. Takeuchi, B. Chisholm, H. Lam, Combinatorial and high-throughput screening of materials libraries: review of state of the art., ACS Comb. Sci. 13 (2011) 579–633.

[2]   T. Gebhardt, D. Music, T. Takahashi, J.M. Schneider, Combinatorial thin film materials science: From alloy discovery and optimization to alloy design, Thin Solid Films. 520 (2012) 5491–5499.

[3]   N.C. Woo, B.G. Ng, R.B. van Dover, High-throughput combinatorial study of local stress in thin film composition spreads., Rev. Sci. Instrum. 78 (2007) 072208.

[4]   J. Zhao, Combinatorial approaches as effective tools in the study of phase diagrams and composition–structure–property relationships, Prog. Mater. Sci. 51 (2006) 557–631.

[5]   R. Hu, P. Nash, Review: Experimental enthalpies of formation of compounds in Al-Ni-X systems, J. Mater. Sci. 41 (2006) 631–641.

[6]   S.S. Ray, K. Okamoto, M. Okamoto, Structure-property relationship in biodegradable poly(butylene succinate)/layered silicate nanocomposites, Macromolecules. 36 (2003) 2355–2367.

[7]   N.S. Barekar, S. Pauly, R.B. Kumar, U. Kühn, B.K. Dhindaw, J. Eckert, Structure–property relations in bulk metallic Cu–Zr–Al alloys, Mater. Sci. Eng. A. 527 (2010) 5867–5872.

[8]   L. Garwin, T. Lincoln, A Century of Nature, University of Chicago Press, 2003.

[9]   T.H. Maiman, Stimulated optical radiation in ruby, Nature. 187 (1960) 493–494.

[10]   M. von Allmen, A. Blatter, Laser-beam interactions with materials: Physical principles and applications, 2nd ed., Springer Berlin Heidelberg, 1995.

[11]   A. Gillner, Laser micro processing: Recent development and future prospectives, Laser Tech. J. 5 (2007) 27–30.

[12]   K. Kincade, A. Nogee, G. Overton, D. Belforte, C. Holton, Annual Laser Market Review & Forecast: Lasers enabling lasers, Laser Focus World. (2018)http://www.laserfocusworld.com/articles/print/volume-54/issue-01/features/annual-laser-market-review-forecast-lasers-enabling-lasers.html

(accessed February 4, 2018).

[13]   J. Meijer, Laser beam machining (LBM), state of the art and new opportunities, J. Mater. Process. Technol. 149 (2004) 2–17.

[14]   M.D. Shirk, P.A. Molian, A review of ultrashort pulsed laser ablation of materials, J. Laser Appl. 10 (1998) 18.

[15]   C.P. Grigoropoulos, Transport in Laser Microfabrication: Fundamentals and Applications, Cambridge University Press, New York, 2009.

[16]   P. Schaaf, ed., Laser Processing of Materials: Fundamentals, Applications and Developments, Springer, New York, 2010.

[17]   S. Fähler, H.-U. Krebs, Calculations and experiments of material removal and kinetic energy during pulsed laser ablation of metals, Appl. Surf. Sci. 96–98 (1996) 61–65.

[18]   A. Mele, A. Giardini Guidoni, R. Kelly, C. Flamini, S. Orlando, Laser ablation of metals: Analysis of surface-heating and plume-expansion experiments, Appl. Surf. Sci. 109–110 (1997) 584–590.

[19]   J.G. Lunney, R. Jordan, Pulsed laser ablation of metals, Appl. Surf. Sci. (1998) 941–946.

[20]   N.M. Bulgakova, A. V Bulgakov, I.M. Bourakov, N.A. Bulgakova, Pulsed laser ablation of solids and critical phenomena, 198 (2002) 198–201.

[21]   P. Lorazo, L. Lewis, M. Meunier, Short-Pulse Laser Ablation of Solids: From Phase Explosion to Fragmentation, Phys. Rev. Lett. 91 (2003) 225502.

[22]   C. Cheng, X. Xu, Mechanisms of decomposition of metal during femtosecond laser ablation, Phys. Rev. B. 72 (2005) 165415.

[23]   V. Alexiades, D. Autrique, Enthalpy model for heating, melting, and vaporization in laser ablation, 19 (2010) 1–13.

[24]   D. von der Linde, K. Sokolowski-Tinten, The physical mechanisms of short-pulse laser ablation, Appl. Surf. Sci. 154–155 (2000) 1–10.

[25]   K. Sokolowski-Tinten, J. Bialkowski, A. Cavalleri, D. von der Linde, A. Oparin, J. Meyer-ter-Vehn, S. Anisimov, Transient States of Matter during Short Pulse Laser Ablation, Phys. Rev. Lett. 81 (1998) 224–227.

[26]   J.M. Fishburn, M.J. Withford, D.W. Coutts, J.A. Piper, Study of the fluence dependent interplay between laser induced material removal mechanisms in

metals: Vaporization, melt displacement and melt ejection, Appl. Surf. Sci. 252 (2006) 5182–5188.

[27] A. V. Pakhomov, M.S. Thompson, D.A. Gregory, Laser-induced phase explosions in lead, tin and other elements : microsecond regime and UV-emission, J. Phys. D. Appl. Phys. 36 (2003) 2067–2075.

[28] X. Xu, K.H. Song, Phase change phenomena during high power laser-materials interaction, Mater. Sci. Eng. A. 292 (2000) 162–168.

[29] X. Xu, Phase explosion and its time lag in nanosecond laser ablation, Appl. Surf. Sci. 197–198 (2002) 61–66.

[30] L.M. Cabalin, J.J. Laserna, Experimental determination of laser induced breakdown thresholds of metals under nanosecond Q-switched laser operation, Spectrochim. Acta Part B At. Spectrosc. 53 (1998) 723–730.

[31] B. Salle, C. Chaleard, V. Detalle, J.L. Lacour, P. Mauchien, C. Nouvellon, A. Semerok, Laser ablation efficiency of metal samples with UV laser nanosecond pulses, Appl. Surf. Sci. 138 (1999) 302–305.

[32] I. Vladoiu, M. Stafe, C. Negutu, I.M. Popescu, The dependence of the ablation rate of metals on nanosecond laser fluence and wavelength, J. Optoelectron. Adv. Mater. 10 (2008) 3177–3181.

[33] M. Stafe, I. Vladoiu, C. Negutu, I.M. Popescu, Experimental Investigation of the Nanosecond Laser Ablation Rate of Aluminium, Rom. Reports Phys. 60 (2008) 789–796.

[34] S.N. Aqida, D. Brabazon, S. Naher, Z. Kovacs, D.J. Browne, Laser micro-processing of amorphous and partially crystalline Cu45Zr48Al7 alloy, Appl. Phys. A Mater. Sci. Process. 101 (2010) 357–360.

[35] D.J. Jorgensen, M.S. Titus, T.M. Pollock, Femtosecond laser ablation and nanoparticle formation in intermetallic NiAl, Appl. Surf. Sci. 353 (2015) 700–707.

[36] O.A. Bulgakova, N.M. Bulgakova, V.P. Zhukov, A model of nanosecond laser ablation of compound semiconductors accounting for non-congruent vaporization, Appl. Phys. A Mater. Sci. Process. 101 (2010) 53–59.

[37] S.K. Sundaram, E. Mazur, Inducing and probing non-thermal transitions in semiconductors using femtosecond laser pulses, Nat. Mater. 1 (2002) 217–224.

[38] S. Rung, A. Christiansen, R. Hellmann, Influence of film thickness on laser

ablation threshold of transparent conducting oxide thin-films, Appl. Surf. Sci. 305 (2014) 347–351.

[39] K.-H. Leitz, B. Redlingshöfer, Y. Reg, A. Otto, M. Schmidt, Metal ablation with short and ultrashort laser pulses, in: Phys. Procedia, 2011: pp. 230–238.

[40] A.Y. Vorobyev, V.M. Kuzmichev, N.G. Kokody, P. Kohns, J. Dai, C. Guo, Residual thermal effects in Al following single ns- and fs-laser pulse ablation, Appl. Phys. A Mater. Sci. Process. 82 (2006) 357–362.

[41] L. Tunna, A. Kearns, W. O'Neill, C.. Sutcliffe, Micromachining of copper using Nd:YAG laser radiation at 1064, 532, and 355 nm wavelengths, Opt. Laser Technol. 33 (2001) 135–143.

[42] J.-F.Y. Gravel, D. Boudreau, Study by focused shadowgraphy of the effect of laser irradiance on laser-induced plasma formation and ablation rate in various gases, Spectrochim. Acta Part B At. Spectrosc. 64 (2009) 56–66.

[43] D.N. Patel, R.P. Singh, R.K. Thareja, Craters and nanostructures with laser ablation of metal/metal alloy in air and liquid, Appl. Surf. Sci. 288 (2014) 550–557.

[44] X. Li, W. Wei, J. Wu, S. Jia, A. Qiu, The Influence of spot size on the expansion dynamics of nanosecond-laser-produced copper plasmas in atmosphere, J. Appl. Phys. 113 (2013).

[45] M.H. Mahdieh, M. Nikbakht, Z. Eghlimi Moghadam, M. Sobhani, Crater geometry characterization of Al targets irradiated by single pulse and pulse trains of Nd:YAG laser in ambient air and water, Appl. Surf. Sci. 256 (2010) 1778–1783.

[46] O. Svelto, Principles of Lasers, 5th ed., Springer, 2010.

[47] A.M. Prokhorov, Molecular amplifier and generator for submillimeter waves, Sov. Phys.-JETP. 7 (1958) 1140–1141.

[48] A.L. Schawlow, C.H. Townes, Infrared and optical masers, Phys. Rev. 112 (1958) 1940–1949.

[49] N.G. Basov, O.N. Krokhin, Y.M. Popov, Generation, amplification, and detection of infrared and optical radiation by quantum-mechanical systems, Sov. Phys. Usp. 3 (1961) 702–726.

[50] The Nobel Prize in Physics 1964, (n.d.)https://www.nobelprize.org/nobel_prizes/physics/laureates/1964/ (accessed

May 13, 2017).

[51]   W. Steen, J. Mazumder, Background to Laser Design and General Applications, in: Laser Mater. Process., 2010.

[52]   R.N. Hall, G.E. Fenner, J.D. Kingsley, T.J. Soltys, R.O. Carlson, Coherent light emission from GaAs junctions, Phys. Rev. Lett. 9 (1962) 366–368.

[53]   J.E. Geusic, H.M. Marcos, L.G. Van Uitert, Laser oscillations in nd-doped yttrium aluminum, yttrium gallium and gadolinium garnets, Appl. Phys. Lett. 4 (1964) 182–184.

[54]   F.P. Schäfer, W. Schmidt, J. Volze, Organic dye solution laser, Appl. Phys. Lett. 9 (1966) 306–309.

[55]   A. Javan, W.R. Bennett, D.R. Herriott, Population inversion and continuous optical maser oscillation in a gas discharge containing a He-Ne mixture, Phys. Rev. Lett. 6 (1961) 106–110.

[56]   C.K.N. Patel, Continuous-wave laser action on vibrational-rotational transition of CO_2, Phys. Rev. 136 (1964) A1187–A1193.

[57]   T. Hansch, M. Pernier, A. Schawlow, Laser Action of Dyes in Gelatin, IEEE J. Quantum Electron. (1971) 45–46.

[58]   W. Koechner, Solid-State Laser Engineering, 6th ed., Springer, 2006.

[59]   C. Jauregui, J. Limpert, A. Tünnermann, High-power fibre lasers, Nat. Photonics. 7 (2013) 861–867.

[60]   A. Einstein, On the quantum mechanics of radiation, Phys. Zeitschrift. 18 (1917) 121–128.

[61]   A.D. Rakic, Algorithm for the determination of intrinsic optical constants of metal films: application to aluminum, Appl. Opt. 34 (1995) 4755–4767.

[62]   P.B. Johnson, R.W. Christy, Optical Constants of the Noble Metals, Phys. Rev. B. 6 (1972) 4370–4379.

[63]   P.B. Johnson, R.W. Christy, Optical constants of transition metals, Phys. Rev. B. 9 (1974) 5056–5070.

[64]   M.S. Qaisar, G.J. Pert, Laser ablation of Mg, Cu, and Pb using infrared and ultraviolet low-fluence lasers, J. Appl. Phys. 94 (2003) 1468–1477.

[65]   D. Bergström, J. Powell, A. Kaplan, The absorptance of steels to Nd:YAG and Nd:YLF laser light at room temperature, Appl. Surf. Sci. 253 (2007) 5017–5028.

[66] M. Muthusamy, S. Muthukumaran, M. Ashokkumar, Composition dependent optical, structural and photoluminescence behaviour of CdS:Al thin films by chemical bath deposition method, Ceram. Int. 40 (2014) 10657–10666.

[67] N.R. Murphy, J.T. Grant, L. Sun, J.G. Jones, R. Jakubiak, V. Shutthanandan, C.V. Ramana, Correlation between optical properties and chemical composition of sputter-deposited germanium oxide (GeOx) films, Opt. Mater. (Amst). 36 (2014) 1177–1182.

[68] E.R. Shaaban, M. Abdel-Rahman, E.S. Yousef, M.T. Dessouky, Compositional dependence of the optical properties of amorphous antimony selenide thin films using transmission measurements, Thin Solid Films. 515 (2007) 3810–3815.

[69] T. Shiraishi, R.J.D. Tilley, An estimation of the reflectivity of some monophasic binary gold alloys, Gold Bull. 47 (2013) 75–82.

[70] S.J. Wilson, M.C. Hutley, The optical properties of "moth eye" antireflection surfaces, Opt. Acta Int. J. Opt. 29 (1982) 993–1009.

[71] H.K. Raut, V.A. Ganesh, A.S. Nair, S. Ramakrishna, Anti-reflective coatings: A critical, in-depth review, Energy Environ. Sci. 4 (2011) 3779.

[72] A. Poruba, A. Fejfar, Z. Remeš, J. Špringer, M. Vaněček, J. Kočka, J. Meier, P. Torres, A. Shah, Optical absorption and light scattering in microcrystalline silicon thin films and solar cells, J. Appl. Phys. 88 (2000) 148–160.

[73] A.M. Rubenchik, S.S. Wu, V.K. Kanz, M.M. LeBlanc, W.H. Lowdermilk, M.D. Rotter, J.R. Stanley, Temperature-dependent 780-nm laser absorption by engineering grade aluminum, titanium, and steel alloy surfaces, Opt. Eng. 53 (2014) 122506.

[74] B.S. Yilbas, K. Danisman, Z. Yilbas, Measurement of temperature-dependent reflectivity of Cu and Al in the range 30-1000 degrees C, Meas. Sci. Technol. 2 (1991) 668–674.

[75] O. Benavides, O. Lebedeva, V. Golikov, Reflection of nanosecond Nd:YAG laser pulses in ablation of metals., Opt. Express. 19 (2011) 21842–8.

[76] O. Benavides, L. de la C. May, A.F. Gil, A comparative study on reflection of nanosecond Nd-YAG laser pulses in ablation of metals in air and in vacuum, Opt. Soc. Am. 21 (2013) 13068–13074.

[77] A.Y. Vorobyev, Reflection of pulsed ruby laser radiation by a copper target in air

and in vacuum, Sov. J. Quantum Electron. 15 (1985) 490–493.

[78] I.L. Hao, H. Chen, W. Zhang, Y.L. Yao, H. Chen, W. Zhang, Time scale effects in laser material removal: a review, Int. J. Adv. Manuf. Technol. 26 (2005) 598–608.

[79] D. Bleiner, A. Bogaerts, Multiplicity and contiguity of ablation mechanisms in laser-assisted analytical micro-sampling, Spectrochim. Acta Part B At. Spectrosc. 61 (2006) 421–432.

[80] M.S. Brown, C.B. Arnold, Laser Precision Microfabrication, in: K. Sugioka, M. Meunier, A. Piqué (Eds.), Springer Berlin Heidelberg, Berlin, Heidelberg, 2010: pp. 91–120.

[81] J.F. Ready, Effects of High-Power Laser Radiation, Academic Press, New York, 1971.

[82] M. Stafe, C. Negutu, N.N. Puscas, I.M. Popescu, Pulsed laser ablation of solids, Rom. Reports Phys. 62 (2010) 758–770.

[83] S. Amoruso, R. Bruzzese, N. Spinelli, R. Velotta, Characterization of laser-ablation plasmas, J. Phys. B At. Mol. Phys. 32 (1999) 131–172.

[84] V. Semak, A. Matsunawa, The role of recoil pressure in energy balance during laser materials processing, J. Phys. D. Appl. Phys. 30 (1997) 2541–2552.

[85] J.M. Vadillo, J.M. Fernández Romero, C. Rodríguez, J.J. Laserna, Effect of plasma shielding on laser ablation rate of pure metals at reduced pressure, Surf. Interface Anal. 27 (1999) 1009–1015.

[86] J. Chang, B.E. Warner, Laser-plasma interaction during visible-laser ablation of methods, Appl. Phys. Lett. 69 (1996) 473.

[87] A.Y. Vorobyev, C. Guo, Residual thermal effects in laser ablation of metals, J. Phys. Conf. Ser. 59 (2007) 418–423.

[88] W.M. Wang, Z.M. Sheng, J. Zhang, A model for the efficient coupling between intense lasers and subwavelength grating targets, Phys. Plasmas. 15 (2008) 23–26.

[89] V.N. Lednev, S.M. Pershin, A.A. Ionin, S.I. Kudryashov, S. V Makarov, A.E. Ligachev, A.A. Rudenko, R.A. Chmelnitsky, A.F. Bunkin, Laser ablation of polished and nanostructured titanium surfaces by nanosecond laser pulses, Spectrochim. Acta - Part B At. Spectrosc. 88 (2013) 15–19.

[90] K. Mikami, S. Motokoshi, M. Fujita, T. Somekawa, T. Jitsuno, K.A. Tanaka, Temperature dependences of laser induced plasma thresholds and periodic

structures by nanosecond infrared laser for copper, iron, and chrome, Appl. Phys. Express. 5 (2012) 3–6.

[91] H.A. Lutey, An improved model for nanosecond pulsed laser ablation of metals, J. Appl. Phys. 114 (2013) 083108.

[92] A. Miotello, R. Kelly, Laser-induced phase explosion: New physical problems when a condensed phase approaches the thermodynamic critical temperature, Appl. Phys. A Mater. Sci. Process. 69 (1999) 67–73.

[93] C. Porneala, D.A. Willis, Observation of nanosecond laser-induced phase explosion in aluminum, Appl. Phys. Lett. 89 (2006) 211121.

[94] R. Schaeffer, Commercially available ultrafast-pulse lasers: An update, Ind. Laser Solut. (2014)https://www.industrial-lasers.com/articles/print/volume-29/issue-6/features/commercially-available-ultrafast-pulse-lasers-an-update.html (accessed February 7, 2018).

[95] A. Nogee, Ultrafast laser market—the battle of value vs. cost, Laser Focus World. (2015)http://www.laserfocusworld.com/articles/2015/05/ultrafast-laser-market-the-battle-of-value-vs-cost.html (accessed February 7, 2018).

[96] A. Nakajima, K. Hashimoto, T. Watanabe, Transparent superhydrophobic thin films with self-cleaning properties, Langmuir. 16 (2000) 7044–7047.

[97] X. Zhang, J. He, Antifogging antireflective thin films: does the antifogging layer have to be the outmost layer?, Chem. Commun. 51 (2015) 12661–12664.

[98] K.L. Chopra, P.D. Paulson, V. Dutta, Thin-film solar cells: an overview, Prog. Photovoltaics Res. Appl. 12 (2004) 69–92.

[99] A.H.S. Jones, D. Camino, D.G. Teer, J. Jiang, Novel high wear resistant diamond-like carbon coatings deposited by magnetron sputtering of carbon targets, Proc. Inst. Mech. Eng. Part J J. Eng. Tribol. 212 (1998) 301–306.

[100] T. Yamamura, M. Kitamura, K. Kuribayashi, Y. Arakawa, S. Takeuchi, Flexible organic leds with parylene thin films for biological implants, 2007 IEEE 20th Int. Conf. Micro Electro Mech. Syst. (2007) 2007–2010.

[101] Y. Fu, H. Du, W. Huang, S. Zhang, M. Hu, TiNi-based thin films in MEMS applications: a review, Sensors Actuators A Phys. 112 (2004) 395–408.

[102] C.-B. Eom, S. Trolier-McKinstry, Thin-film piezoelectric MEMS, MRS Bull. 37 (2012) 1007–1017.

[103] J. Hermann, M. Benfarah, G. Coustillier, S. Bruneau, E. Axente, J.-F. Guillemoles, M. Sentis, P. Alloncle, T. Itina, Selective ablation of thin films with short and ultrashort laser pulses, Appl. Surf. Sci. 252 (2006) 4814–4818.

[104] J. Kim, S. Na, Metal thin film ablation with femtosecond pulsed laser, Opt. Laser Technol. 39 (2007) 1443–1448.

[105] S. Zoppel, H. Huber, G.A. Reider, Selective ablation of thin Mo and TCO films with femtosecond laser pulses for structuring thin film solar cells, Appl. Phys. A Mater. Sci. Process. 89 (2007) 161–163.

[106] G. Heise, M. Domke, J. Konrad, S. Sarrach, J. Sotrop, H.P. Huber, Laser lift-off initiated by direct induced ablation of different metal thin films with ultra-short laser pulses, J. Phys. D. Appl. Phys. 45 (2012) 315303.

[107] G. Heise, M. Englmaier, C. Hellwig, T. Kuznicki, S. Sarrach, H.P. Huber, Laser ablation of thin molybdenum films on transparent substrates at low fluences, Appl. Phys. A Mater. Sci. Process. 102 (2011) 173–178.

[108] M.F. Chen, Y.P. Chen, W.T. Hsiao, Z.P. Gu, Laser direct write patterning technique of indium tin oxide film, Thin Solid Films. 515 (2007) 8515–8518.

[109] M. Domke, L. Nobile, S. Rapp, S. Eiselen, J. Sotrop, H.P. Huber, M. Schmidt, Understanding thin film laser ablation: The role of the effective penetration depth and the film thickness, Phys. Procedia. 56 (2014) 1007–1014.

[110] D.J. Hwang, A. Chimmalgi, C.P. Grigoropoulos, Ablation of thin metal films by short-pulsed lasers coupled through near-field scanning optical microscopy probes, J. Appl. Phys. 99 (2006) 044905.

[111] B.N. Chichkov, C. Momma, S. Nolte, F. von Alvensleben, A. Tünnermann, Femtosecond, picosecond and nanosecond laser ablation of solids, Appl. Phys. A Mater. Sci. Process. 63 (1996) 109–115.

[112] H.A. Lutey, M. Sozzi, S. Carmignato, S. Selleri, A. Cucinotta, P.G. Molari, Nanosecond and sub-nanosecond pulsed laser ablation of thin single and multi-layer packaging films, Appl. Surf. Sci. 285 (2013) 300–308.

[113] E. Matthias, J. Siegel, S. Petzoldt, M. Reichling, H. Skurk, O.W. Kading, E. Neske, In-situ investigation of laser ablation of thin films, Thin Solid Films. 254 (1995) 139–146.

[114] S.M. Metev, V.P. Veiko, Laser-Assisted Microtechnology, 2nd ed., Springer,

1998.

[115] E. Matthias, M. Reichling, J. Siegel, O.W. Kading, S. Petzoldt, H. Skurk, P. Bizenberger, E. Neske, The influence of thermal diffusion on laser ablation of metal films, Appl. Phys. A Mater. Sci. Process. 58 (1994) 129–136.

[116] H. Domer, O. Bostanjoglo, Laser ablation of thin films with very high induced stresses, J. Appl. Phys. 91 (2002) 5462–5467.

[117] M. Samuelsson, D. Lundin, J. Jensen, M.A. Raadu, J.T. Gudmundsson, U. Helmersson, On the film density using high power impulse magnetron sputtering, Surf. Coatings Technol. 205 (2010) 591–596.

[118] H.K. Pulker, Coatings on Glass, Elsevier, 1999.

[119] M. Ohring, Film Formation and Structure, in: Mater. Sci. Thin Film., 2nd ed., Academic Press, San Diego, 1992: pp. 195–247.

[120] M. Ohring, Electrical and Magnetic Properties of Thin Films, in: Mater. Sci. Thin Film., 2nd ed., Academic Press, San Diego, 1992: pp. 451–506.

[121] D. Shelton, Optical properties of metallic films, in: Met. Film. Electron. Opt. Magn. Appl., Woodhead Publishing Limited, Cambridge, 2014: pp. 547–589.

[122] M. Ohring, Optical Properties of Thin Films, in: Mater. Sci. Thin Film., 2nd ed., Academic Press, San Diego, 1992: pp. 507–545.

[123] D.G. Stavenga, S. Foletti, G. Palasantzas, K. Arikawa, Light on the moth-eye corneal nipple array of butterflies., Proc. Biol. Sci. 273 (2006) 661–667.

[124] S. Takemura, D.G. Stavenga, K. Arikawa, Absence of eye shine and tapetum in the heterogeneous eye of Anthocharis butterflies (Pieridae)., J. Exp. Biol. 210 (2007) 3075–3081.

[125] P. Schelling, Thermal properties of metallic films, in: Met. Film. Electron. Opt. Magn. Appl., 2014: pp. 590–619.

[126] H. Kaya, Dependence of electrical resistivity on temperature and composition of Al–Cu alloys, Mater. Res. Innov. 16 (2012) 224–229.

[127] G. Langer, J. Hartmann, M. Reichling, Thermal conductivity of thin metallic films measured by photothermal profile analysis, Rev. Sci. Instrum. 68 (1997) 1510.

[128] E.T. Swartz, R.O. Pohl, Thermal boundary resistance, Rev. Mod. Phys. 61 (1989) 605–668.

[129] B.S. Shin, J.Y. Oh, H. Sohn, Theoretical and experimental investigations into laser

ablation of polyimide and copper films with 355-nm Nd:YVO4 laser, J. Mater. Process. Technol. 187–188 (2007) 260–263.

[130] A. Schoonderbeek, Laser Processing of Thin Films for Photovoltaic Applications, J. Laser Micro/Nanoengineering. 5 (2010) 248–255.

[131] S. Rung, M. Rexhepi, C. Bischoff, R. Hellmann, Laserscribing of thin films using top-hat laser beam profiles, J. Laser Micro Nanoeng. 8 (2013) 309–314.

[132] C. Bischoff, R. Hellmann, S. Rung, Efficient micromachining of thin films with nanosecond lasers, Laser Tech. J. 49 (2012) 15–20.

[133] D. V. Ta, A. Dunn, T.J. Wasley, R.W. Kay, J. Stringer, P.J. Smith, C. Connaughton, J.D. Shephard, Nanosecond laser textured superhydrophobic metallic surfaces and their chemical sensing applications, Appl. Surf. Sci. 357 (2015) 248–254.

[134] D. Patil, S. Aravindan, M. Kaushal Wasson, P. Vivekanandan, P. V. Rao, Fast Fabrication of Superhydrophobic Titanium Alloy as Antibacterial Surface Using Nanosecond Laser Texturing, J. Micro Nano-Manufacturing. 6 (2017) 011002.

[135] S.H. Ko, H. Pan, D.J. Hwang, J. Chung, S. Ryu, C.P. Grigoropoulos, D. Poulikakos, High resolution selective multilayer laser processing by nanosecond laser ablation of metal nanoparticle films, J. Appl. Phys. 102 (2007) 1–9.

[136] C. Korner, R. Mayerhofer, M. Hartmann, H.W. Bergmann, Physical and material aspects in using visible laser pulses of nanosecond duration for ablation, Appl. Phys. A Mater. Sci. Process. 63 (1996) 123–131.

[137] D. Bigoni, M. Milani, R. Jafer, C. Liberatore, S. Tarazi, L. Antonelli, D. Batani, Influence of mechanical and thermal material properties on laser-produced crater-morphology and their study by focused ion beam & scanning electron microscope imaging, J. Laser Micro/Nanoengineering. 5 (2010) 169–174.

[138] G4 Pulsed Fibre Laser Product Manual, SPI Lasers UK Ltd, 2012.

[139] Pulsed Fibre Lasers, SPI Lasers UK Ltd, n.d.

[140] FISCHERSCOPE ® X-RAY XDV ® - µ X-Ray Fluorescence Measuring Instrument with a Polycapillary X-Ray Optics for Automated Measurements and Analyses of Coating Thicknesses and Compositions on Very Small Components and Structures, (n.d.).

[141] H. Fischer, X-Ray Fluorescence Spectroscopy (XRF) – Basics, (n.d.)http://xrf-

spectroscopy.com/ (accessed April 17, 2017).

[142]   Energy   dispersive   X-ray   fluorescence   (EDXRF),
         (n.d.)https://www.malvernpanalytical.com/en/products/technology/x-ray-
         fluorescence/energy-dispersive-x-ray-fluorescence (accessed May 22, 2018).

[143]   XL30 ESEM FEG Scanning Electron Microscpe, (2000).

[144]   DekTak3 ST Surface Profile Measuring System, (n.d.).

[145]   F.-Y. Zhu, Q.-Q. Wang, X.-S. Zhang, W. Hu, X. Zhao, H.-X. Zhang, 3D
         nanostructure reconstruction based on the SEM imaging principle, and
         applications, Nanotechnology. 25 (2014) 185705–10.

[146]   C.A. Volkert, A.M. Minor, Focused Ion Beam Microscopy and Micromachining,
         MRS Bull. 32 (2007) 389–399.

[147]   R. Danzl, F. Helmli, S. Scherer, Focus Variation – a Robust Technology for High
         Resolution Optical 3D Surface Metrology, Strojniški Vestn. – J. Mech. Eng. 57
         (2011) 245–256.

[148]   Alicona - IF-LaboratoryMeasurementModule, (2013).

[149]   C.P. Kothandaraman, S. Subramanyan, Heat and Mass Transfer Data Book, 5th
         ed., New Age International, New Delhi, 2004.

[150]   J.A. Dean, Lange's Handbook of Chemistry, 15th ed., McGraw-Hill, Inc., New
         York, 1998.

[151]   C.L. Yaws, Enthalpy of Fusion – Inorganic Compounds, in: Thermophys. Prop.
         Chem. Hydrocarb., 2nd ed., Elsevier Inc., 2014: pp. 676–680.

[152]   P. Nath, K.L. Chopra, Thermal conductivity of copper films, Thin Solid Films. 20
         (1974) 53–62.

[153]   Y. Volkov, L. Palatnik, A. Pugachev, Investigation of the thermal properties of
         thin aluminum films, Zh. Eksp. Teor. Fiz. 43 (1976) 1171–1174.

[154]   X. Bai, Q. Ma, M. Perrier, V. Motto-Ros, D. Sabourdy, L. Nguyen, A. Jalocha, J.
         Yu, Experimental study of laser-induced plasma: Influence of laser fluence and
         pulse duration, Spectrochim. Acta - Part B At. Spectrosc. 87 (2013) 27–35.

[155]   J.S. Custer, M.O. Thompson, D.C. Jacobson, J.M. Poate, S. Roorda, W.C. Sinke,
         F. Spaepen, Density of amorphous Si, Appl. Phys. Lett. 64 (1994) 437–439.

[156]   V.A. Sterligov, Y. V Subbota, Y.M. Shirshov, L.P. Pochekaylova, E.F. Venger, R.
         V Konakova, I.Y. Ilyin, Elastic laser light scattering by GaAs surfaces, Appl. Opt.

38 (1999) 2666–76.

[157] N. Shen, J.D. Bude, C.W. Carr, Model laser damage precursors for high quality optical materials, Opt. Express. 22 (2014) 3393.

[158] John A. Thornton, Structure-Zone Models Of Thin Films, Proc. SPIE 0821, Model. Opt. Thin Film. 95 (1988).

[159] R.E. Taylor, Things Mother Never Taught Me (about Thermophysical Properties of Solids), in: C.J. Cremer, H.A. Fine (Eds.), Therm. Conduct. 21, Plenum Press, 1990: pp. 41–49.

[160] H. Okamoto, Al-Ni (Aluminum-Nickel), J. Phase Equilibria Diffus. 25 (2004) 394–394.

[161] H. Okamoto, Supplemental Literature Review of Binary Phase Diagrams: Ag-Ni, Al-Cu, Al-Sc, C-Cr, Cr-Ir, Cu-Sc, Eu-Pb, H-V, Hf-Sn, Lu-Pb, Sb-Yb, and Sn-Y, J. Phase Equilibria Diffus. 34 (2013) 493–505.

[162] S.A. Rebegea, K. Thomas, V. Chawla, J. Michler, M.C. Kong, Laser ablation of a Cu–Al–Ni combinatorial thin film library: analysis of crater morphology and geometry, Appl. Phys. A. 122 (2016) 1074.

[163] A.J. Bradley, H. Lipson, An X-ray investigation of slowly cooled copper-nickel-aluminum alloys, Proc. R. Soc. London. 167 (1938) 421–438.

[164] M. Hafner, W. Burgstaller, A.I. Mardare, A.W. Hassel, Aluminium–copper–nickel thin film compositional spread: Nickel influence on fundamental alloy properties and chemical stability of copper, Thin Solid Films. 580 (2015) 36–44.

[165] B. Hua, Q.F. Lin, Q.P. Zhang, Z.Y. Fan, Efficient photon management with nanostructures for photovoltaics, Nanoscale. 5 (2013) 6627–6640.

[166] D.M. Karnakis, High power single-shot laser ablation of silicon with nanosecond 355 nm, Appl. Surf. Sci. 252 (2006) 7823–7825.

[167] Y.P. Deng, Y.F. Guan, J.D. Fowlkes, S.Q. Wen, F.X. Liu, G.M. Pharr, P.K. Liaw, C.T. Liu, P.D. Rack, A combinatorial thin film sputtering approach for synthesizing and characterizing ternary ZrCuAl metallic glasses, Intermetallics. 15 (2007) 1208–1216.

[168] Y. Liu, M.Q. Jiang, G.W. Yang, Y.J. Guan, L.H. Dai, Surface rippling on bulk metallic glass under nanosecond pulse laser ablation, Appl. Phys. Lett. 99 (2011) 191902.

[169] V. Raghavan, Al-Cu-Zr (Aluminum-Copper-Zirconium), J. Phase Equilibria Diffus. 32 (2011) 452–454.

[170] J. Puustinen, J. Lappalainen, J. Hiltunen, M. Hiltunen, Surface nanostructure effects on optical properties of Pb(Zr x Ti1-x)O3 thin films, Appl. Phys. A Mater. Sci. Process. 116 (2014) 379–387.